Energy Efficient Control of a Speed and Displacement Variable Hydraulic Pump

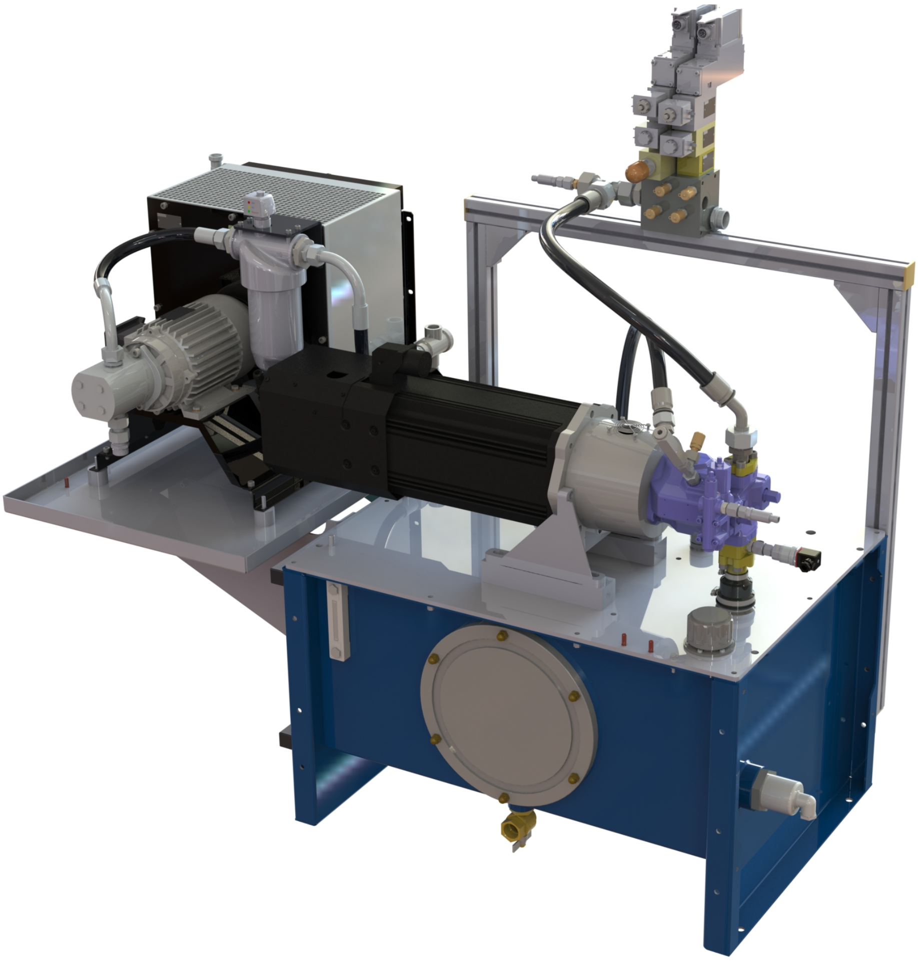

Master Project
Group 4.105C
Electro-Mechanical System Design
Aalborg University
3rd of June 2020

AALBORG UNIVERSITY
STUDENT REPORT

Board of Studies for
Mechanics and Physics
Fibigerstræde 16
DK - 9220 Aalborg Øst
Tel. 99 40 85 32
snmp@mp.aau.dk
http://www.ses.aau.dk/

Title: Energy Efficient Control of a Speed and Displacement Variable Hydraulic Pump

Semester: Fourth semester

Semester theme:
Master Thesis

Project duration: 03-02-2020 to 03-06-2020

ECTS: 30

Supervisor:
Lasse Schmidt

Project group:

Jesper Mortensen

Report pages: 73
Appendix: 25

Synopsis:

The following report presents the modelling, analysis and control of a speed and displacement variable hydraulic pump. In relation to conventional hydraulic pumps, this has a second degree of freedom. The project aims to develop control algorithms allowing the system to track a pressure reference, while increasing the efficiency. Taking offset in a previously developed model, this is initially improved to become sufficient for control development. A benchmark control method is developed with the purpose of representing the industry-best-practice, while 16 load trajectories are defined. The benchmark control method is experimentally evaluated to yield an average RMS pressure tracking error of 5.2 [bar] and an average efficiency of 49.5 [%] for the load trajectories. The system pressure and efficiency capabilities are analysed and mapped by implying steady state to the model. As a result it is suggested, that the system is generally most efficient when the swash plate swivel angle is at its maximum, yielding that the pump corresponds to a variable speed fixed displacement pump. Two control strategies are proposed of which a sliding mode disturbance observer based MIMO-approach is experimentally evaluated to yield an average RMS pressure tracking error of 1.9 [bar] and an average efficiency of 61.0 [%] for the load trajectories. This constitutes a pressure tracking improvement of 63 [%] and an efficiency improvement of 23 [%] compared to the benchmark. A few potential issues are identified, while their solution is left for further development. The developed control is deemed to show promising potential for future industrial application.

Preface

This report documents the master thesis, completed by the project group 4.105C from 4^{th} semester of the M.Sc. in Electro-Mechanical System Design at Aalborg University. The project is conducted in the period of the 3^{rd} of February to the 3^{rd} of June 2020.

The project concerns the development of control-algorithms for a speed and displacement variable hydraulic pump. This system will for reasons stated in the problem introduction be referred to as a "hydro gear". The developed control aims to track a pressure reference while increasing the system efficiency, with the perspective of decreasing the energy consumption of the hydro gear and potentially aiding the industry with reducing the energy consumption.

Reading Guide

Throughout the report, figures, tables and equations are numbered. The number refer to the chapter in which they are placed and the numeration in the chapter. External literature is referenced to by a number in square brackets, which refer to the bibliography in the end of the report. Appendices are attached in the end of the report, with capital letters indicating their chapter.

Abstract

Nærværende rapport omhandler udvikling af reguleringsalgoritmer til en variabel hastigheds- og deplacement pumpe. Indledningsvist introduceres testbænken: Den har de to indgange bestående af induktionsmotorens hastighed og en styreindgang til pumpens styreventil. Ved et tidligere projekt er pumpen modelleret, og denne model forbedres ved tilføjelse af en overtryksventil på pumpens udgangsside, ved revision af modellens antal af dynamiske ordener samt ved forbedring af modellens parametre, med anvendelse af optimering. Modellen omfatter desuden effekttabene i induktionsmotoren, pumpen og i styreenheden.

Der defineres to reguleringsobjektiver, hvorved pumpen skal følge en trykreference, mens de samlede effekttab af systemets væsentligste komponenter minimeres, med henblik på at maksimere systemets energieffektivitet. På baggrund af modellens svære ulineariteter vælges det, at løsningsstrategien for at indfri de to reguleringsobjektiver skal tage udgangspunkt i ulineær kontrol, og i særdeleshed den såkaldte sliding mode kontrol (SMC).

Med antagelse af stationær tilstand for modellen udlægges systemets tryk- og effektivitetsevne, som funktion af de to indgangssignaler og ved en given udgangseffekt. Herved blev det fundet, at systemet generelt er mest effektivt, når pumpens svingplade er vinklet helt ud. Dette skyldes, at pumpens styreenhed lukker af for størstedelen af de flow, der bidrager til styreenhedens virkemåde, men som også må regnes for effekttab.

Der udarbejdes en simpel styring af pumpen, som har til formål at skabe et sammenligningsgrundlag til den egentlige kontroludvikling. Denne styring er baseret på at efterligne en konventionel konstant frekvens, variabel deplacement pumpe. Ved at definere 16 lasttrajektorier med varierende lastgrader og trykreferencer kan systemets effektivitet og evne til at følge referencetrykket kvantificeres. Med denne styring opnås eksperimentelt en effektiv fejl (RMS) mellem reference- og udgangstryk på 5.2 [bar] samt en gennemsnitlig effektivitet på 49.5 [%] over samtlige lasttrajektorier.

Kontroludviklingen er delt i to: Først anvendes en SISO-betragtning, hvor en lineær regulator assisteres af en ulineær disturbance observer (forstyrrelsesobservator) til at styre udgangstrykket via rotorhastigheden, mens en opslagstabel anvendes til at definere det mest energieffektive valg af signal til styreventilen. Tabellen dannes på baggrund af effektivitetsresultaterne fra antagelse af stationær tilstand. Denne metode viser ved simulering gode resultater, men brugen af en opslagstabel ønskes undgået, idet denne er unik for simuleringmodellen. Som løsning herpå tager del to af kontroludviklingen udgangspunkt i en MIMO-betragtning. Herved genanvendes den udviklede ulineære trykregulering, mens der udvikles en effekttabsregulering. Denne tager ligeledes udgangspunkt i en lineær regulator, som assisteres af en ulineær disturbance observer. Løsningen viser gode resultater ved simulering, og ved eksperimentel implementering opnås en effektiv fejl (RMS) mellem reference- og udgangstryk på 1.9 [bar] samt en gennemsnitlig effektivitet på 61.0 [%] over samtlige lasttrajektorier.

Enkelte udfordringer med den udviklede kontrol, såsom små oscillationer i kontrolsignalet ved konstant reference samt eventuelle udfordringer med overophedning af induktionsmotoren efterlades til videre udvikling. Den etablerede reguleringsalgoritme vurderes at vise væsentligt potentiale for fremtidig industriel anvendelse.

Nomenclature

a	Polynomial coefficient [-]
A	Discharge area [m^2]
A	Piston area [m^2]
A	ODE solution amplitude coefficient [-]
B	Viscous friction coefficient [Nms/rad]
C	Nominal control gain [-]
C	Leakage coefficient [$m^3/(sPa)$]
d	Unknown bound disturbance [-]
D	Controller [-]
D	Max. displacement of pump per revolution [m^3]
D	Upper disturbance bound [-]
e	Control error [-]
f	Polynomial function [-]
f	Control Disturbance [-]
F	Spring pretension [N]
g	Input dynamics [-]
G	Transfer function [-]
I	Electric Current [A]
J	Moment of inertia for rotary group [kgm^2]
k	Control gain for super-twisting algorithm [-]
K	Conversion ratio [-]
K	Spring stiffness [N/m]
K	Equivalent static flow gain [$\frac{m^3}{s\sqrt{Pa}}$]
K	Ratio of model and actual input dynamics [-]
l	Normalized load valve input [-]
L	Inductance [H]
L	Upper disturbance bound [-]
M	Equivalent mass of swash plate control piston assembly [kg]
n	Polytropic index [-]
p	Number of pole pairs [-]
P	Pressure [Pa]
q	Array of design variables used in optimization [-]
Q	Volumetric flow [m^3/s]
r	Residual [-]
R	Ohmic resistance [Ω]
s	Laplace transform variable [-]
S	Input dynamics [-]
t	Time [s]
u	Normalized control valve input [-]
U	Voltage [V]
U	Nominal and compensating control signals [-]

v	Position of output pressure relief valve spool [m]
V	Volume [m^3]
V	Lyapunov function [-]
w	Auxiliary control variable of the super-twisting algorithm [-]
W	Input dynamics [-]
x	Position of swash plate control piston [m]
y	Position of electrically actuated pressure relief valve spool [m]
z	Position of control valve spool [m]
z	Auxiliary variable for SMDO [-]
α	Air to oil ratio, assumed constant in the entire system [-]
α	Control tuning constant [-]
β	Bulk modulus [Pa]
ϵ	Constraint tolerance for optimization [-]
ϵ	Sigmoid boundary layer width [-]
γ	Helping variable for 2SMDO [-]
ω	Natural frequency [rad/s]
ω	Angular velocity [rad/s]
$\mathcal{P}$	Power [J/s]
φ	Boundary layer width [-]
Φ	Optimization objective function [-]
$\mathit{\Psi}$	Flux linkage [Wb]
ρ	Control gain for first order sliding algorithms [-]
σ	Auxiliary constant for describing the electro magnetic torque [-]
σ	Sliding mode variable [-]
θ	Swash plate swivel angle [rad]
τ	Torque [Nm]
τ	Time constant [-]
ν	Sliding mode control output [-]
χ	System state vector [-]

Contents

1 System Introduction & Model Development

In this chapter, the concept of the speed and displacement variable hydraulic pump will be introduced, as a specific type of a hydraulic power unit (HPU). Then, the project test bench will be introduced, leading to the introduction of a previously developed dynamic model for the test bench. This will finally be revised for improving its dynamic resemblance to the physical test bench and allow for control development.

1.1 The Hydro Gear

A hydraulic power unit (HPU) is used in most hydraulic systems. In industry, a HPU commonly works by transforming electrical power into hydraulic power, by making use of an electric motor and a hydraulic pump. It is often designed for supplying a constant pressure at varying flow or by load sensing pressure control. In figure 1.1, a highly simplified representation of an HPU with a black box consumer is depicted.

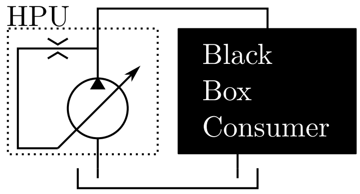

Figure 1.1: Highly simplified system consisting of an HPU supplying a black box consumer. As seen, the output pressure is used to control the pump by an unspecified method. Figure from [1].

The HPU is conventionally realized by using the constant frequency electric grid to supply a three phase induction motor, which then propels a pressure compensated variable displacement pump [2]. This setup has one degree of freedom, being the pump displacement which is used for controlling the output pressure.

By using a frequency converter to supply the induction motor, the speed and displacement variable hydraulic pump has a second degree of freedom. Due to this, the pump can be regarded as a step-less hydraulic gear which is the reason the pump will be referred to as a ”hydro gear” hence forth. This second degree of freedom can then be used to pursue secondary control objectives, such as increasing the system efficiency, which will form the basis for the project in hand.

1.2 The Project Test Bench

In figure 1.2, the project test bench is illustrated, with the electronics control cabinet and the hose section from output to tank excluded. The electronic control cabinet is situated to the right, opposing the cooling unit.

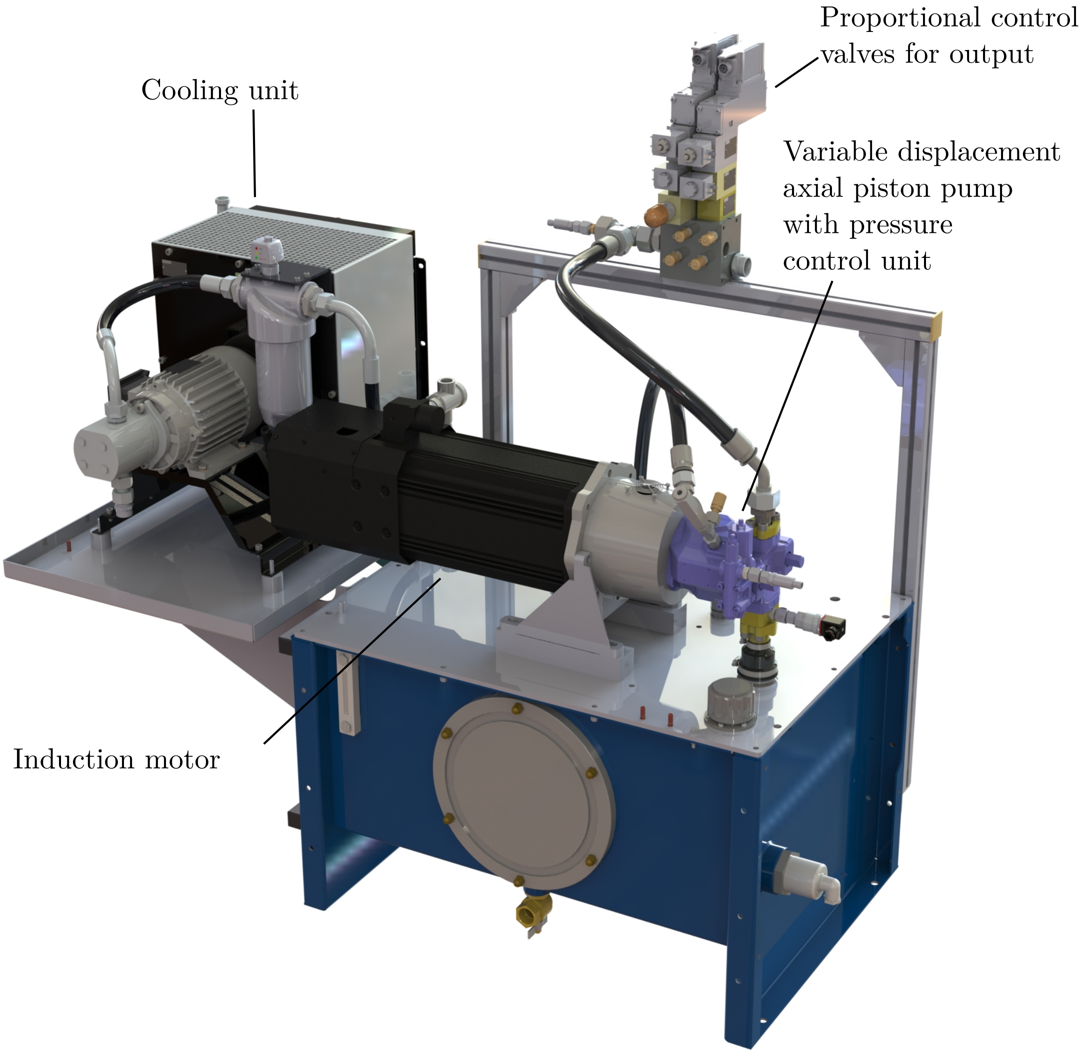

Figure 1.2: Illustration of the project test bench with certain areas named for reference. The illustration excludes the electronics control cabinet and the hose connection from the output to tank.

A reduced version of the hydraulic schematic of the project test bench is depicted in figure 1.3. Here, four digital valves in the output stages, the cooling unit and few other components have been omitted from the schematic. For the purpose of loading the hydro gear, the proportional control valves in the output stages are connected to work as flow restrictions between the pump output and the tank. There are four pressure transducers on the test bench while no flow transducers.

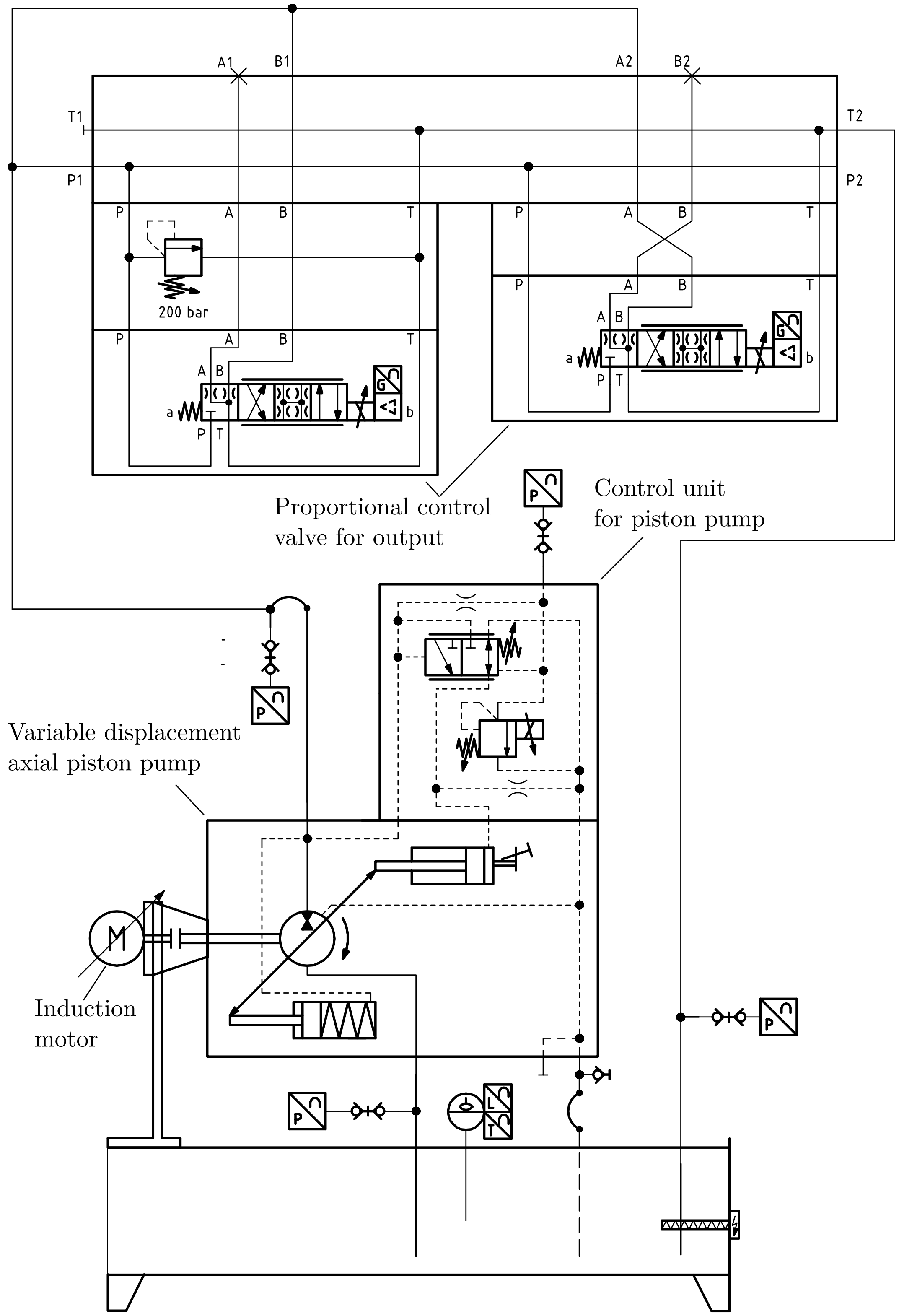

Figure 1.3: Reduced hydraulic schematic with certain areas named for reference. From [1].

In appendix A, the main components of the hydro gear and their key parameters are specified. Of these it is emphasized that the pump displacement is 18 [cm^3/rev] while the system is rated for 42 [L/min] at 170 [bar].

1.3 Previously Developed Dynamic Model

In this section, the model derived in a previous project is presented along with its results. According to [1], the hydro gear can be modelled based on the schematic of figure 1.4.

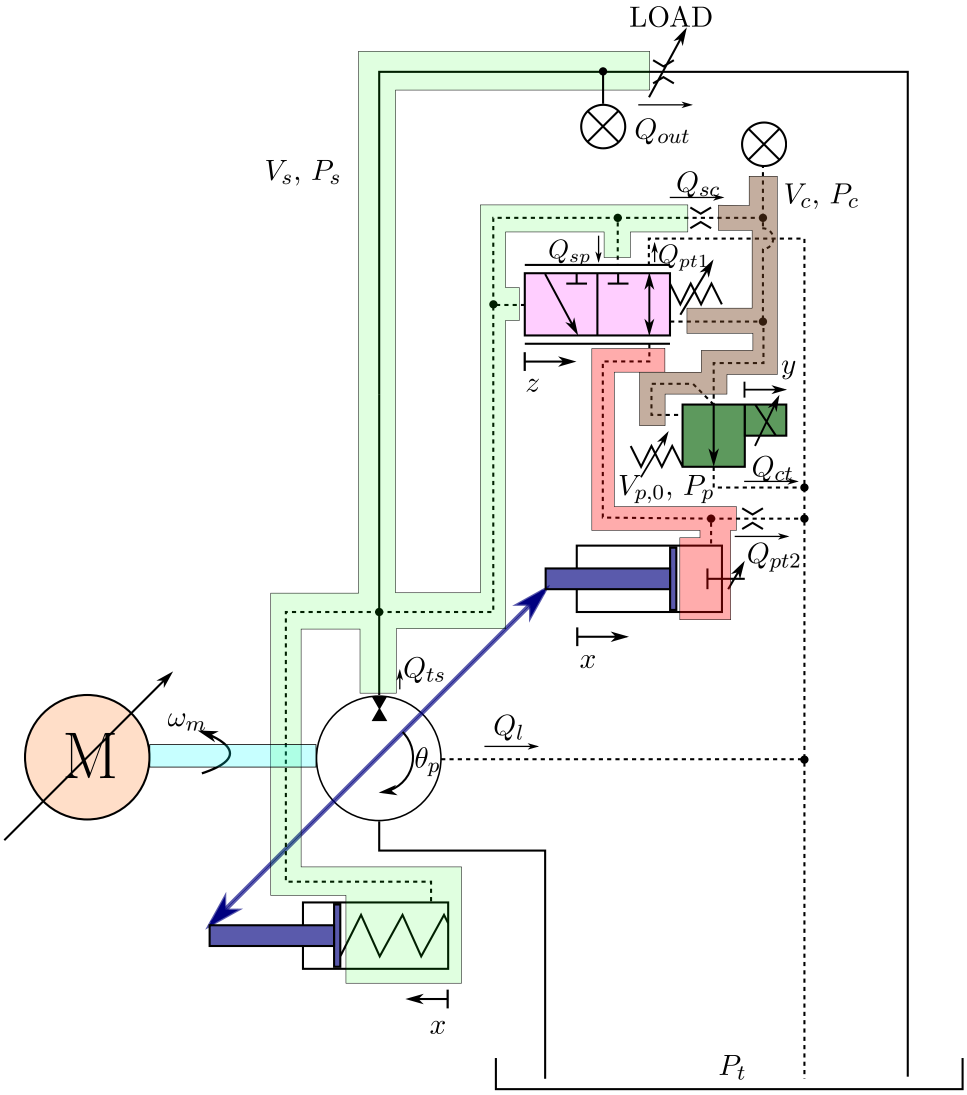

Figure 1.4: The simplified hydraulic system schematic, that forms the basis for the dynamic model developed in [1].

The coloured sections represent lumped components contributing with dynamics and/or non-linearities to the model [1].

1.3.1 Dynamic Model of Hydraulic System

As seen in figure 1.4 three hose sections are highlighted. These are each modelled with first order dynamics according to equation 1.1-1.3. Furthermore the combined swash plate and piston mass is highlighted as they are modelled according to equation 1.4. This is based on assuming them to move translationally according to the illustration of figure 1.5. The combined rotary group of the induction motor and hydraulic pump is highlighted and is modelled according to equation 1.5.

$$\dot{P}_s = \frac{\beta_s}{V_s}(Q_{ts} - Q_{sp} - Q_{sc} - Q_{out}) \quad | \; P_s \leq 200[\text{bar}] \tag{1.1}$$

$$\dot{P}_p = \frac{\beta_p}{V_{p,0} + A_{px}x}(Q_{sp} - Q_{pt} + A_{px}\dot{x}) \tag{1.2}$$

$$\dot{P}_c = \frac{\beta_c}{V_c}(Q_{sc} - Q_{ct}) \tag{1.3}$$

$$\ddot{x} = M^{-1}(F_{sx,0} + A_{sx}(P_s - P_0) + K_{sx}(x_{max} - x) - B_v\dot{x} - A_{px}(P_p - P_0)) \tag{1.4}$$

$$| \; 0 < x_{min} \leq x \leq x_{max}$$

$$\dot{\omega}_m = J^{-1}(\tau_{em} - D_s K_{\theta p} x(P_s - P_t) - B_\omega \omega_m) \tag{1.5}$$

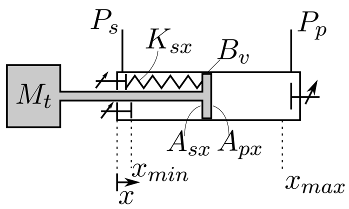

Figure 1.5: Illustration of the simplified model of the swash plate control pistons. From [1].

The flows of the system are modelled according to equation 1.6-1.11.

$$Q_{ts} = D_s\omega_m K_{p\theta} x - Q_l \quad | \; K_{p\theta} = \frac{1}{x_{max}} \tag{1.6}$$

$$Q_l = C_l(P_s - P_t)$$

$$Q_{sp} = K_{sp} z\sqrt{|P_s - P_p|} \cdot sgn(P_s - P_p) \tag{1.7}$$

$$Q_{sc} = K_{sc}\sqrt{|P_s - P_c|} \cdot sgn(P_s - P_c) \tag{1.8}$$

$$Q_{out} = K_{out} l\sqrt{|P_s - P_t|} \cdot sgn(P_s - P_t) \tag{1.9}$$

$$Q_{pt} = (K_{pt1}(z_{max} - z) + K_{pt2})\sqrt{|P_p - P_t|} \cdot sgn(P_p - P_t) \tag{1.10}$$

$$Q_{ct} = K_{ct} y\sqrt{|P_c - P_t|} \cdot sgn(P_c - P_t) \tag{1.11}$$

The displacements of the electrically actuated pressure relief valve and the pressure control valve are modelled according to equation 1.12 and 1.13 on basis of figure 1.6 and 1.7, respectively.

$$y = K_{cy}^{-1}((P_c - P_0)A_{cy} - F_{cy,0} - K_u u) + y_{max} \quad | \; 0 \leq y \leq y_{max} \tag{1.12}$$

$$z = K_{cz}^{-1}((P_s - P_0)A_{sz} - F_{cz,0} - (P_c - P_0)A_{cz}) \quad | \; 0 \leq z \leq z_{max} \tag{1.13}$$

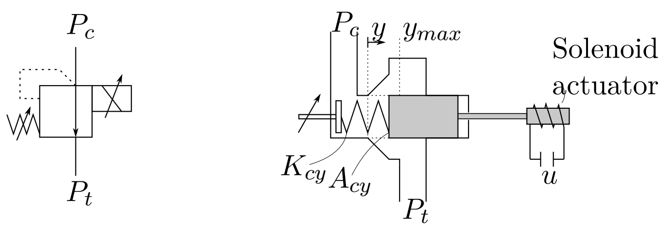

Figure 1.6: Illustration of the pressure relief valve, with its schematic representation to the left and a simplified cross section used to describe its flow paths as well as forces acting on the spool to the right. From [1].

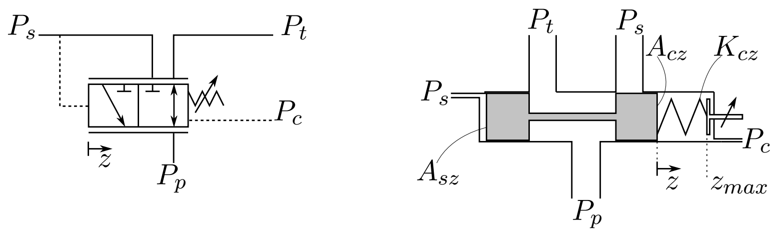

Figure 1.7: Illustration of the pressure control valve, with its schematic representation to the left and a simplified cross section used to describe its flow paths as well as forces acting on the spool to the right. From [1].

Lastly the bulk modulus of the oil within each control volume is modelled according to equation 1.14-1.16.

$$\beta_s = \frac{(1-\alpha)\cdot exp(\frac{P_0-P_s}{\beta_0}) + \alpha\cdot(\frac{P_0}{P_s})^{\frac{1}{n}}}{\frac{1-\alpha}{\beta_0}\cdot exp(\frac{P_0-P_s}{\beta_0}) + \frac{\alpha}{n\cdot P_0}\cdot(\frac{P_0}{P_s})^{\frac{n+1}{n}}} \tag{1.14}$$

$$\beta_p = \frac{(1-\alpha)\cdot exp(\frac{P_0-P_p}{\beta_0}) + \alpha\cdot(\frac{P_0}{P_p})^{\frac{1}{n}}}{\frac{1-\alpha}{\beta_0}\cdot exp(\frac{P_0-P_p}{\beta_0}) + \frac{\alpha}{n\cdot P_0}\cdot(\frac{P_0}{P_p})^{\frac{n+1}{n}}} \tag{1.15}$$

$$\beta_c = \frac{(1-\alpha)\cdot exp(\frac{P_0-P_c}{\beta_0}) + \alpha\cdot(\frac{P_0}{P_c})^{\frac{1}{n}}}{\frac{1-\alpha}{\beta_0}\cdot exp(\frac{P_0-P_c}{\beta_0}) + \frac{\alpha}{n\cdot P_0}\cdot(\frac{P_0}{P_c})^{\frac{n+1}{n}}} \tag{1.16}$$

1.3.2 Dynamic Model of Three Phase Induction Motor & Controller

The three phase induction motor is modelled in synchronous reference frame according to equation 1.17.

$$\dot{\Psi}_{sd} = -\frac{R_s(L_m\Psi_{rd} - L_r\Psi_{sd})}{\sigma_{IM}} + \Psi_{sq}\omega_s + U_{sd} \tag{1.17a}$$

$$\dot{\Psi}_{sq} = -\frac{R_s(L_m\Psi_{rq} - L_r\Psi_{sq})}{\sigma_{IM}} - \Psi_{sd}\omega_s + U_{sq} \tag{1.17b}$$

$$\dot{\Psi}_{rd} = -\frac{R_r(L_m\Psi_{sd} - L_s\Psi_{rd})}{\sigma_{IM}} + \Psi_{rq}\omega_\Delta \tag{1.17c}$$

$$\dot{\Psi}_{rq} = -\frac{R_r(L_m\Psi_{sq} - L_s\Psi_{rq})}{\sigma_{IM}} - \Psi_{rd}\omega_\Delta \tag{1.17d}$$

Here the inductances, currents and flux linkages are related by $\Psi_{sd} = L_mI_{rd} + L_sI_{sd}$, $\Psi_{sq} = L_mI_{rq} + L_sI_{sq}$, $\Psi_{rd} = L_mI_{sd} + L_rI_{rd}$ and $\Psi_{rq} = L_mI_{sq} + L_rI_{rq}$. With the common denominator $\sigma_{IM} = L_m^2 - L_sL_r$. Then the developed torque is defined by equation 1.18.

$$\tau_{em} = -\frac{3p_bL_m}{2}\left(\frac{\Psi_{rd}\Psi_{sq} - \Psi_{sd}\Psi_{rq}}{\sigma_{IM}}\right) \tag{1.18}$$

The standard control scheme of the induction motor is field oriented current control (FOC), with an outer velocity feedback loop. This is modelled according to figure 1.8 with control gains according to table 1.1.

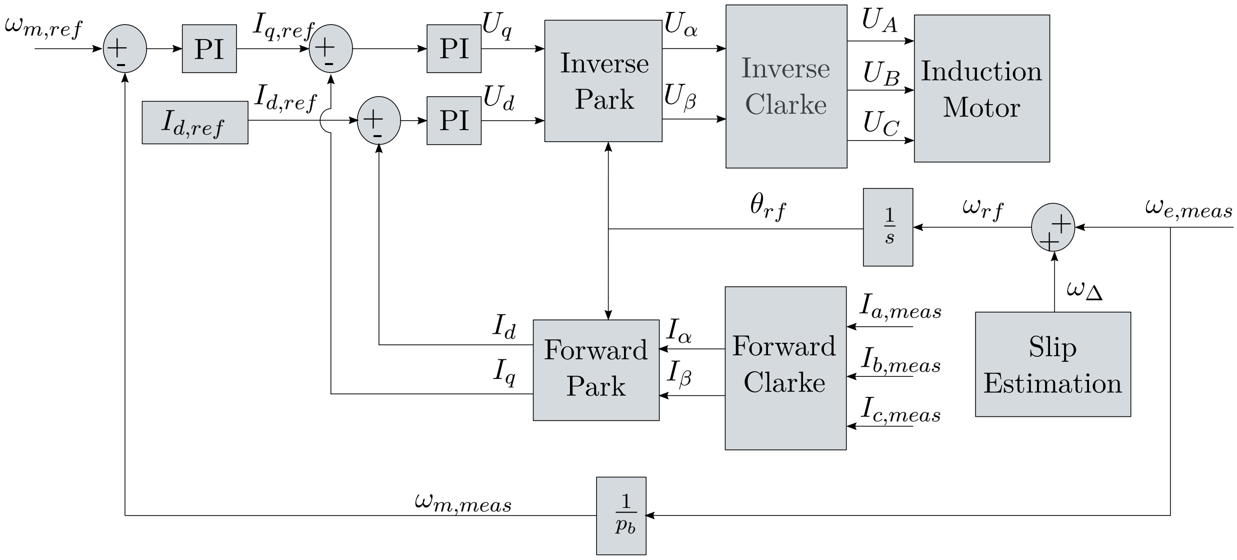

Figure 1.8: Cascade control scheme of FOC.

Table 1.1: The controller gains of the FOC PI controllers, as tuned by the Bosch Rexroth IndraWorks software.

	Unit	K_p	K_i
Speed controller	$[\frac{A}{rad/s}]$	12.54	804.10
Direct & quadrature axis current controller	$[\frac{V}{A}]$	4.07	2713.33

The slip speed is estimated through equation 1.19, based on stator currents only.

$$\omega_\Delta = \frac{R_r}{L_r}\frac{I_{sq}}{I_{sd}} \tag{1.19}$$

The direct axis current reference is defined according to equation 1.20.

$$I_{sd,ref} = \frac{U_s}{\omega_s L_m} \tag{1.20}$$

1.3.3 Loss Model

The loss model for the induction motor is based on [3] and stated in equation 1.21.

$$\mathcal{P}_{IM,loss} = \mathcal{P}_{loss,d} + \mathcal{P}_{loss,q} + \mathcal{P}_{loss,dq} \tag{1.21a}$$

$$\mathcal{P}_{loss,d} = \left(\frac{{\omega_s}^2{L_m}^2}{R_c} + R_s + \frac{{\omega_s}^2{L_m}^2R_s}{{R_c}^2}\right) {I_{sd}}^2 \tag{1.21b}$$

$$\mathcal{P}_{loss,q} = (R_r + R_s)\,{I_{sq}}^2 \tag{1.21c}$$

$$\mathcal{P}_{loss,dq} = -2\,\frac{\omega_s\,L_m\,R_s\,I_{sd}\,I_{sq}}{R_c} \tag{1.21d}$$

The output power of the induction motor is described by equation 1.22.

$$\mathcal{P}_{IM,out} = \tau_{em}\omega_m \tag{1.22}$$

The input power of the induction motor is described by equation 1.23.

$$\mathcal{P}_{IM,in} = \mathcal{P}_{IM,out} + \mathcal{P}_{IM,loss} \tag{1.23}$$

The input to the hydraulic system is equal to the induction motor output according to equation 1.24.

$$\mathcal{P}_{hyd,in} = \mathcal{P}_{IM,out} \tag{1.24}$$

The output power of the hydro gear is described by the power dissipated across the load valve according to equation 1.25.

$$\mathcal{P}_{out} = Q_{out}(P_s - P_t) \tag{1.25}$$

The hydraulic power losses are described by equation 1.26.

$$\mathcal{P}_{hyd,loss} = \mathcal{P}_{ts} + \mathcal{P}_{sp} + \mathcal{P}_{pt} + \mathcal{P}_{sc} + \mathcal{P}_{ct} + \mathcal{P}_x \tag{1.26a}$$
$$\mathcal{P}_{ts} = C_l(P_s - P_t)^2 + B_\omega \omega_m^2 \tag{1.26b}$$
$$\mathcal{P}_{sp} = Q_{sp}(P_s - P_p) \tag{1.26c}$$
$$\mathcal{P}_{pt} = Q_{pt}(P_p - P_t) \tag{1.26d}$$
$$\mathcal{P}_{sc} = Q_{sc}(P_s - P_c) \tag{1.26e}$$
$$\mathcal{P}_{ct} = Q_{ct}(P_c - P_t) \tag{1.26f}$$
$$\mathcal{P}_x = B_v \dot{x}^2 \tag{1.26g}$$

The combined system losses are then described by equation 1.27.

$$\mathcal{P}_{tot,loss} = \mathcal{P}_{IM,loss} + \mathcal{P}_{hyd,loss} \tag{1.27}$$

1.3.4 Parameter Identification Results

Based on data sheets, the IndraWorks Engineering PLC software and assumptions, 24 system parameters were obtained. As the system consist of a total of 48 parameters, a further 24 parameters needed to be identified. One parameter, the equivalent core resistance R_c, was identified by formulating a least squares optimization problem and applying it to measurement data. The objective was convex so a gradient based solver algorithm was applied. The remaining 23 parameters were all introduced by the hydraulic system and were identified by separating the identification problem into two sub-problems. First, the 17 parameters contributing to the steady state solution were identified as the objective function could be evaluated algebraically. Then this solution was used as an initial guess for the full hydraulic parameter identification whose objective function relied on least squares pressure residuals solved by simulation. For the case of both sub-problems, the objective function was not convex, which is why a stochastic solver algorithm was applied.

For the full parameter identification problem, the three inputs and two measurements depicted in figure 1.9 were applied.

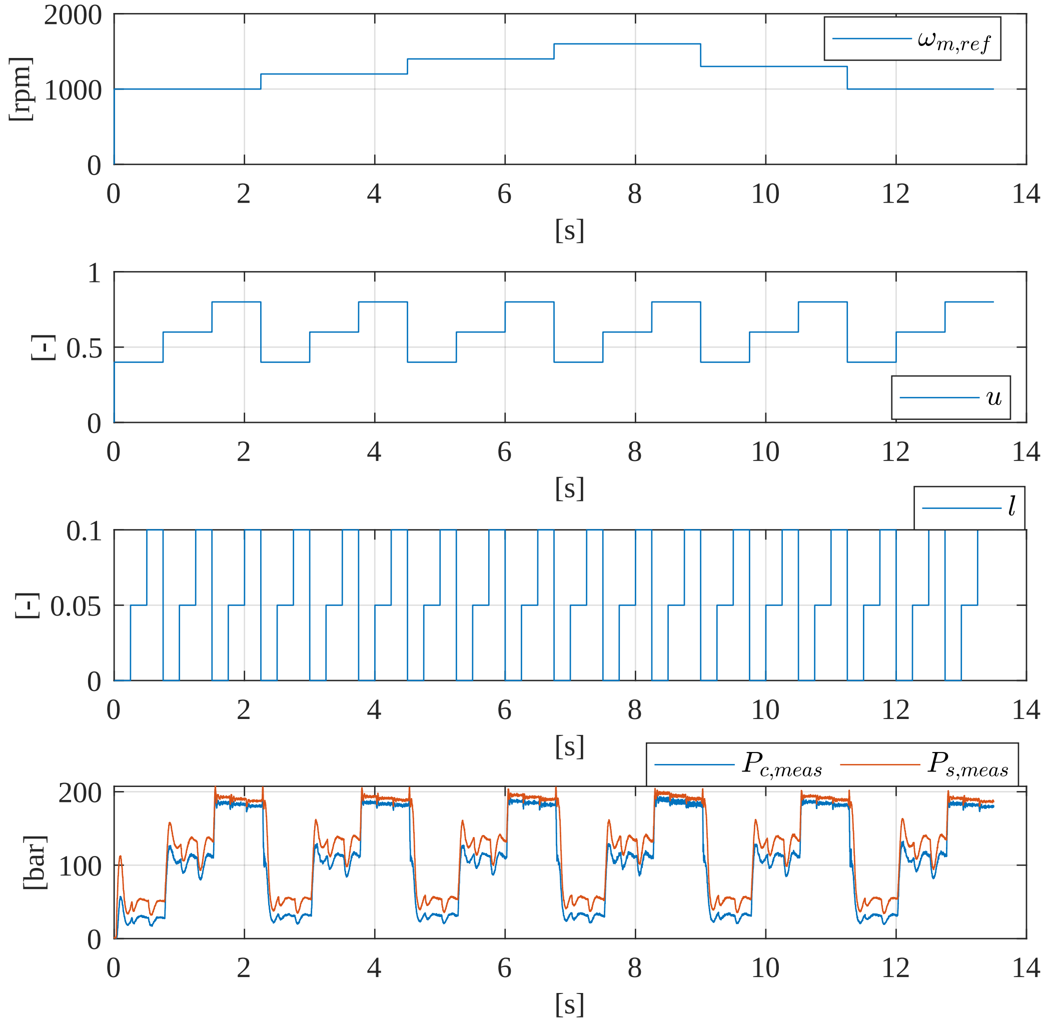

Figure 1.9: The trajectories and measurement data used for the full parameter identification. The data is sampled at 1 [kHz]. From [1].

From the parameter identification, the model pressure response of figure 1.10 was obtained.

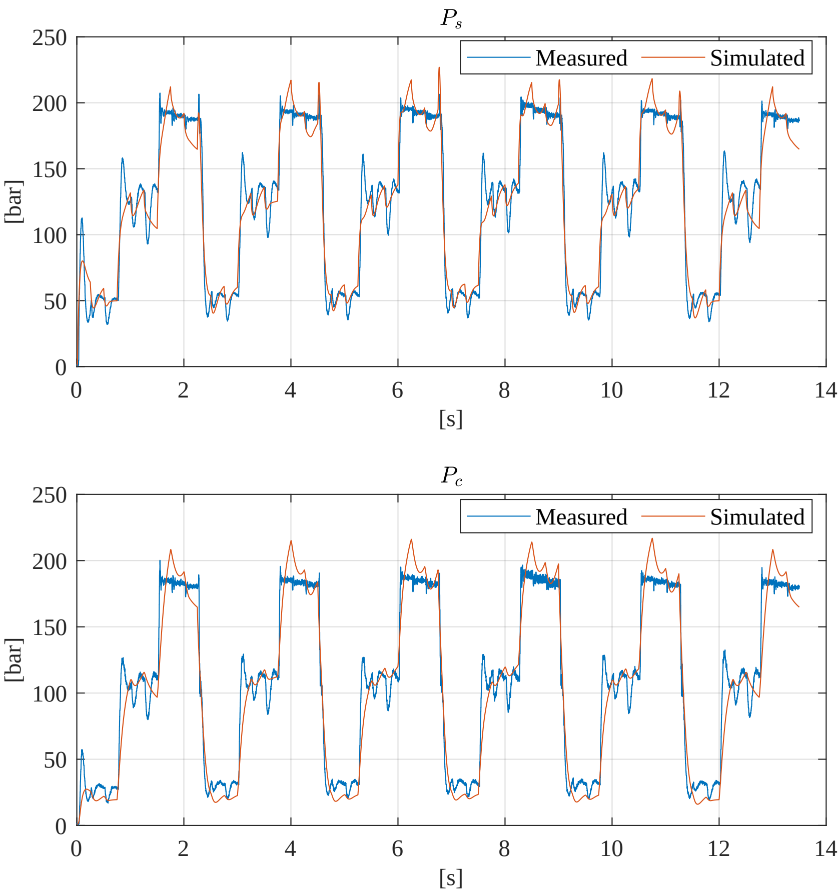

Figure 1.10: Final pressure response comparison between measured data and system model, based on the identified parameters of [1].

As seen, the simulated pressure response corresponds rather well to the measured response. The steps of u, causing the pressure to rise from approx. 50 to 125 [bar], all have an overshoot which is not represented by the model. For the high pressures of approx. 180 [bar], the measured data contain much higher frequencies than the simulated, while the simulated seems more influenced by the change of the load. These and more differences are discussed to possibly stem from a combination of unmodelled dynamics, non-linearities and the output pressure relief valve which is seen in the hydraulic schematic of figure 1.3, though was disregarded as it is set to 200 [bar]. Based on this, the model was deemed sufficient for control development, though left room for improvement. The proposed causes to the differences were used to form the proposals for future improvements, which will be the basis of the following revision of the dynamic model.

1.4 Revision of Dynamic Model

The previously found results were quite good, bearing in mind the very limited system information that was available beforehand, but as concluded, the results had room for improvement. This section seeks to improve those previously found results. Taking offset in the proposals for future improvements in [1] a output pressure relief valve is added to the model, which improves the model fit. With aim for parameter identification through optimization, the input signals are studied. Furthermore, the parameter identification objective function is revised to apply a non-linear constraint equation that implies that the proposed parameters must be able to comply with steady state, before applying the proposed parameters to the fitness function. Finally many of the previously neglected dynamic orders are revised identifying the model with the best fit and lowest dynamic order among the considered models.

1.4.1 Addition of Component: Output Pressure Relief Valve

Based on the proposals for future improvements, an output pressure relief valve is added to the model according to figure 1.11.

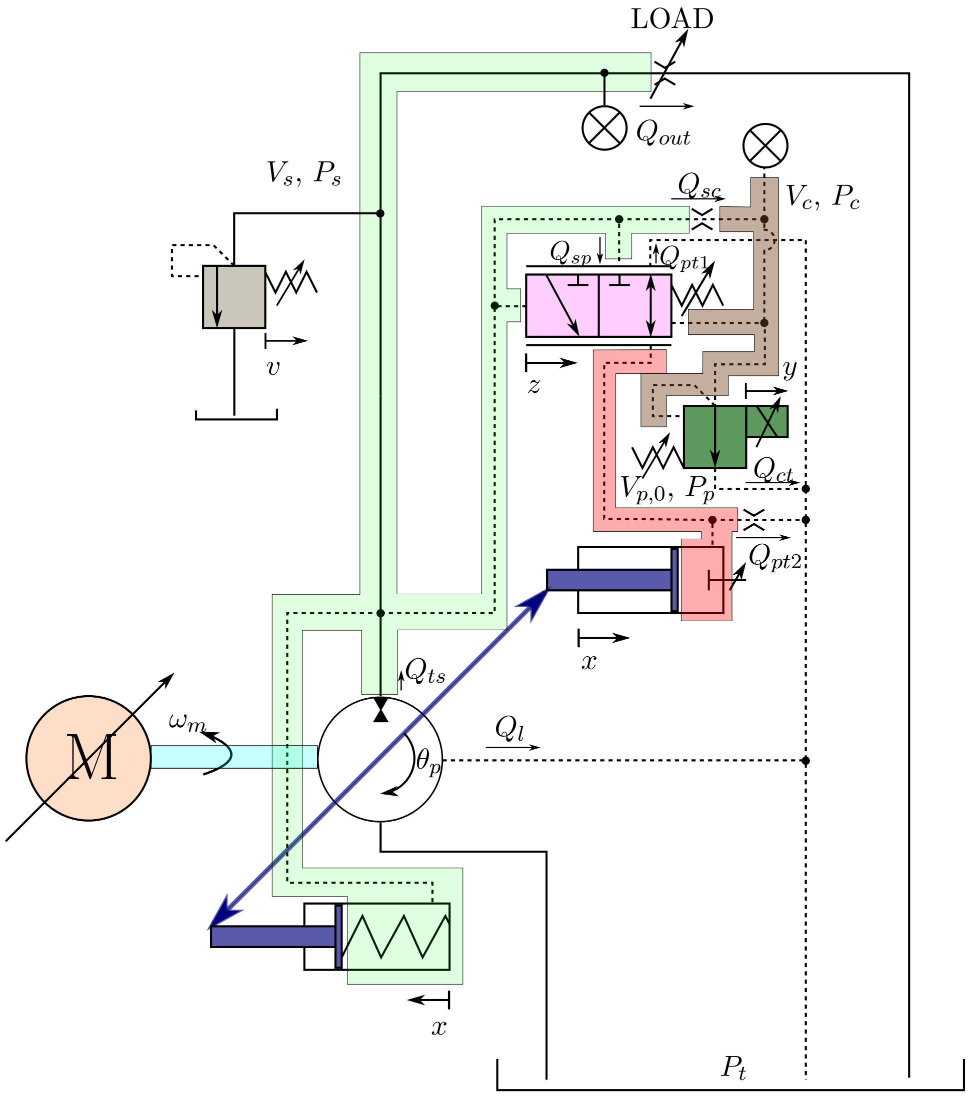

Figure 1.11: The simplified hydraulic system schematic as developed in [1], with an output pressure relief valve added.

The nomenclature and describing equations take offset in figure 1.12.

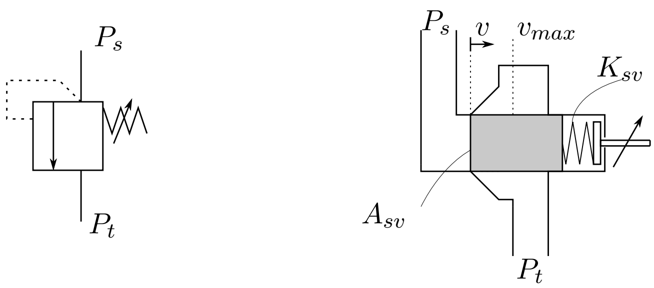

Figure 1.12: Illustration of the output pressure relief valve, which is added to the system model. To the left, the schematic representation is depicted while to the right a simplified cross section, used to describe the flow paths and the forces acting on the spool, is depicted.

As for the other valves of the model, the spool displacement is initially modelled as directly proportional to the forces acting on it and hence neglecting any dynamics. The flow through the valve is assumed turbulent and is modelled as a simplified version of the generalized orifice equation by assuming constant oil density. This is seen in equation 1.28 and 1.29 respectively.

$$v = K_{sv}^{-1}(A_{sv}(P_s - P_0) - F_{sv,0}) \quad | \, 0 \leq v \leq v_{max} \tag{1.28}$$

$$Q_{st} = vK_{st}\sqrt{|P_s - P_t|} \cdot sgn(P_s - P_t) \tag{1.29}$$

With no further notion on the procedure, the parameter identification optimization algorithm of [1] is applied on the new model containing the output pressure relief valve, yielding an immediate improvement of the model fit by 34 [%] going from $3.3869 \cdot 10^{16}$ to $2.251 \cdot 10^{16}$ [Pa^2]. From this result the output pressure relief valve begin to open at a pressure of 188.6 [bar]. The result will be used and improved in section 1.4.4.

1.4.2 Review of Input Signals for Parameter Identification

The trajectories used for the full parameter identification, figure 1.9, are produced as a sequence of steps of the inputs and the load valve. These were chosen as they were deemed to contain *relevant* dynamic and steady state information of the hydro gear. In other words: If the model is able to represent the response displayed by the chosen step trajectories, then the model represent the dominant dynamics of the system and is well suited for control development.

To challenge this concept, literature of system identification suggest to use input signals that have constant amplitude across all frequencies as these will excite all system dynamics [4]. In figure 1.13 the single-sided amplitude spectra of the inputs and the load are depicted.

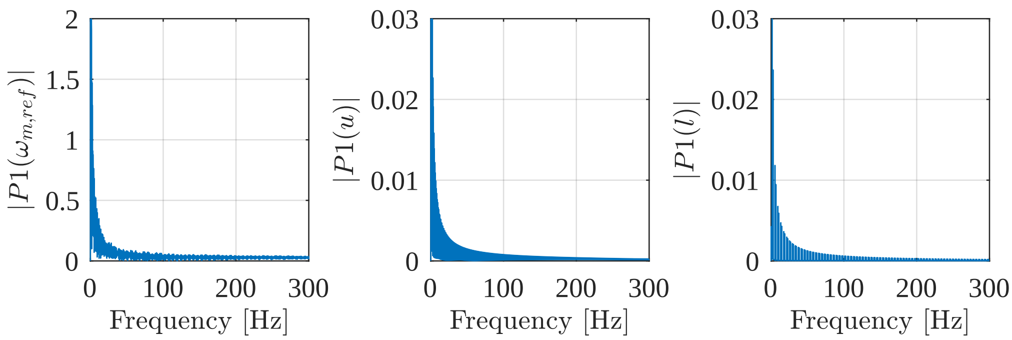

Figure 1.13: Single-sided amplitude spectra of the input signals applied in parameter identification.

As seen, the sequences of steps do not display constant amplitude across all frequencies. Instead they contain high amplitude at low frequencies and diminishing amplitude as the frequencies increase beyond 100 [Hz].

An input, that contains constant amplitude across all frequencies is the white noise signal [4], though as it requires infinite power this is not a realizable signal. The best realizable approximation is the random binary signal (RBS). Hence, a RBS is created for the control input u and the load valve l, while the induction motor follows the previously defined step-sequence. This is in order to protect the pump from excessive accelerations and the motor from overload.

The best attained update frequency of the RBS-trajectories is 500 [Hz] while logging the data at 1 [kHz]. This is though with the compromise of pausing the RBS-update while the data-logging buffer is loaded from the flash memory of the PLC onto a memory-card.

The resulting input signals and measured pressures are depicted in figure 1.14.

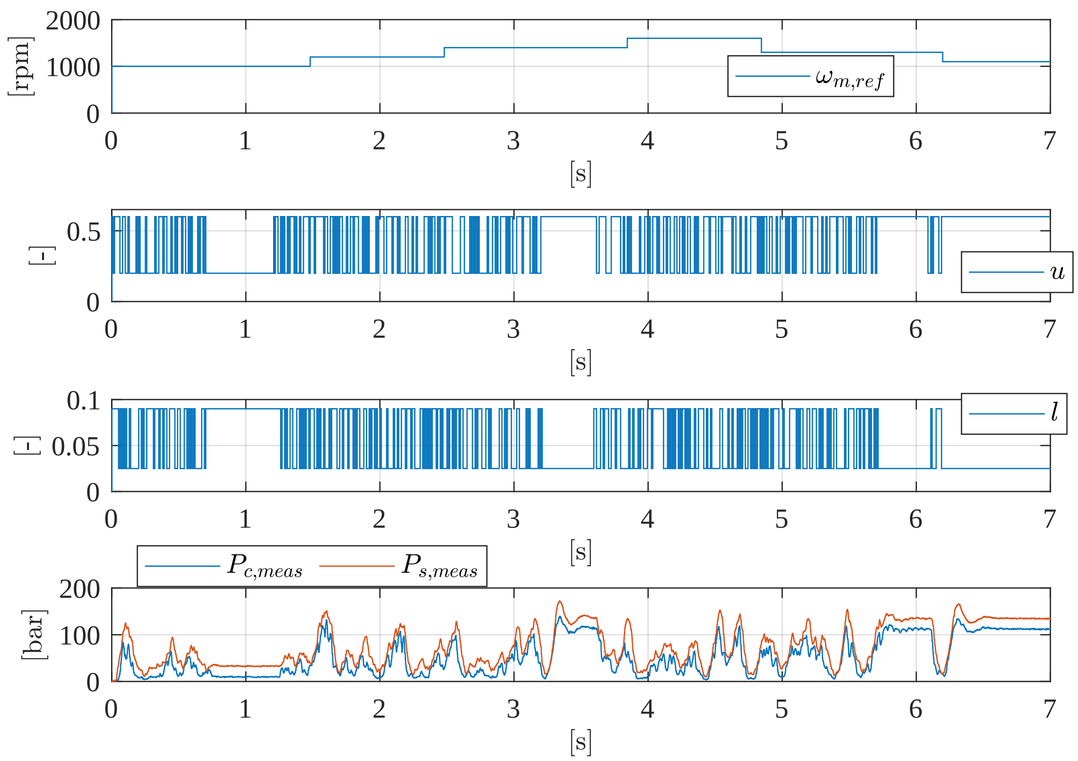

Figure 1.14: The measured pressure responses produced by the RBS signals for the control input u and the load l and the step sequence for the shaft speed, ω_m.

In figure 1.15, the single-sided amplitude spectra of the control input u and the load l are depicted.

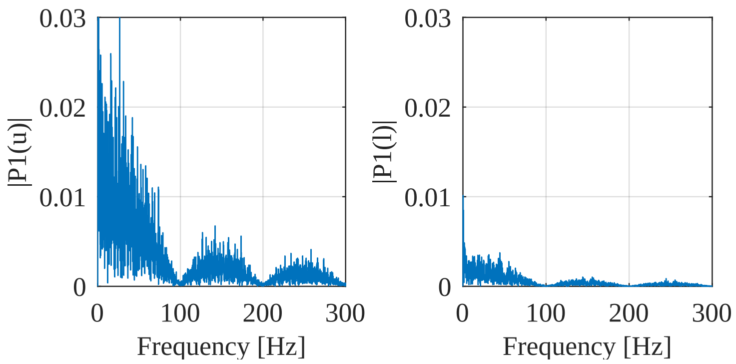

Figure 1.15: Single-sided amplitude spectra of the random binary input signals.

As seen, the frequency content is richer than for the step sequences. This will lead to excitement of more dynamics in the system. Aliasing is present in the discrete signal, as could be expected. By applying the RBS signals to the model and comparing the pressure response to the measurement it is evident, that the model does not represent the excited dynamics very well. This is seen in figure 1.16a. The amplitude of the pressure oscillations are larger in the measured data than in the simulations. As an experiment of thought, the parameters of the dynamic model are identified reusing the optimization algorithm but applying the new RBS-inputs. The resulting pressure response is depicted in figure 1.16b.

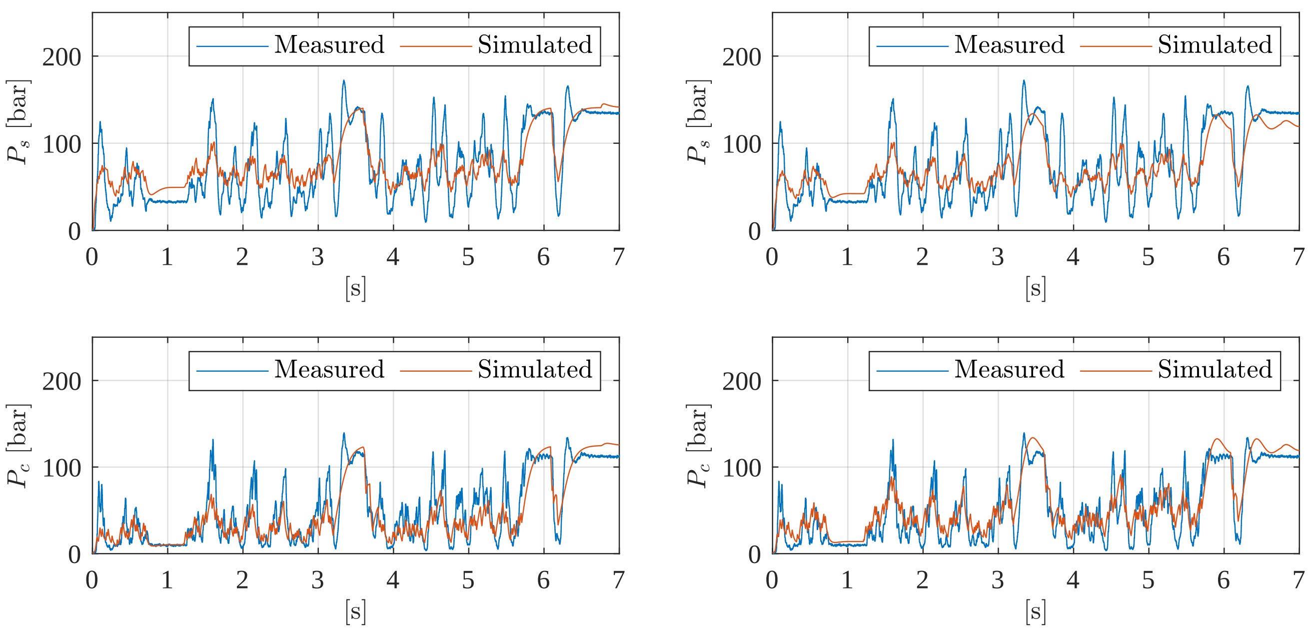

(a) The model parameters identified based on the step sequence inputs. For reference, the fitness value is $7.52 \cdot 10^{16}[\mathrm{Pa}^2]$ for the 7[s].

(b) The model parameters identified based on the RBS inputs. For reference, the fitness value is $6.73 \cdot 10^{16}[\mathrm{Pa}^2]$ for the 7[s].

Figure 1.16: Pressure response of the model compared to the measured.

As seen, the response is only slightly improved. Then applying the original step sequence on the model reveals an almost complete loss of steady state response and to a high extent a loss of dynamic response in the model. This is depicted in figure 1.17.

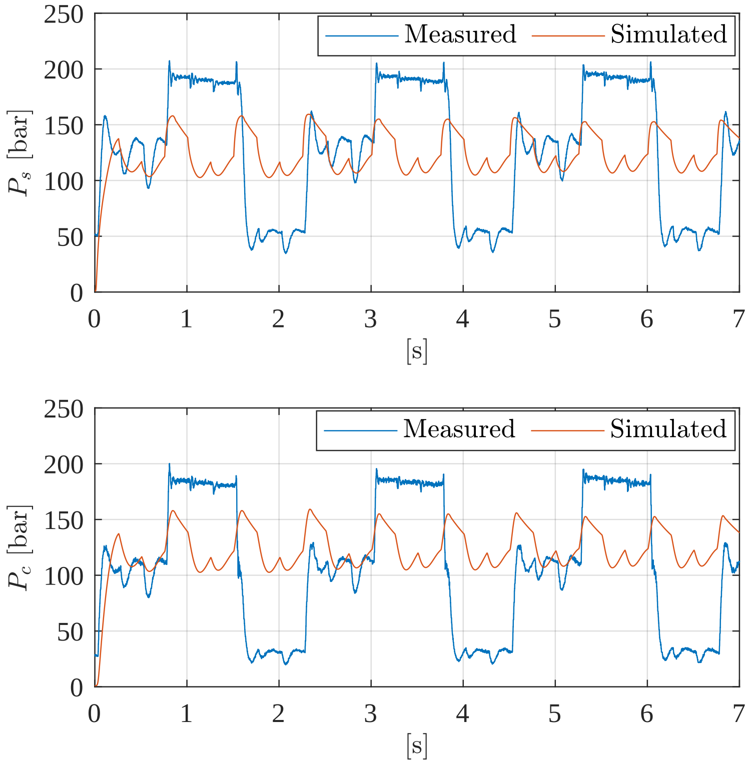

Figure 1.17: Pressure response, running the original step sequence inputs with the model parameters identified based on the RBS inputs.

When predominantly exciting low frequencies as is the case for the step sequence inputs, the model fits quite well. When also exciting higher frequencies through the RBS, the model does not fit very well. When fitting the model to the RBS-excited response, without adding more dynamic orders, the model will only improve its fit by a small degree, but with loss of most of the information that allowed it to fit the predominantly low frequency input.

This leads to two conclusions:

- The notion of the step-sequence excited response containing *relevant* system information is sound. If the model is able to represent the step-sequence excited response, it does represent the relevant system information, being the dominant low frequency response. As is generally the case, any developed controller should then be designed to avoid exciting the higher-order unmodelled frequencies.
- To this end, it is appropriate to check if adding more dynamics will improve the model fit. This is done in section 1.4.4, where the most obvious neglected dynamics are included to see if they might improve the model fit.

1.4.3 Revision of the Hydraulic Parameter Identification Objective

In the following section, another proposal for future improvement in [1] is pursued, being a revision of the parameter identification optimization objective. The method applied for attaining the previous results was to start off by identifying the parameters that contribute to the steady state solution and then use that solution along with a qualified initial guess on the remaining parameters for the full parameter identification. When proceeding to the full parameter identification problem, the identified parameters are not regarded certain as there exist infinite parameter combinations leading to the same steady state solution. This feature arises from the hydraulic closed loop system embedded in the control unit. When taking the dynamic response into account at least some of the solution space is constrained [1]. Here, the two parameter identification problems will be combined into a single more efficient problem.

The goal is to develop a parameter identification based on least squares residuals on the measured pressure responses that ensures the proposed parameters of each iteration to comply with steady state before simulating. This is realized through formulating a non-linear constraint equation, that utilizes the proposed parameters to evaluate whether they are able to comply with a measured steady state solution. If they do comply, the proposed parameters are used to evaluate the pressure residuals through simulation. If they do not, the proposed parameters are rejected. This concept has two main strengths:

- The time for solving the non-linear constraint is significantly shorter than the time for one simulation of the model. This is even though the simulation is a pre-compiled executable. In Simulink, this is known as "Rapid Accelerator Mode".
- The risk of the parameter identification routine proposing parameters causing a singularity or ill conditioning of the simulation model is drastically reduced by checking if the parameters are able to produce a steady state solution before simulating.

In equation 1.30 the objective is defined as a sum of least squared pressure residuals. The simulated pressures are dependent on the design variables q, which are separated into the design variables contributing to steady state, q_{ss}, and the variables that exclusively contribute to the transient response, q_{tr}. The objective is subject to a linear constraint being upper and lower bounds on the design variable space and the non-linear constraint, c, which is dependent on the design variables contributing to steady state. The non-linear constraint is subtracted a tolerance in order to allow for numerical errors.

$$\min \Phi(q) = \sum (r_{Ps}(q))^2 + \sum (r_{Pc}(q))^2 \ , \tag{1.30a}$$

$$\text{subject to } q_{min} \leq q \leq q_{max} \ \text{ and } c(q_{ss}) - \epsilon_{tol} \leq 0$$

$$r_{Ps}(q) = P_{s,meas} - P_s(q) \tag{1.30b}$$

$$r_{Pc}(q) = P_{c,meas} - P_c(q) \tag{1.30c}$$

$$q = [q_{ss} \quad q_{tr}]^T \tag{1.30d}$$

$$\begin{aligned} q_{ss} = [&K_u \quad C_l \quad y_{max} \quad z_{max} \quad K_{sp} \quad K_{sc} \quad K_{pt1} \quad K_{pt2} \quad \dots \\ &K_{ct} \quad A_{cy} \quad A_{cz} \quad A_{sz} \quad F_{cy,0} \quad F_{cz,0} \quad K_{cy} \quad K_{cz} \quad B_\omega]^T \end{aligned}$$

$$q_{tr} = [V_{p,0} \quad V_c \quad \alpha \quad x_{min} \quad M \quad B_v]^T \tag{1.30e}$$

The non-linear constraint is designed to evaluate if the proposed q_{ss} is meaningful with respect to steady state. The method takes offset in the section 'Reduced Parameter Identification Problem by Implying Steady State" in [1].

A non-saturated steady state data point is sampled, being: $u = 0.6$, $\omega_{m,ref} = 1400$[rpm], $l = 0.06$, $\tau_{em} = 21.6$[Nm], $P_s = 134.5$[bar] and $P_c = 112.1$[bar]. This point is deemed to have no saturated states as it is possible to control P_s in both directions through u while P_s is nearly invariant to changes of $\omega_{m,ref}$ and l in the vicinity of the point.

When assuming steady state the pressure derivatives are zero which allows to use their state equations as residuals themselves. Then applying the data point to the state equations and assuming $\omega_m = \omega_{m,ref}$ leaves the states x, y, z and P_p as unknowns.

The swash plate control piston displacement, x, is evaluated from assuming steady state for the rotary group dynamic equation and isolating for it according to equation 1.31. The valve displacements y and z are simply evaluated as their dynamics are already neglected. They are restated in equation 1.32 and 1.33.

$$x = \frac{\tau_{em} - B_\omega \omega_m}{D_s K_{\theta p}(P_s - P_t)} \tag{1.31}$$

$$y = K_{cy}^{-1}((P_c - P_0)A_{cy} - F_{cy,0} - K_u u) + y_{max} \tag{1.32}$$

$$z = K_{cz}^{-1}((P_s - P_0)A_{sz} - F_{cz,0} - (P_c - P_0)A_{cz}) \tag{1.33}$$

The pressure P_p is evaluated by assuming steady state for the swash plate control piston dynamic equation and isolating for P_p, according to equation 1.34.

$$P_p = \frac{F_{sx,0} + A_{sx}(P_s - P_0) + K_{sx}(x_{max} - x)}{A_{px}} + P_0 \tag{1.34}$$

Hence the residuals for the three pressure dynamics which are implied steady state can be evaluated directly. Then a positive definite constraint equation can be formulated by summing the squared residuals according to equation 1.35. As the sampled data point pressure level is well below 188.6 [bar], it is not necessary to take the added output pressure relief valve into account when evaluating the constraint.

$$c(q_{ss}) = r_{\dot{P}_s}^2 + r_{\dot{P}_p}^2 + r_{\dot{P}_c}^2 \tag{1.35a}$$

$$\text{equation 1.1} \rightarrow r_{\dot{P}_s} = Q_{ts} - Q_{sp} - Q_{sc} - Q_{out} \tag{1.35b}$$

$$\text{equation 1.2} \rightarrow r_{\dot{P}_p} = Q_{sp} - Q_{pt} \tag{1.35c}$$

$$\text{equation 1.3} \rightarrow r_{\dot{P}_c} = Q_{sc} - Q_{ct} \tag{1.35d}$$

Based on this a new hydraulic parameter identification optimization problem is formulated as a combination of the two methods applied in [1]. This method will prove highly efficient in the following section, by solving 16 separate identification problems in comparable time to the single result of [1].

1.4.4 Revision of the Hydraulic Model Order

In this section the dynamic model order will be revised with focus on the most obviously neglected dynamics in the results of [1]. The electrically actuated pressure relief valve displacement y and the pressure control valve displacement z had their dynamics neglected.

Likewise is the case for the added output pressure relief valve. Hence it could be interesting to evaluate whether adding dynamics to the state equations of y, z and v will improve the model fit.

From the identified parameters it is evident, that the viscous friction of the swash plate control piston is relatively large compared to its mass. Therefore, it would be interesting to evaluate whether neglecting one order, the inertial, from the swash plate control piston dynamics will yield a negligible loss of model fit while simplifying the model.

These included or neglected dynamics are defined in table 1.2.

Table 1.2: The equations describing the states x, y, z and v in terms of having either included (1) og neglected (0) dynamics.

	Neglected Dynamics 0	Included Dynamics 1
x	$\dot{x} = \frac{F_{sx,0}+A_{sx}(P_s-P_0)+K_{sx}(x_{max}-x)-A_{px}(P_p-P_0)}{B_v}$	$\ddot{x} = \frac{F_{sx,0}+A_{sx}(P_s-P_0)+K_{sx}(x_{max}-x)-B_v\dot{x}-A_{px}(P_p-P_0)}{M}$
y	$y = \frac{(P_c-P_0)A_{cy}-F_{cy,0}-K_u u}{K_{cy}} + y_{max}$	$\ddot{y} = \frac{(P_c-P_0)A_{cy}+K_{cy}(y_{max}-y)-F_{cy,0}-K_u u-B_{cy}\dot{y}}{M_{cy}}$
z	$z = \frac{(P_s-P_0)A_{sz}-F_{cz,0}-(P_c-P_0)A_{cz}}{K_{cz}}$	$\ddot{z} = \frac{(P_s-P_0)A_{sz}-K_{cz}z-F_{cz,0}-(P_c-P_0)A_{cz}-B_{cz}\dot{z}}{M_{cz}}$
v	$v = \frac{A_{sv}(P_s-P_0)-F_{sv,0}}{K_{sv}}$	$\ddot{v} = \frac{A_{sv}(P_s-P_0)-K_{sv}v-B_{sv}\dot{v}-F_{sv,0}}{M_{sv}}$

Exploiting the 0 and 1 as a binary representation of the inclusion of dynamics, 16 different models can be defined with a corresponding model number. These are stated in table 1.3. For each model the amount of hydraulic dynamic orders, the total number of parameters and the number of unknown parameters for identification are stated.

Table 1.3: Binary representation of the 16 dynamic models, which arise from all combinations of neglecting and including the defined dynamics. For each model, the number of dynamic orders in the hydraulic system, the total number of parameters and the number of unknown parameters for identification are stated.

x	0	0	0	0	0	0	0	0	1	1	1	1	1	1	1	1
y	0	0	0	0	1	1	1	1	0	0	0	0	1	1	1	1
z	0	0	1	1	0	0	1	1	0	0	1	1	0	0	1	1
v	0	1	0	1	0	1	0	1	0	1	0	1	0	1	0	1
Model #	0	1	2	3	4	5	6	7	8	9	10	11	12	13	14	15
Hyd. Dyn. Orders	5	7	7	9	7	9	9	11	6	8	8	10	8	10	10	12
Total Params.	47	49	49	51	49	51	51	53	48	50	50	52	50	52	52	54
Unknown Params.	22	24	24	26	24	26	26	28	23	25	25	27	25	27	27	29

As seen, there is a difference of seven dynamic orders between model #0 and #15.

By applying the revised hydraulic parameter identification problem to the 16 different models, updating the amount of design variables for the identification objective accordingly and applying the step-sequence based input trajectories, each model is fitted to the pressure measurements individually, from the same starting point. The best obtained fit for each model is depicted according to its amount of dynamic orders in figure 1.18.

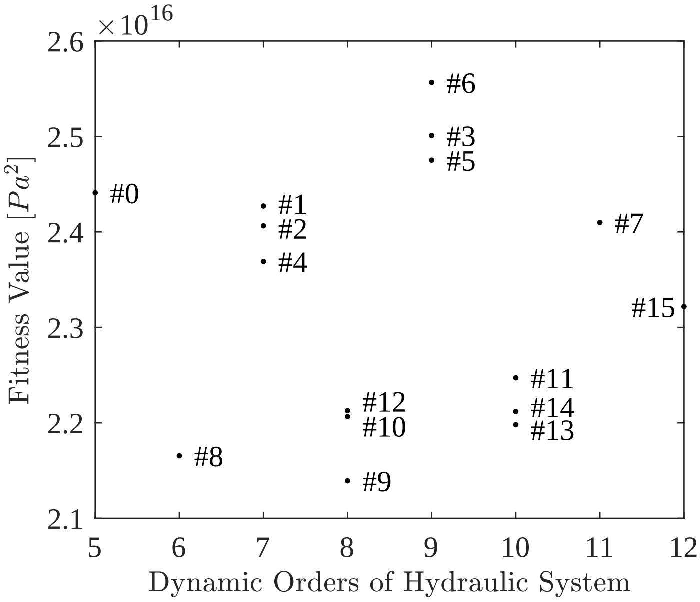

Figure 1.18: Model fit for each of the 16 models according to their number of dynamic orders in the hydraulic system.

As seen, the models that have the swash plate dynamics reduced by one order generally fit less good than the ones including the inertial term for the swash plate.

It is desirable to both reduce the fitness value and the number of dynamic orders, which is why model #0, #8 and #9 are the three best models. Model #8 offers a 13 [%] improvement of the fitness value compared to #0 by increasing the model order by one, while #9 only improves the fitness by 0.9 [%] compared to #8 by further increasing the model order by two. Therefore, model #8 is chosen for further development.

In figure 1.19 model #0, #8 and #9 are simulated in a trajectory where the time between updates is increased from 250 to 500 [ms] as to ease the comparison of the three.

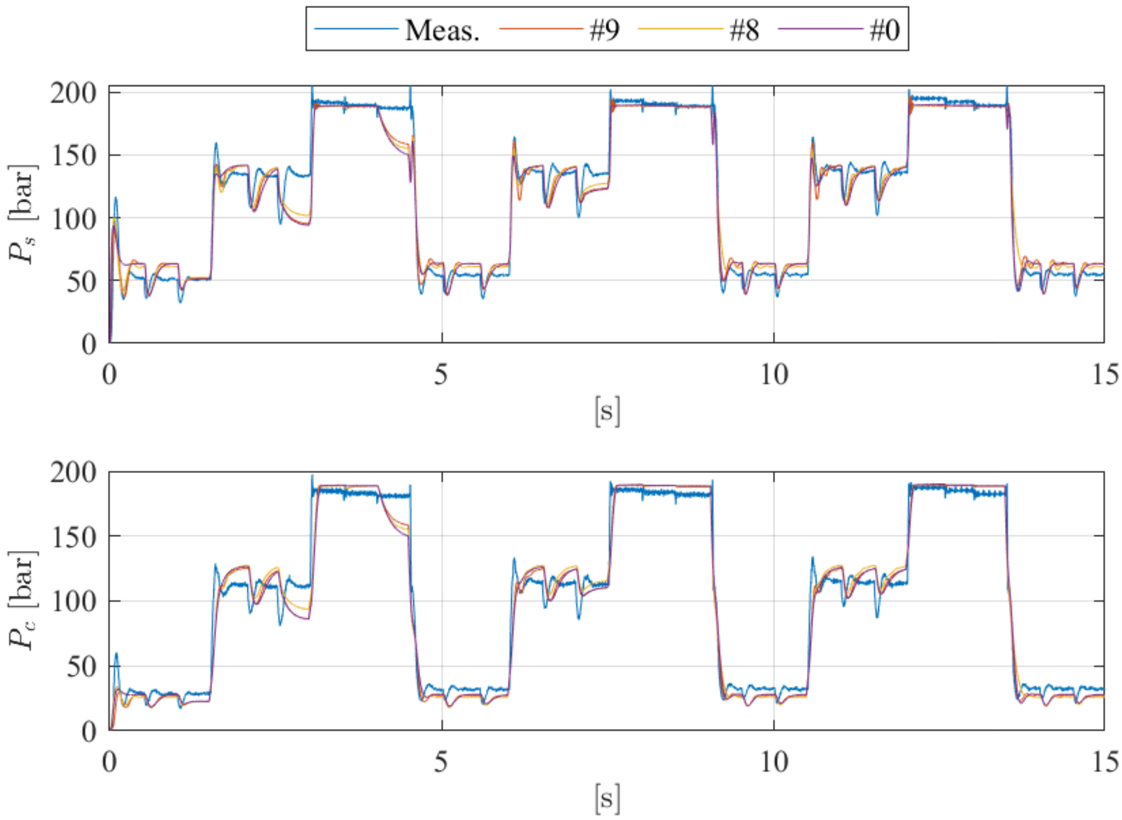

Figure 1.19: Simulated pressure response of model #0, #8 and #9.

Based on this, the dynamic system has been revised yielding an improved model while the final model has the same dynamic order as the previously found model. The two main findings of this section is, that introducing the previously neglected valve dynamics does not really improve the model fit and that the dynamics of the swash plate control pistons are best described by including the inertial terms. Indeed the nature of the model, being a lumped parameter model, does neglect many dynamic orders, some more obvious than others. It may be that the main discrepancy between the model and test bench is caused by non-linearities. An example of such non-linearity could be valve flows. It is quite likely that describing the flows of the pump as proportional to a static flow gain is inaccurate. Rather, it is likely that the flow gain should be a function of the displacement to encompass possible advanced geometric features inside the valves.

1.4.5 Final Dynamic Model

Based on the above analyses the final dynamic model is #8 with minor corrections of the non-linearities as compared to [1]. The dynamics of the hydraulic system are described by equation 1.36-1.40.

$$\dot{P}_s = \frac{\beta_s}{V_s}(Q_{ts} - Q_{st} - Q_{sp} - Q_{sc} - Q_{out}) \tag{1.36}$$

$$\dot{P}_p = \frac{\beta_p}{V_{p,0} + A_{px}(x_{max} - x)}(Q_{sp} - Q_{pt} + A_{px}\dot{x}) \tag{1.37}$$

$$\dot{P}_c = \frac{\beta_c}{V_c}(Q_{sc} - Q_{ct}) \tag{1.38}$$

$$\ddot{x} = M^{-1}(F_{sx,0} + K_{sx}(x_{max} - x) - B_v\dot{x} + A_{sx}P_s - A_{px}P_p) \quad | \quad 0 < x_{min} \leq x \leq x_{max} \tag{1.39}$$

$$\dot{\omega}_m = J^{-1}(\tau_{em} - D_s K_{\theta p} x(P_s - P_t) - B_\omega \omega_m) \tag{1.40}$$

The flows of the system are described by equation 1.41-1.47.

$$Q_{ts} = D_s\omega_m K_{p\theta}x - Q_l \quad | \; K_{p\theta} = \frac{1}{x_{max}} \tag{1.41}$$

$$Q_l = C_l(P_s - P_t)$$

$$Q_{st} = vK_{st}\sqrt{|P_s - P_t|} \cdot sgn(P_s - P_t) \tag{1.42}$$

$$Q_{sp} = K_{sp}z\sqrt{|P_s - P_p|} \cdot sgn(P_s - P_p) \tag{1.43}$$

$$Q_{sc} = K_{sc}\sqrt{|P_s - P_c|} \cdot sgn(P_s - P_c) \tag{1.44}$$

$$Q_{out} = K_{out}l\sqrt{|P_s - P_t|} \cdot sgn(P_s - P_t) \tag{1.45}$$

$$Q_{pt} = (K_{pt1}(z_{max} - z) + K_{pt2})\sqrt{|P_p - P_t|} \cdot sgn(P_p - P_t) \tag{1.46}$$

$$Q_{ct} = K_{ct}y\sqrt{|P_c - P_t|} \cdot sgn(P_c - P_t) \tag{1.47}$$

The displacements of the internal and the external valves are described by equation 1.48-1.50.

$$y = K_{cy}^{-1}((P_c - P_0)A_{cy} + F_{cy,0} - K_u u) + y_{max} \qquad | \; 0 \leq y \leq y_{max} \tag{1.48}$$

$$z = K_{cz}^{-1}((P_s - P_0)A_{sz} - F_{cz,0} - (P_c - P_0)A_{cz}) \qquad | \; 0 \leq z \leq z_{max} \tag{1.49}$$

$$v = K_{sv}^{-1}(A_{sv}(P_s - P_0) - F_{sv,0}) \qquad | \; 0 \leq v \leq v_{max} \tag{1.50}$$

The bulk moduli of the oil for the volumes s, p and c are described by equation 1.51-1.53.

$$\beta_s = \frac{(1-\alpha) \cdot exp(\frac{P_0 - P_s}{\beta_0}) + \alpha \cdot (\frac{P_0}{P_s})^{\frac{1}{n}}}{\frac{1-\alpha}{\beta_0} \cdot exp(\frac{P_0 - P_s}{\beta_0}) + \frac{\alpha}{n \cdot P_0} \cdot (\frac{P_0}{P_s})^{\frac{n+1}{n}}} \tag{1.51}$$

$$\beta_p = \frac{(1-\alpha) \cdot exp(\frac{P_0 - P_p}{\beta_0}) + \alpha \cdot (\frac{P_0}{P_p})^{\frac{1}{n}}}{\frac{1-\alpha}{\beta_0} \cdot exp(\frac{P_0 - P_p}{\beta_0}) + \frac{\alpha}{n \cdot P_0} \cdot (\frac{P_0}{P_p})^{\frac{n+1}{n}}} \tag{1.52}$$

$$\beta_c = \frac{(1-\alpha) \cdot exp(\frac{P_0 - P_c}{\beta_0}) + \alpha \cdot (\frac{P_0}{P_c})^{\frac{1}{n}}}{\frac{1-\alpha}{\beta_0} \cdot exp(\frac{P_0 - P_c}{\beta_0}) + \frac{\alpha}{n \cdot P_0} \cdot (\frac{P_0}{P_c})^{\frac{n+1}{n}}} \tag{1.53}$$

The three phase induction motor with FOC control is modelled as defined in section 1.3.2: Dynamic Model of Three Phase Induction Motor & Controller, while the loss model is as defined in section 1.3.3: Loss Model.

In conclusion, the detail and accuracy of the dynamic model is deemed sufficient for control development.

2 Problem Statement

Based on the introduction of the hydro gear test bench and the development of a dynamic model, the main purpose of this project is to develop a control method, that allows for tracking a pressure reference, while improving the system efficiency. In order to do so, an equivalent conventional hydraulic power unit needs to be established, such that it can form a benchmark for the developed control schemes. Based on this, the following problem is stated:

How can the introduced hydro gear be controlled with the aim of tracking a pressure reference while increasing the system efficiency?

The solution strategy will be to develop robust non-linear control algorithms, as the hydro gear is highly non-linear and the loss model even more so. Robustness of the control towards modelling inaccuracies and disturbances are prioritized leading to the choice of a sliding mode control approach. Linear analysis and linear control is not considered as it is deemed that the linearised model will be highly dependent on the linearisation points.

The controllers should aim for being industrially applicable, as to increase the relevance of the solution.

System Capability Analysis by Implying Steady State 3

In this chapter, the system capabilities will be mapped as to analyse the system characteristics and performance. In order to develop the maps, steady state will be implied. These maps will focus on the relation between the inputs, the output pressure and the system efficiency.

The steady state solution is based on setting the state-derivatives of the dynamic equations to zero. Then the steady state solution can be solved directly from the resulting algebraic equations according to 3.1.

$$\text{equation 1.36} \rightarrow 0 = Q_{ts} - Q_{st} - Q_{sp} - Q_{sc} - Q_{out} \tag{3.1a}$$
$$\text{equation 1.37} \rightarrow 0 = Q_{sp} - Q_{pt} \tag{3.1b}$$
$$\text{equation 1.38} \rightarrow 0 = Q_{sc} - Q_{ct} \tag{3.1c}$$
$$\text{equation 1.39} \rightarrow 0 = F_{sx,0} + K_{sx}(x_{max} - x) + A_{sx}P_s - A_{px}P_p \tag{3.1d}$$
$$\text{equation 1.40} \rightarrow 0 = \tau_{em} - D_s K_{\theta p} x(P_s - P_t) - B_\omega \omega_m \tag{3.1e}$$
$$\text{equation 1.17a} \rightarrow 0 = -\frac{R_s(L_m \Psi_{rd} - L_r \Psi_{sd})}{\sigma_{IM}} + \Psi_{sq}\omega_s + U_{sd} \tag{3.1f}$$
$$\text{equation 1.17b} \rightarrow 0 = -\frac{R_s(L_m \Psi_{rq} - L_r \Psi_{sq})}{\sigma_{IM}} - \Psi_{sd}\omega_s + U_{sq} \tag{3.1g}$$
$$\text{equation 1.17c} \rightarrow 0 = -\frac{R_r(L_m \Psi_{sd} - L_s \Psi_{rd})}{\sigma_{IM}} + \Psi_{rq}\omega_\Delta \tag{3.1h}$$
$$\text{equation 1.17d} \rightarrow 0 = -\frac{R_r(L_m \Psi_{sq} - L_s \Psi_{rq})}{\sigma_{IM}} - \Psi_{rd}\omega_\Delta \tag{3.1i}$$

Due to the presence of the closed loop FOC, the assumption $\omega_m = \omega_{m,ref}$ is initially set. This is done as the implemented PI-controllers in the FOC-scheme will diminish any steady state error. Then the states P_s, P_p, P_c, x, I_{sq}, I_{rd}, I_{rq}, U_{sd} and U_{sq} can be solved for.

3.1 Handling State Saturations

There are three states, whose saturations are deemed significant for the system characteristics and performance. These are the swash plate control piston displacement, x, the electrically actuated pressure relief valve displacement, y, the pressure control valve displacement, z, and the output pressure relief valve displacement, v, described by the inequalities of equation 3.2-3.5.

$$x_{min} \leq x \leq x_{max} \tag{3.2}$$
$$0 \leq y \leq y_{max} \tag{3.3}$$
$$0 \leq z \leq z_{max} \tag{3.4}$$
$$0 \leq v \leq v_{max} \tag{3.5}$$

Saturation of the torque delivered by the induction motor is not necessary to account for, as the induction motor is dimensioned for handling transients at high pressures. In steady state, the maximum load torque delivered by the pump, disregarding friction, is 54 [Nm] at 188.6 [bar]. With a maximum torque of 118.7 [Nm], the surplus makes considering torque saturation during steady state unnecessary.

These saturations can be implied in the steady state solution in different ways. One way could be to solve for steady state iteratively by:

1. Solve equation 3.1a-3.1i.
2. Check the solution for saturation violations:
   - If any, then set the states in concern to their nearest saturated value and *update* the system of equations to be solved.
   - Else stop and save the solution.
3. Solve the updated system and go to item no. 2.

When setting e.g. the state x to be constant, the system of equations is reduced by one equation, in this case equation 3.1d is removed. This is what is meant by *update* in item no. 2.

By practical implementation it is found that the algebraic complexity of equation 3.1a-3.1i makes an algebraic solution unfeasible. Further, by evaluating with numerical solvers, the ill conditioning of the system renders the solution to be of poor quality while requiring excessive computation time. Hence the steady state solution is produced by simulation of the dynamic system.

The AAU compute cloud, CLAAUDIA, is utilized to simulate $64^3 = 262.144$ solutions which will be presented in the following section.

The steady state solution is created as a sweep of the two inputs u, $\omega_{m,ref}$ and the load valve input l, each with a resolution of 64 equally spaced steps. As to plot the system capabilities each capability map is created with constant output powers 1, 5 and 10 [kW]. This is done as opposed to e.g. constant load valve input l, where the output flow will be pressure dependent or constant output flow Q_{out} where the output power yet again will be pressure dependent.

In the following sections the results are mainly displayed as 3D scatters with colours indicating state saturations. 3D scatters are chosen as the data folds on top of itself, out-ruling the contour plot and the like as options.

3.2 Input-Pressure Dependence

In figure 3.1 the pressures P_s, P_p and P_c are depicted as function of the inputs u and ω_m at 1 [kW] output power.

The saturation of the output pressure relief valve displacement v is stated somewhat counter-intuitively. When $v = 0$ it is regarded unsaturated as it is actually the output pressure P_s that is of interest. When $v > 0$ it is regarded as saturated as this causes the pressure relief valve to open, effectively saturating the pressure P_s. Therefore, the black dots noted as "No Saturation" mean that x, y and z are between their bounds, while $v = 0$.

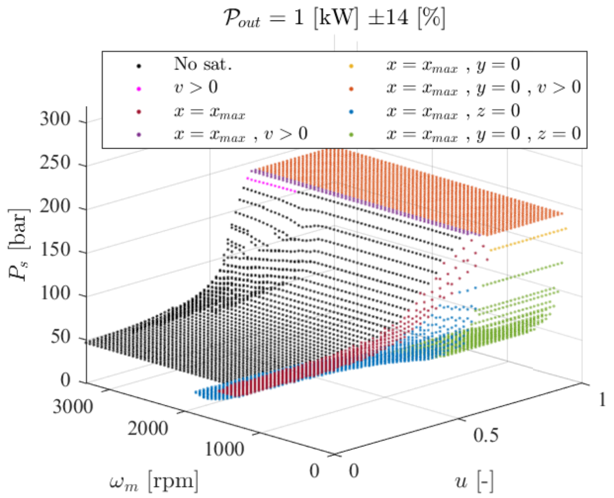

(a) P_s.

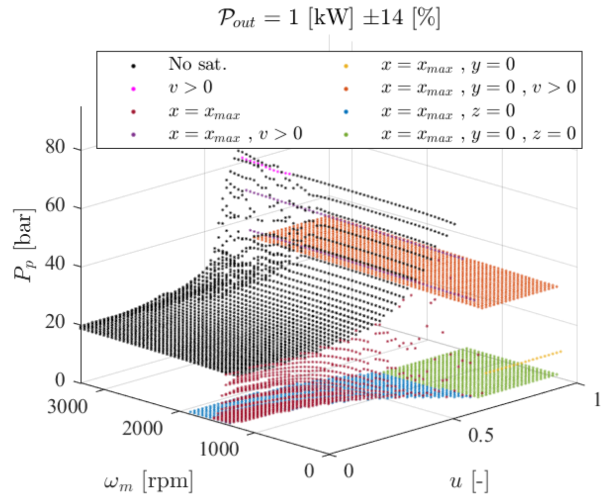

(b) P_p.

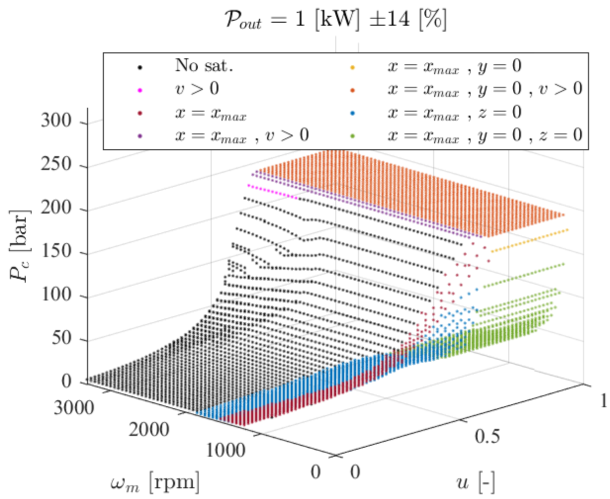

(c) P_c.

Figure 3.1: Input-pressure dependence at 1 [kW] output power.

Main points of the results are discussed in the following bullets:

- In the non-saturated region (•), the pressures are nearly invariant to the rotor speed ω_m while they are variant to the control input u. This is exactly the main functionality of the system control unit.
- In the non-saturated region (•), the swash plate displacement x is inverted with the progression of the rotor speed ω_m, being that it starts from $x = x_{max}$ at low speed and moves towards $x = x_{min}$ while the speed increases.
- Consider the boundary between the non-saturated region (•) and the region of $x = x_{max}$, (•). The reason why the hydro gear is able to control the pressure P_s through the control input u is, that at this boundary u almost exclusively control the leakage through the control unit, being the flow Q_{ct}. Hence, here the pressure is controlled through varying the leakage.
- A large part of the saturated regions folds beneath the non-saturated region. The concept that different pressures can be realized with the same inputs is due to different load valve

openings. Hence the system can output 1 [kW] at the saturated states $x = x_{max}$, $z = 0$ (•) by a relatively large load flow but relatively low pressure. Meanwhile it can output 1 [kW] with no state saturations (•) by a relatively low load flow and high pressure. Both with the same inputs.

- An output of 1 [kW] can be realized in most of the input space.

In figure 3.2 the pressures P_s, P_p and P_c are depicted as function of the inputs u and ω_m at 5 [kW] output power.

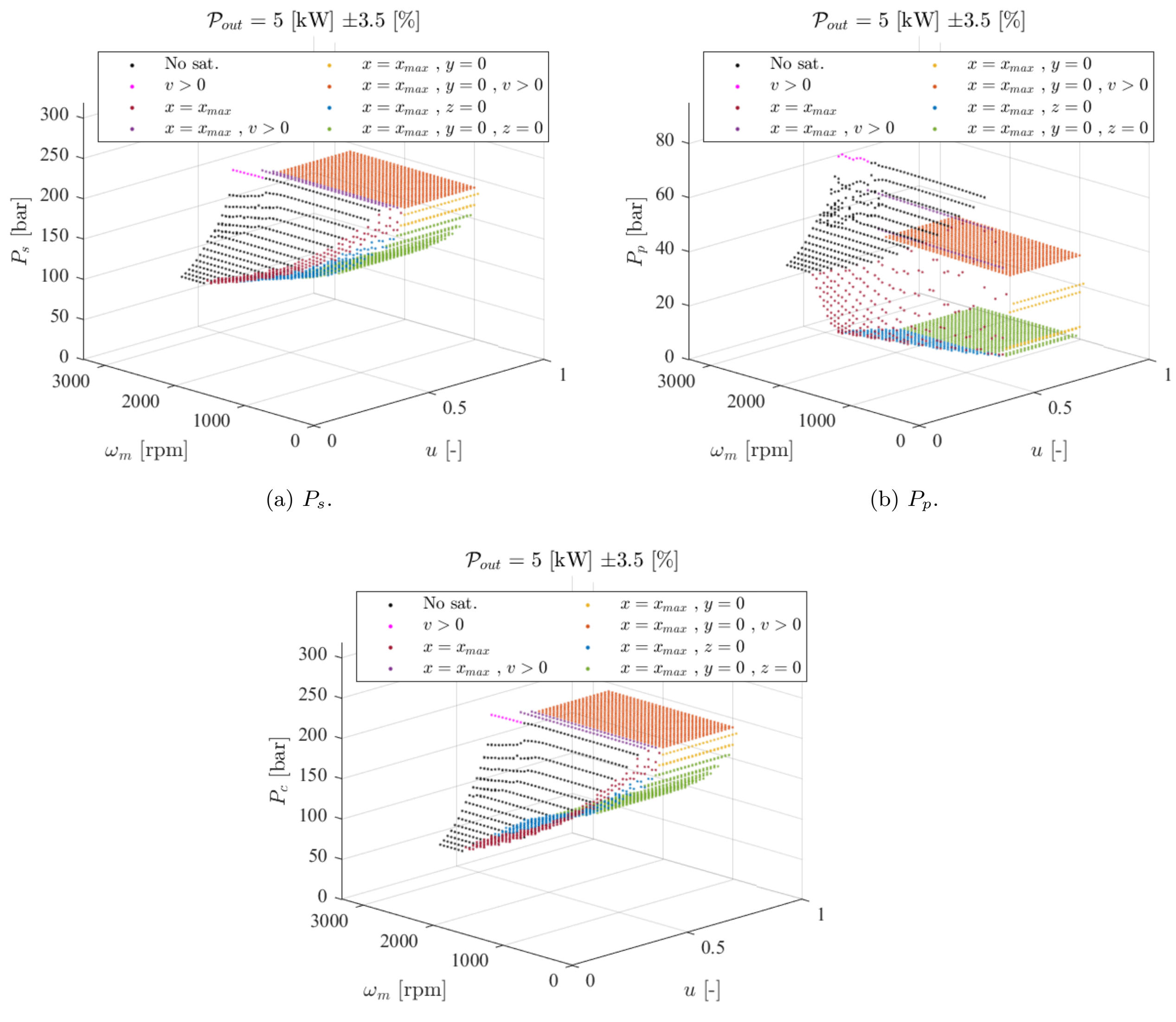

(a) P_s.

(b) P_p.

(c) P_c.

Figure 3.2: Input pressure dependence at 5 [kW] output power.

Main points of the results are discussed in the following bullets:

- An output of 5 [kW] can be realized in less of the input space compared to 1 [kW]. Further, the region of the input space that can realize an output of 5 [kW] is closest to the 'corner' $(u, \omega_m) = (1, 3300)$.
- In steady state, the output pressure relief valve almost works like an ideal pressure saturation as the regions including $v > 0$, namely (•), (•) and (•) are nearly constant

with respect to P_s.

In figure 3.3 the pressures P_s, P_p and P_c are depicted as function of the inputs u and ω_m at 10 [kW] output power.

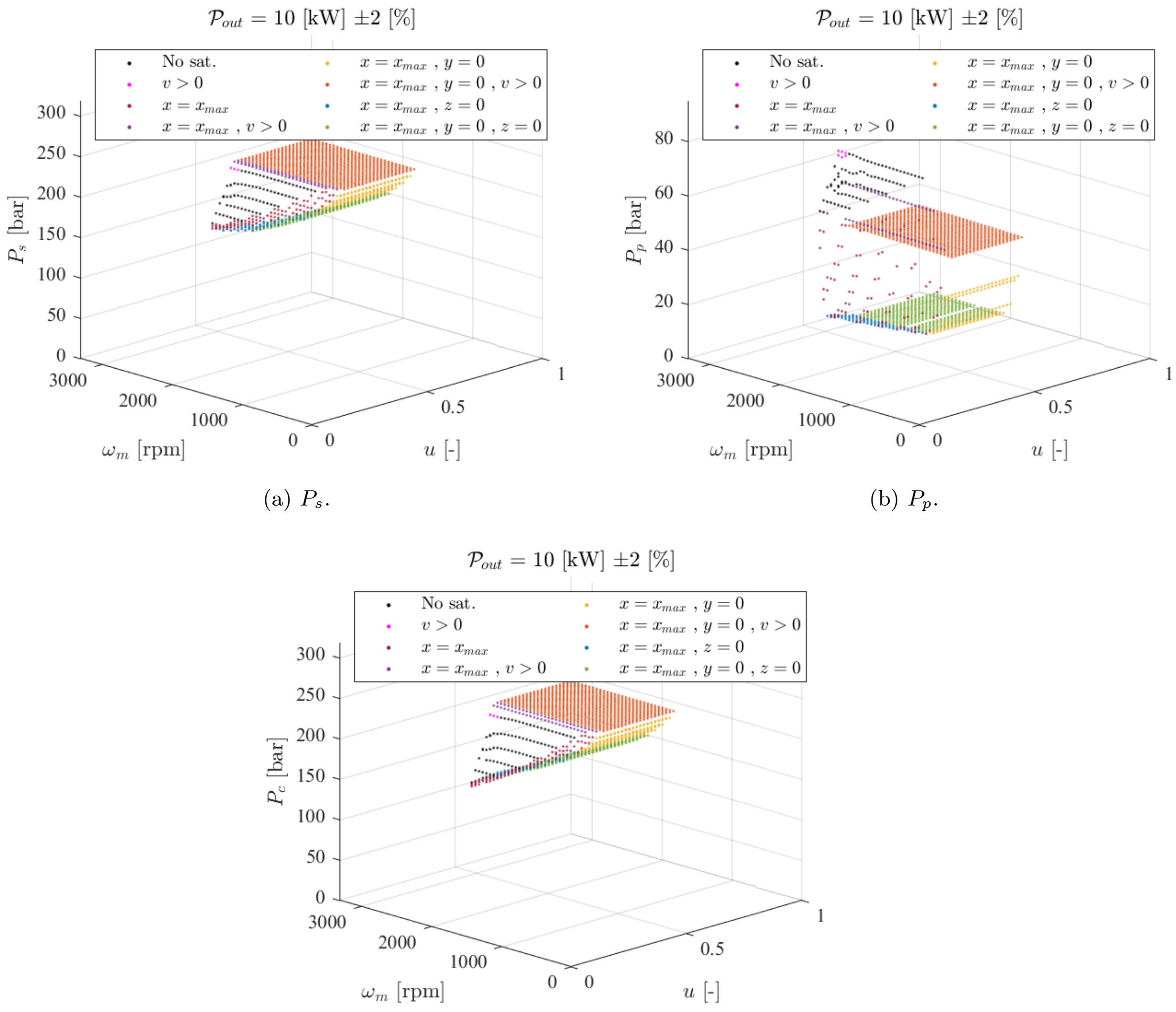

(a) P_s.

(b) P_p.

(c) P_c.

Figure 3.3: Input pressure dependence at 10 [kW] output power.

Main points of the results are discussed in the following bullets:

- An output of 10 [kW] can be realized in even less of the input space compared to 5 and 1 [kW], near the 'corner' $(u, \omega_m) = (1, 3300)$.
- Within the shaft speed bounds it requires an output pressure $P_s > 100$ [bar] to realize an output power of 10 [kW]. The speed bound is set by the pump, while the induction motor is able to reach 9000 [rpm].

In figure 3.4, the quite consistent invariance of the u-P_s relation to varying speed and output power is illustrated. This is indeed, only the case within the non-saturated region.

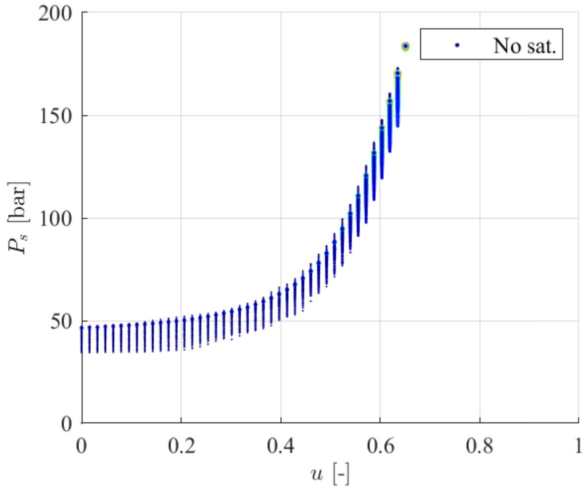

(a) u-P_s relation.

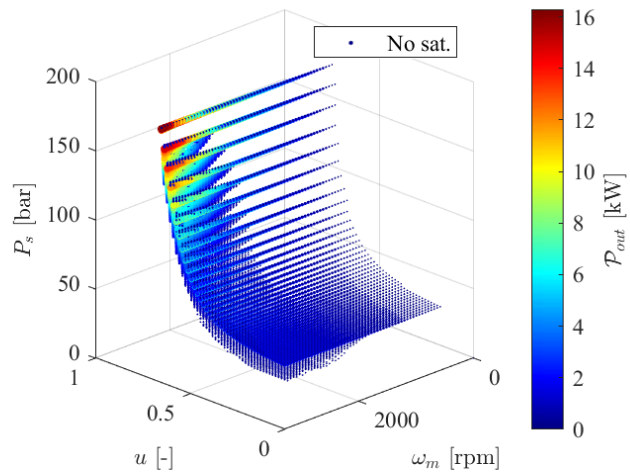

(b) Input-P_s relation.

Figure 3.4: The input-P_s relation for all output powers in the non-saturated region, emphasising the quite consistent invariance of the u-P_s relation to varying speed and output power.

As seen, the highest value of the control input while having no saturations is $u = 0.65$. Beyond this point, some state will saturate regardless of load and rotor speed.

In figure 3.5, the relation between the output power and output pressure is depicted while the bounds of each state saturation region is illustrated. For this figure $v > 0$ is disregarded.

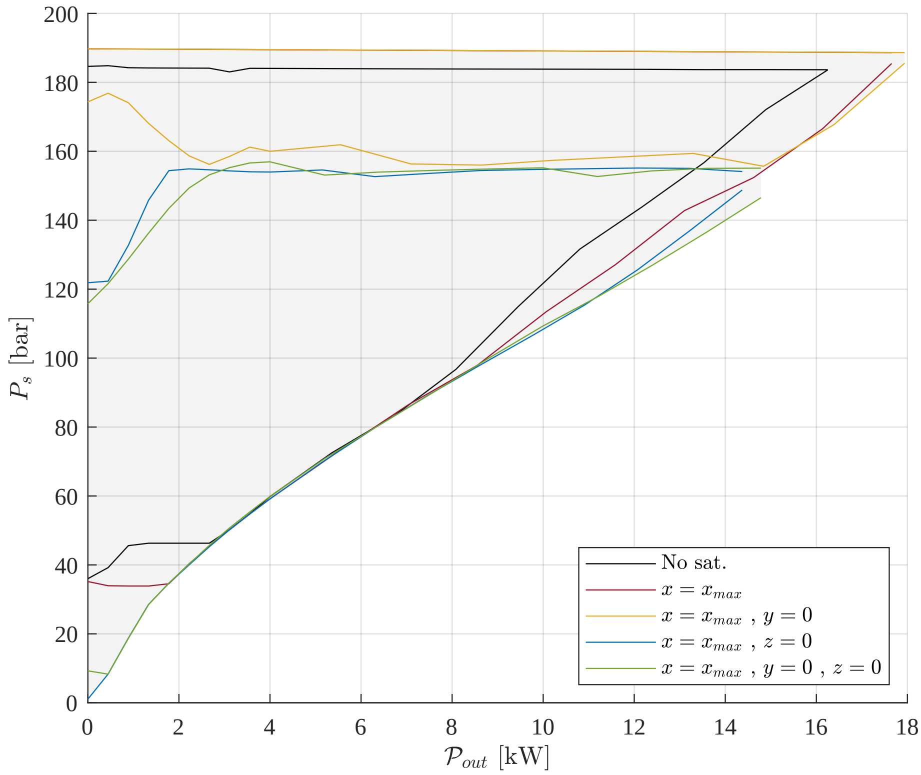

Figure 3.5: $\mathcal{P}_{out}$-P_s relation with the bounds of each state saturation region marked. $v > 0$ is disregarded. The state saturation regions are displayed as a grey area with upper and lower bounds according to the lines. E.g. the region $x = x_{max}$, $y = 0$ (●) is lower bounded by approx. 160 [bar] and upper bounded by approx. 188 [bar] marked by the lines.

Main points of the results are discussed in the following bullets:

- The non-saturated zone (●) is capable of reaching most of the system pressure capability.
- Low output pressures $P_s < 35$ [bar] are only obtained when $x = x_{max}$ and $z = 0$ being (●) and (●). In the region (●) the pressure P_s can be controlled through both ω_m and u while in the region (●), P_s is invariant to u leaving it only controllable through ω_m.
- High output powers $\mathcal{P}_{out} > 15$ [kW] are not obtainable while $z = 0$.

3.3 Input-Efficiency Dependence

In this section, the dependency between the inputs and the system efficiency is mapped. In steady state, the system efficiency is defined as the ratio of the output and input powers, efficiency$= 100\frac{\mathcal{P}_{out}}{\mathcal{P}_{IM,in}}$. For reference, the highest attained efficiency is 83.87 [%] when the load is $l = 0.2$ [-] and the inputs are $u = 0.69$ [-] and $\omega_m = 1892$ [rpm]. At this point, the output power is 8.74 [kW], corresponding to 74 [%] of the rated power of 11.83 [kW]. As shall be seen in the following section, similar efficiencies are obtainable through most of the output power range. In figure 3.6 the system efficiency is depicted as function of the inputs at 1 [kW] output power.

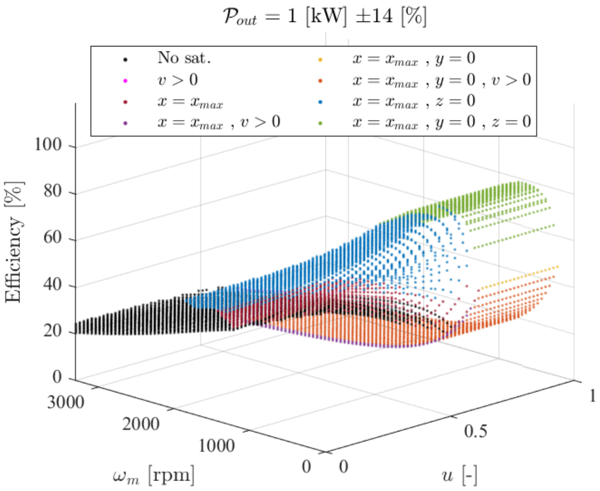

(a) Seen from 'input-origin'.

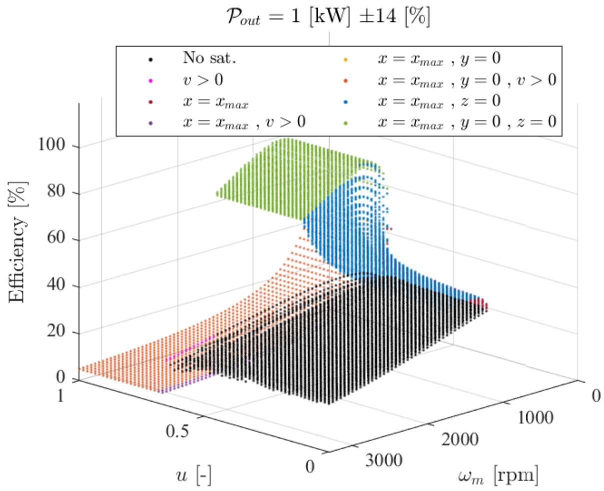

(b) Rotated 90 [°] CCW.

Figure 3.6: Input efficiency dependence at 1 [kW].

Main points of the results are discussed in the following bullets:

- In the non-saturated region (•), the obtainable efficiency is in the range 18-44 [%].
- The greatest efficiency of 78.1 [%] is obtained in the region of $x = x_{max}$, $y = 0$ and $z = 0$, (•), though from the input pressure dependency plots this region is only able to realize pressures in the range 21-132 [bar]. One of the reasons for the high efficiency in this range is that the flows Q_{ct} and Q_{pt} are zero as $y = 0$ and $z = 0$. These flows contribute to the functioning of the hydraulic control unit, but in relation to the system efficiency they can be regarded as leakages, through which power dissipates.
- The system is generally most efficient in the regions of $x = x_{max}$, without $v > 0$, being (•), (•), (•) and (•). In these regions, the pump can be regarded as a variable speed, fixed displacement pump.

In figure 3.7 the system efficiency is depicted as function of the inputs at 5 [kW] output power.

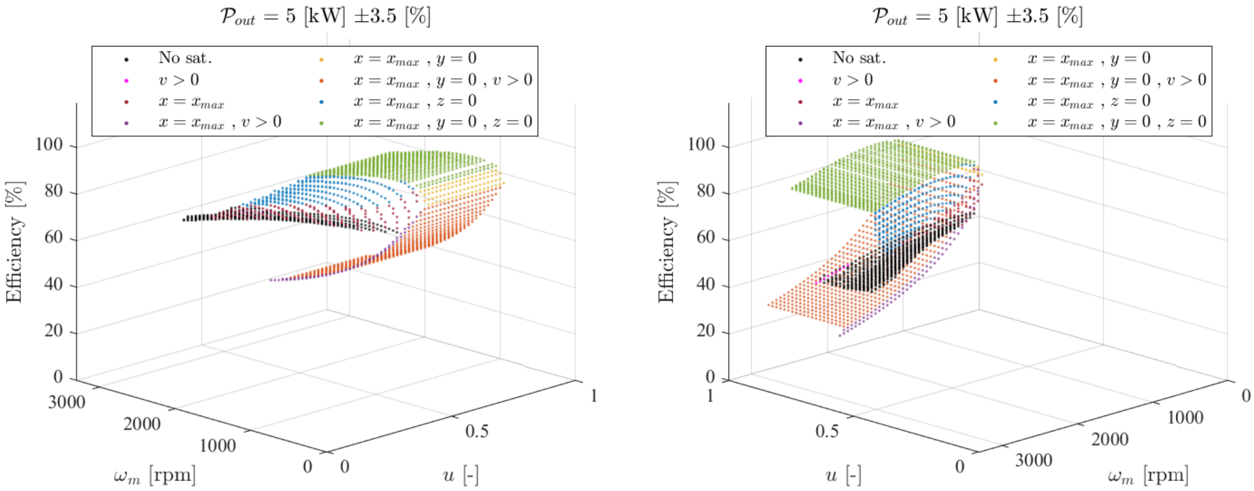

(a) Seen from 'input-origin'. (b) Rotated 90 [°] CCW.

Figure 3.7: Input efficiency dependence at 5 [kW].

Main points of the results are discussed in the following bullets:

- In the non-saturated region (•), the obtainable efficiency is in the range 53-64 [%].
- The efficiency layout is similar to that of 1 [kW], though as mentioned for the pressure plots, a smaller region of the input ranges is able to realize the larger output power.

In figure 3.8 the system efficiency is depicted as function of the inputs at 10 [kW] output power.

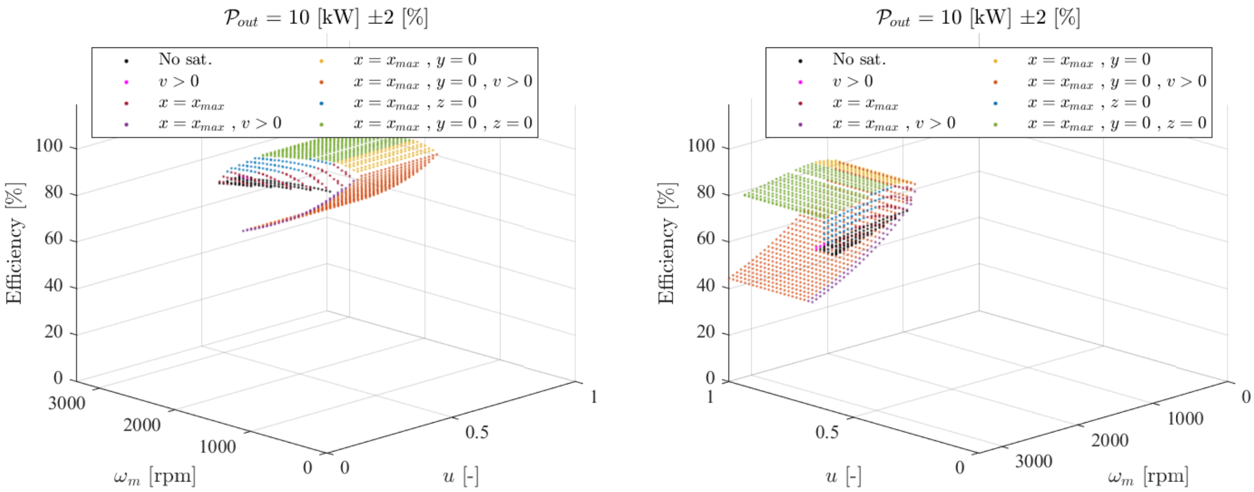

(a) Seen from 'input-origin'. (b) Rotated 90 [°] CCW.

Figure 3.8: Input efficiency dependence at 10 [kW].

Main points of the results are discussed in the following bullets:

- In the non-saturated region (•), the obtainable efficiency is in the range 67-73 [%].
- The efficiency layout is similar to that of 1 and 5 [kW], though an even smaller region of the input ranges is able to realize the larger output power.

In figure 3.9, the output power to system efficiency dependency is depicted. For this figure, $v > 0$ is disregarded.

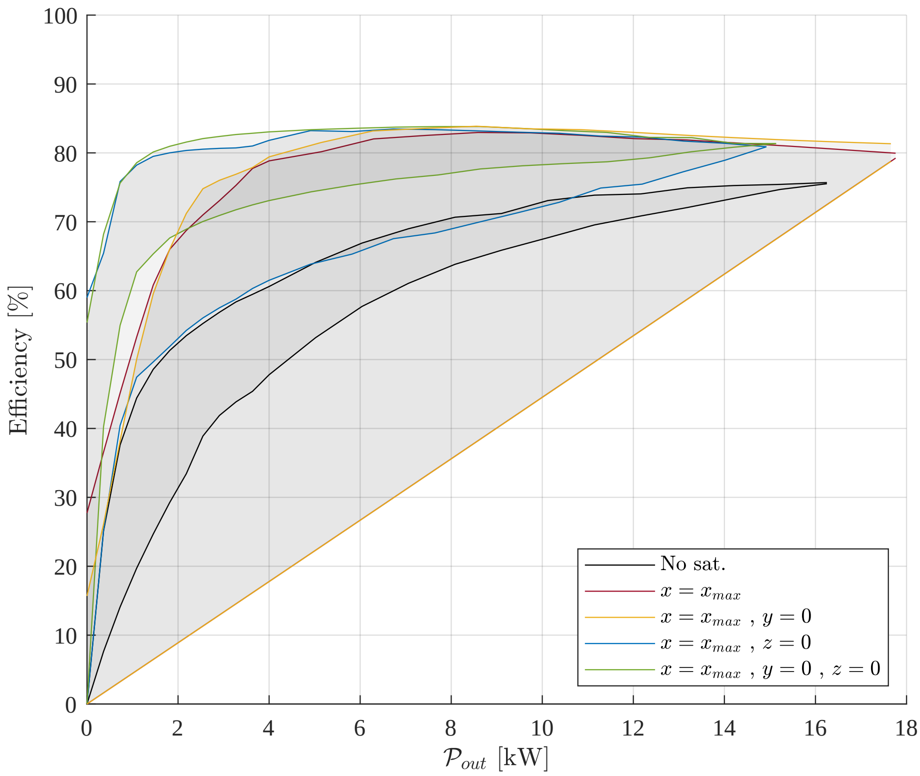

Figure 3.9: Output power to system efficiency dependency, where $v > 0$ is disregarded. The state saturation regions are displayed as a grey area with upper and lower bounds according to the lines. Note, the lower bound of the region $x = x_{max}$, $y = 0$ (●) coincides with the lower bound of the region $x = x_{max}$ (●).

Main points of the results are discussed in the following bullets:

- The non-saturated region is a relatively narrow banana-shaped region in the output power system efficiency dependency. I.e. the efficiency variation is not very large when the output power is above 4 [kW]. If the control is restricted to avoid state saturations, the best efficiency is not very good in the low output powers and the possibility of improving the efficiency is quite small in the high output powers.
- From the upper bounds of each region it can generally be stated that the more states that are saturated, the better a system efficiency is obtainable.

3.4 Pressure-Efficiency Dependence

In this section, the relation between the output pressure and the system efficiency is investigated. In figure 3.10 this relation is depicted, with $v > 0$ disregarded.

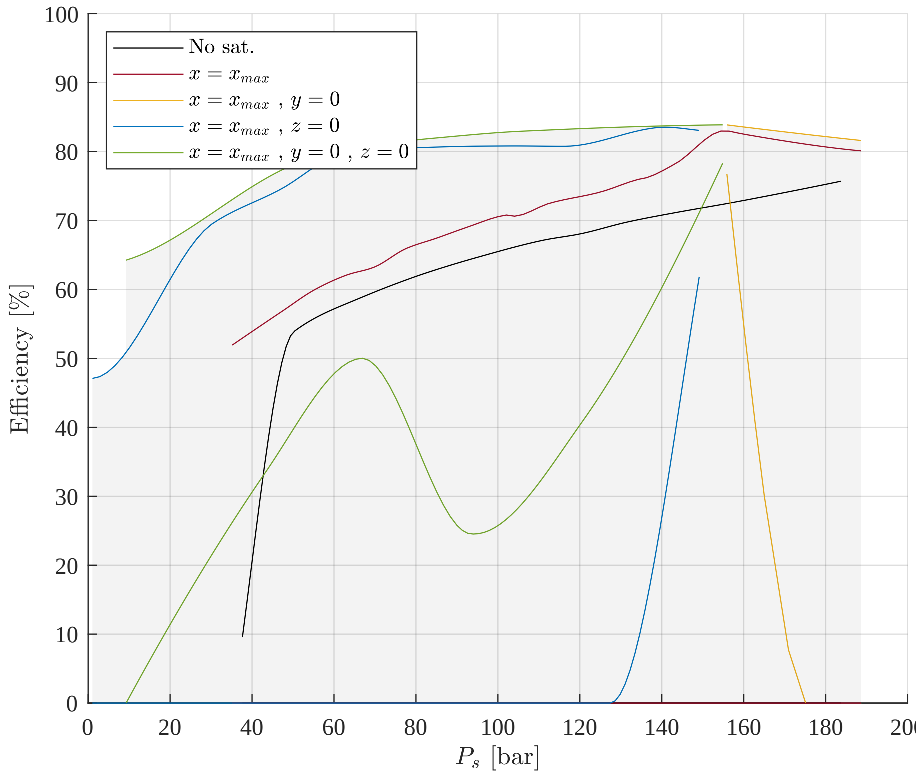

Figure 3.10: P_s-efficiency relation with the bounds of each state saturation region marked. $v > 0$ is disregarded. The state saturation regions are displayed as a grey area with upper and lower bounds according to the lines. Note, the lower bound of the non-saturated region (•) and the region of $x = x_{max}$ (•) coincide at 0 [%] efficiency.

Main points of the results are discussed in the following bullets:

- As for the result of the output power efficiency dependence it can generally be concluded that an increased efficiency is obtained as the number of saturations are increased.
- The lower bound to the region of $x = x_{max}$, $y = 0$ and $z = 0$ (•) is at efficiencies rather close to the upper bound of the non-saturated region (•). From figure 3.9 most of this lower bound must correspond to output powers below 1 [kW] as this is the only region of less than approx. 64 [%] efficiency.

3.5 Case: Holding High Pressure at Zero Load Flow

From the previous results, it seems likely that the system is generally most efficient when the input $u \in \{0.65, 1\}$. In this range, the pressure is nearly invariant to u, leaving the pressure to be controlled through the shaft speed ω_m. By doing this the pump will effectively function as a fixed displacement pump.

A frequent use-case of any HPU is to hold a high pressure at very low or even no flow. It is interesting to evaluate the system losses at zero load flow, as holding a high pressure for a fixed displacement pump requires very low shaft speed. This low shaft speed and high torque due to the high pressure, does intuitively not seem like the most efficient solution, as this will draw a high current in the induction motor, likely yielding high losses.

In figure 3.11, the output pressure, P_s, and losses in the hydro gear at $\mathcal{P}_{out} = 0$ are depicted.

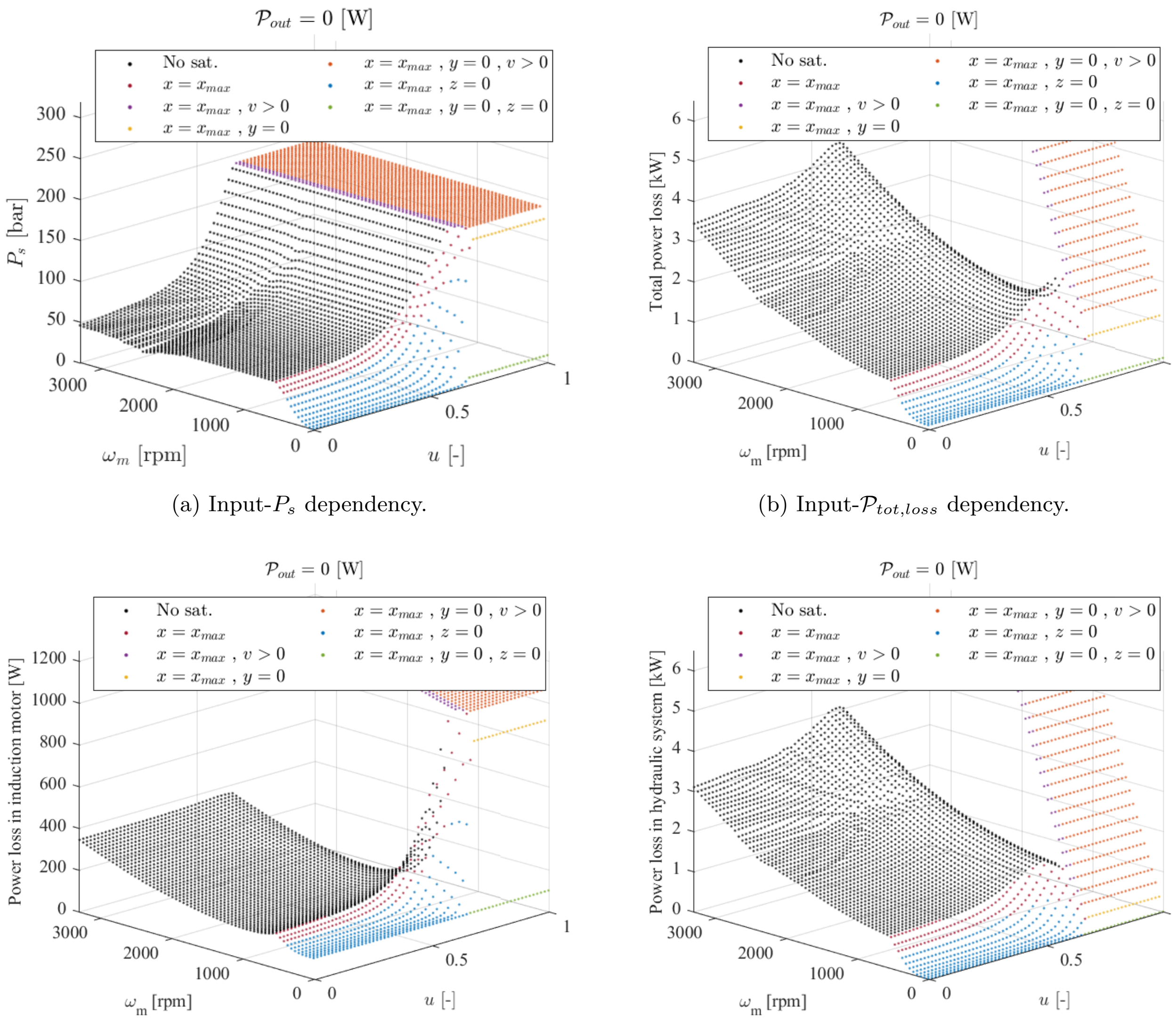

(a) Input-P_s dependency.

(b) Input-$\mathcal{P}_{tot,loss}$ dependency.

(c) Input-$\mathcal{P}_{IM,loss}$ dependency.

(d) Input-$\mathcal{P}_{hyd,loss}$ dependency.

Figure 3.11: The output pressure, P_s, and losses in the hydro gear at $\mathcal{P}_{out} = 0$.

In case one chooses to set $P_s = 165$ [bar], there are indeed infinite input combinations along a line stretching across the non-saturated zone (•) and into the zones of $x = x_{max}$ (•), $x = x_{max}$ and $z = 0$ (•) and lastly $x = x_{max}$, $y = 0$ and $z = 0$ (•). From the total power loss it may look as if the lowest loss that realizes this pressure is in the saddle-point of the non-saturated zone (•) with the inputs $u = 0.62$ [-] and $\omega_m = 745$ [rpm]. Here, the total power loss is 2 [kW], composed of 284 [W] in the induction motor and 1.8 [kW] in the hydraulic system. But there is a point with less total losses. At the inputs $u = 0.68$ [-] and $\omega_m = 67$ [rpm] within the region of $x = x_{max}$ (•) the total losses are 1 [kW], composed of 330 [W] in the hydraulic system and 823 [W] in the induction motor. Hence, choosing the lowest speed, that allows the pump to realize the desired pressure, will generally yield fewer losses. As is seen from the example though, the induction motor will as a result of the low speed and high torque carry a larger portion of the combined losses as compared to choosing a higher speed. If a high pressure, zero load flow section is part of a load trajectory, the reduced losses will contribute to an increased system efficiency during the trajectory.

3.6 Summary

In the following bullets, the main conclusions of the system capability analysis are summarized:

- At the boundary between the non-saturated region (•) and the region of $x = x_{max}$, (•), u almost exclusively control the leakage through the control unit, being the flow Q_{ct}. Hence, here the pressure P_s is controlled through varying the leakage.
- The relation between u and P_s in the non saturated zone is not only close-to invariant to the shaft speed ω_m, but also to the output power $\mathcal{P}_{out}$, yielding that it would be feasible to invert this relation to realize an open loop control of the pressure, with some precision.
- If the hydro gear produces an output power $\mathcal{P}_{out} > 4$ [kW], the possible efficiency variation in the non-saturated region (•) is small, yielding that there is not necessarily much efficiency to gain by developing control algorithms that only allow to operate within this region.
- The hydro gear is generally most efficient when $x = x_{max}$ yielding that it operates like a variable speed, fixed displacement pump. Likewise for the case of $\mathcal{P}_{out} = 0$, the power losses are fewest when operating like a variable speed, fixed displacement pump.
- For the case of operating like a variable speed fixed displacement pump, the losses of the hydraulic system are greatly reduced due to the losses of the hydraulic control unit being reduced, while the losses in the induction motor are increased due to the increased torque on the motor.

Benchmark Method 4

In this chapter a benchmark method will be formed for quantifying the performance of the controllers that will be developed in chapter 5. In order to do so a load trajectory will be defined and the concept of a corresponding industrial-best-practice HPU, based on the existing hydro gear test bench, will be introduced. As to seek different solutions, two candidate HPU control structures are proposed. The system performance will be quantified as an RMS pressure tracking error and a system efficiency. These figures along with assessment of the applicability lead to the choice of one corresponding industrial-best-practice HPU which will be denoted the benchmark HPU (bHPU). Lastly, the control structure of the bHPU is implemented in the project test bench and the performance of the bHPU is validated experimentally.

4.1 Load Trajectory

In this section, the load trajectory for the efficiency benchmark will be formed. It will take offset in backwards reasoning based on general design rules attained from Bosch Rexroth, for designing a HPU for a specific load.

When dimensioning a HPU for a load, it is often dimensioned to be able to provide 20-30 [%] more power than the consumer will need, as to have a surplus of power to account for inaccuracies, system modifications, wear etc. [1]

The hydro gear test bench is rated for 42 [L/min] at 170 [bar], corresponding to 11.83 [kW] of output power. Taking offset in a 20 [%] surplus in the HPU, the load will be allowed to reach 9.5 [kW]. Recalling that the hydro gear test bench utilizes the output proportional valves as a load, the maximum allowable equivalent load valve input can be found to be $l = 0.191[-]$. At this load valve input and a pressure of 170 [bar], the output flow will be $Q_{out} = 33.6$ [L/min], which again corresponds to 9.5 [kW] output power.

From the steady state solution, it is known, that at zero pressure control input, $u = 0$ [-], and a speed high enough to reach the non-saturated zone (where no states are saturated), the pressure is just below 50 [bar]. Hence the pressure trajectory will be bounded between 50 and 170 [bar].

The concept of creating a pressure reference input allows for a load sensing consumer to adjust the supply pressure according to the load. In order to capture the influence of this in the efficiency benchmark, a load sense level is formulated with four discrete steps. When the load sense level is zero, it corresponds to no load sensing in which case the machine will be set to the highest required pressure level. The load sense level will hence forth be abbreviated LSL. Likewise, in order to capture the variation of the load level a such is formulated with four discrete steps, hence forth abbreviated as LL.

[1] From Bosch Rexroth A/S.

Based on this, the trajectories $P_{s,ref}$ and l_{ref} are created as seen in figure 4.1. The pressure reference data is based on ramps, while the load reference is a combination of ramps and a chirp sequence of 0-25 [Hz].

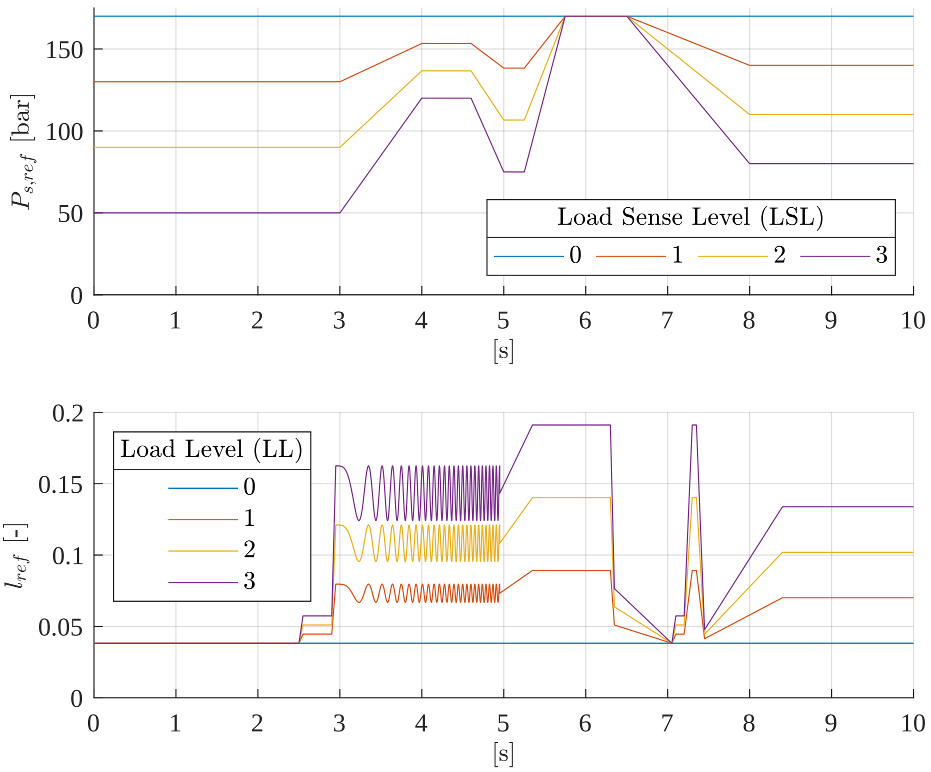

Figure 4.1: Load and pressure reference trajectories.

As seen, the first two seconds of the trajectories are constant. This is in order to allow any developed controller to converge if necessary. For LL3, the maximum resulting reference output power is 9.5 [kW]. In table 4.1 the minimum and maximum reference output powers are noted for all combinations of LSL and LL.

Table 4.1: Minimum and maximum reference output powers for all combinations of LSL and LL.

$^{min(\mathcal{P}_{out})}/_{max(\mathcal{P}_{out})}$		Load Sense Level (LSL) 0	1	2	3
Load Level (LL)	0	1892.8/1892.8	1262.3/1892.8	723.4/1892.8	295.5/1892.8
	1	1892.8/4416.5	1262.3/4416.5	723.4/4416.5	295.5/4416.5
	2	1892.8/6940.3	1262.3/6940.3	723.4/6940.3	295.5/6940.3
	3	1892.8/9464	1262.3/9464	723.4/9464	295.5/9464

As seen, an increasing load level yields an increasing maximum output power, while an increasing load sense level yields a decreasing minimum output power.

4.2 The Corresponding Fixed Speed, Variable Displacement HPU

In this section, a simple control method will be described that allows to use the hydro gear test bench to form a corresponding fixed speed variable displacement HPU.

The concept of a fixed speed machine arises from the notion of a conventional HPU, being supplied by the fixed frequency electric grid, though the frequency converter of the hydro gear does not allow for outputting a fixed frequency. As the torque speed curves of the induction motor are very steep in the operating range from zero slip to critical slip, see appendix B, it is assumed that a constant speed input will reproduce the main characteristics of the corresponding fixed frequency variable displacement HPU.

Since the test bench induction motor is a 6 pole machine the rotor speed would be 1000 [rpm] at zero slip if it were to be supplied directly from the 50 [Hz] grid. This would only be able to produce a theoretical maximum of 18 [L/min] and would not be suitable for comparison to the hydro gear. Therefore, the following section will define a suiting rotor speed for outputting the required capacity of the load trajectory.

4.2.1 Capacity Adjustment Through Choice of Rotor Speed

Since the load has a maximum of 9.5 [kW], then the HPU must be able to output 11.83 [kW] as to have a power surplus of 20 [%].

At the rated pressure, maximum swash plate displacement and assuming no hydraulic losses, a rotor speed of 2347 [rpm] would be enough to produce 11.83 [kW]. Only this would not be enough as hydraulic losses will reduce the actual output power. Therefore, the steady state solution is used to create a hydraulic efficiency plot as function of input speed. This is depicted in figure 4.2.

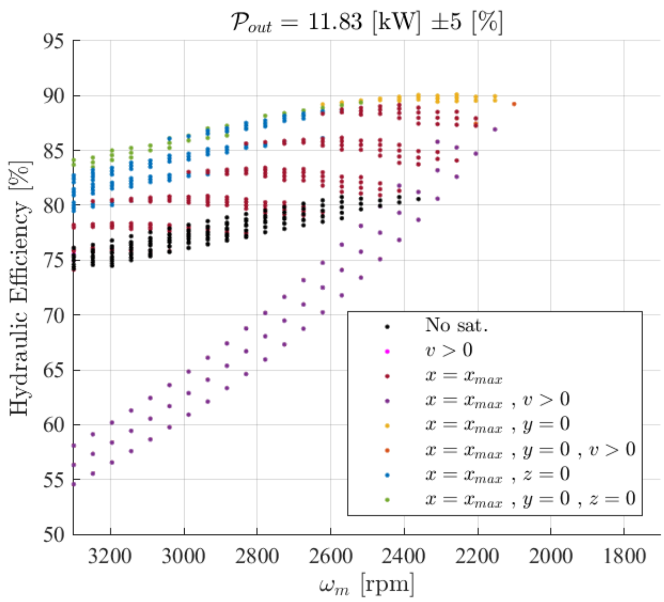

Figure 4.2: The hydraulic efficiency as function of rotor speed at 11.83 [kW] output power.

As seen, the hydraulic system yields a maximum efficiency of approximately 90 [%] in the speed range 2200-2700 [rpm]. As to be slightly conservative, an efficiency of 88 [%] is chosen. Hence, the final motor speed should be 2662 [rpm] to encompass the hydraulic losses. At this speed and pressure, the induction motor delivers 13.5 [kW] at the shaft, resulting in 11.83 [kW] hydraulic output power, which is a 20 [%] surplus with respect to the maximum load power. From the induction motor torque speed curves it is evident that the motor is theoretically capable of producing the maximum torque of 118.7 [Nm] at this speed. Hence the induction motor is capable of outputting its maximum 26.86 [kW], which will lead to current saturation and a actual maximum torque of 98.35 [Nm]. At 2662 [rpm] and an output pressure of 170 [bar] the load torque produced by the pump is 53.88 [Nm], hence the induction motor has a large surplus of torque to handle transients.

4.2.2 Pressure Control

Having defined a corresponding fixed frequency variable displacement HPU, this section will describe a control method that is aimed to represent a common solution in the industry. First, the open loop pressure control is introduced, as this is very simple and *may* be what the first versions of the installed pressure control unit was developed for. Then, exploiting the solenoid of the control unit to create a closed loop controller will increase performance and allow for tracking the varying pressure reference when the load sense level is not 0.

Open Loop Pressure Control

The simplest usage of the fixed frequency variable displacement HPU is to set a constant control input. Traditionally this would by done by manually increasing the control input till reaching a desired pressure. Then the built-in hydraulic pressure compensation of the control unit will maintain the set pressure under varying load conditions through varying the displacement of the swash plate control pistons. All of this can be realized without the need of a PLC.

This open loop method is then only made for tracking load sense level 0. The best control input for tracking LSL0 is $u = 0.635$. The pressure tracking under load level 3 is depicted in figure 4.3.

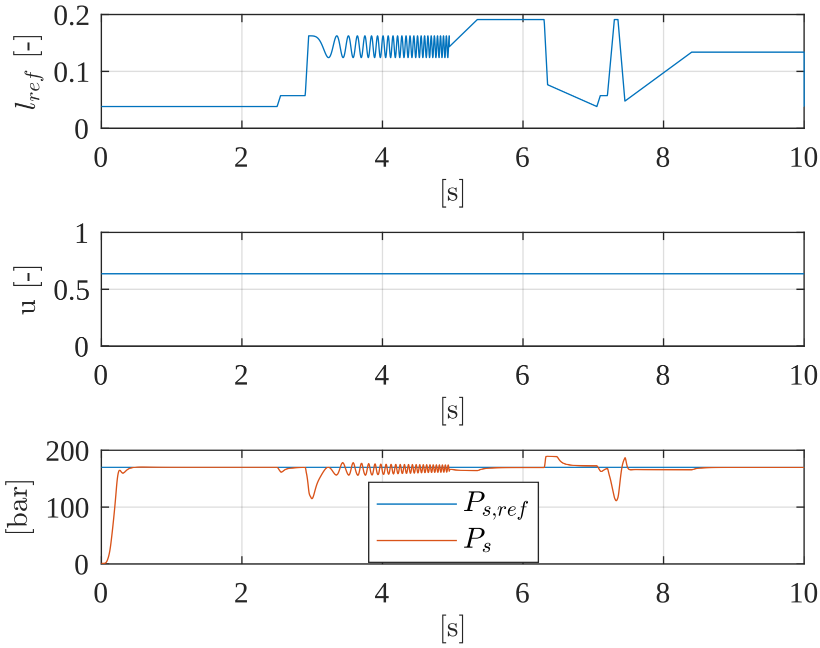

Figure 4.3: Simulated pressure response for constant inputs of u and $\omega_{m,ref}$ while subject to LL3 and LSL0, yielding the load and pressure references l_{ref} and $P_{s,ref}$ respectively.

As seen, the pressure variations due to the load of LL3 are quite large ranging up to 50 [bar].

Indeed it would be possible to invert the relation between u and P_s which was described in the steady state solution (figure 3.4) to allow for tracking LSL 1-3. But then, the control method will require a PLC to evaluate the inverted relation, making it more reasonable to choose a closed loop pressure control method which will potentially be able to attenuate the disturbance of the load.

Closed Loop Pressure Control

For the purpose of representing a common solution in industry a PID-controller with anti wind-up on the integrator will be implemented and tuned, while simply assuming stability of the zero pressure-tracking-error equilibrium point. The control structure will follow the block diagram of figure 4.4.

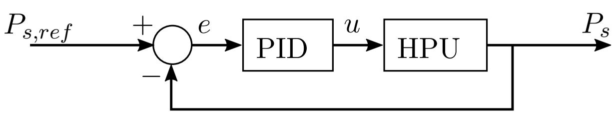

Figure 4.4: Block diagram of the closed loop pressure control for the fixed speed, variable displacement HPU.

Applying the tuned PID on the fixed speed, variable displacement HPU for the trajectory of LSL3 and LL3 yields the response of figure 4.5.

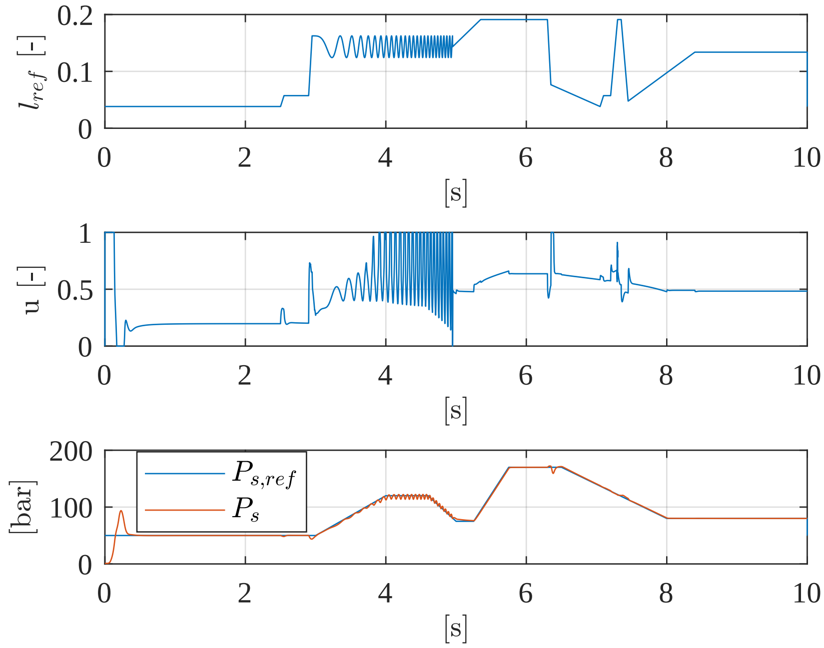

Figure 4.5: Simulated pressure tracking with the PID. The signal u displays rather high control activity in the effort to track the pressure reference $P_{s,ref}$ under the disturbance of the load l_{ref}.

As seen, the tuned PID offers quite good pressure tracking on the LSL3 reference during the quite significant disturbances introduced by LL3.

Based on this, a candidate benchmark HPU is proposed as a corresponding fixed speed, variable displacement HPU. The performance of the candidate will be quantified in section 4.4.

4.3 The Corresponding Variable Speed, Fixed Displacement HPU

In this section, an alternative to the more conventional fixed frequency, variable displacement HPU is proposed. The concept is based on studying the steady state efficiency results. Apparently, it is generally most efficient to apply the lowest possible speed, that is able to realize the reference pressure and at which $x = x_{max}$.

4.3.1 Realizing Fixed Displacement Through Choice of u

From the steady state solution it is noted, that all combinations of state saturations except the case $v > 0$, include the saturation of the swash plate displacement $x = x_{max}$. Further it is noted that any control input $u > 0.651$ will lead to state saturation. Effectively this means that for any $u > 0.651$ the system can be regarded as a fixed displacement HPU at steady state. What happens during transients is hard to generalize about, though it is clear that increasing u will decrease the likelihood of x leaving x_{max}.

Therefore, it is chosen to set $u = 1$, as this will most likely realize the concept of fixed displacement in all situations.

4.3.2 Pressure Control

For the purpose of representing a common solution in industry a PID-controller with anti wind-up on the integrator will be implemented and tuned, while simply assuming stability of the zero pressure-tracking-error equilibrium point. The control structure will follow the block diagram of figure 4.6.

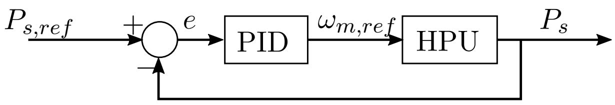

Figure 4.6: Block diagram of the closed loop pressure control for the variable speed, fixed displacement HPU.

Applying the tuned PID on the variable speed, fixed displacement HPU for the trajectory of LSL3 and LL3 yields the response of figure 4.7.

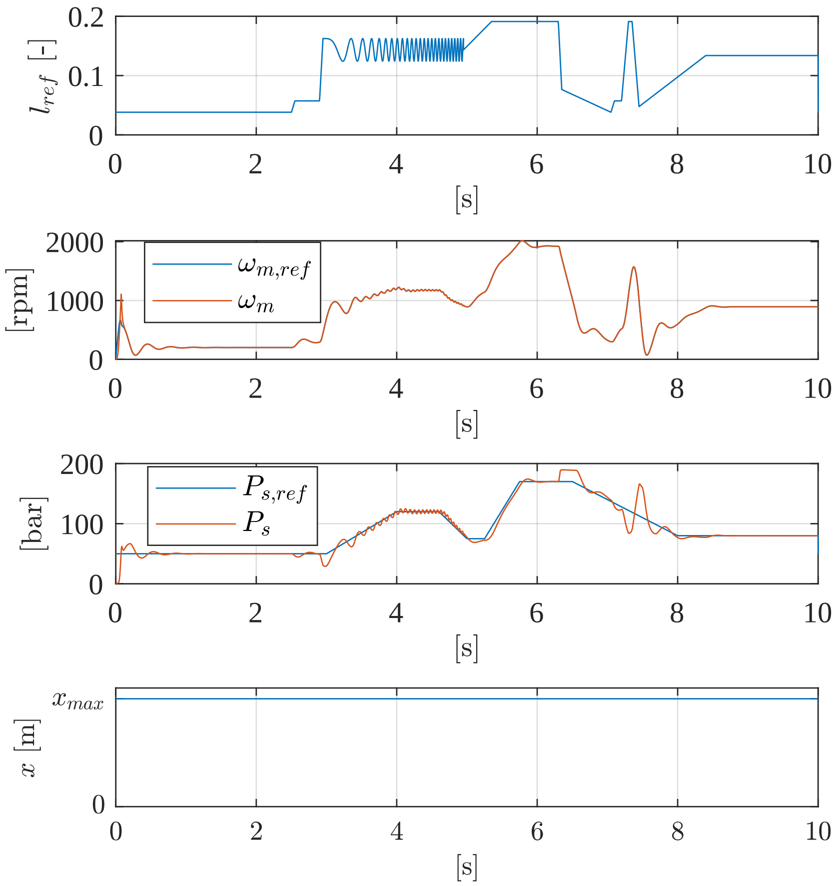

Figure 4.7: Simulated pressure tracking with the PID. Uppermost is the load reference l_{ref}, below is the reference shaft speed $\omega_{m,ref}$ and the simulated shaft speed ω_m, as controlled by the PID, in order to allow the pressure P_s to track its reference $P_{s,ref}$. Lowermost is the value of the swash plate control piston x.

As seen, the swash plate control piston displacement x is at its max throughout the trajectory as intended. The pressure tracking is less good than of the fixed speed variable displacement HPU. This along with efficiency figures will be quantified in the following section.

4.4 Performance Quantification: Pressure Tracking & System Efficiency

Two measures will be used to quantify the performance of the benchmark HPU candidates and the controllers which will be developed for the hydro gear. These will be the RMS tracking error and the system efficiency.

The first measure, the RMS pressure tracking error, is defined according to equation 4.1.

$$RMSe = \sqrt{\frac{1}{t_1 - t_0} \int_{t_0}^{t_1} (P_s - P_{s,ref})^2 dt} \tag{4.1}$$

Then the second measure, efficiency, is chosen as opposed to the loss energy. This is because efficiency makes it somewhat easier to compare the performance between different load cases. The standard, ISO 4409, defines a method of quantifying the efficiency of a pump [5]. This standard defines a volumetric and a hydro-mechanical efficiency which is the common terminology in the industry, though these figures cannot be regarded as energy conversion efficiencies, due to inconsistencies in their definitions with respect to the definition of the overall efficiency [6]. Furthermore, it only considers the pump itself, disregarding the remaining components of the hydraulic power unit as a system. In this project, three main loss components are taken into consideration, being the induction motor, the pump and the pressure control unit. The standard, ISO 14414, on the other hand defines how to asses the energy consumption of a pump system, though is not intended for quantifying comparable efficiency figures between solutions. Rather, it works as a road map of how to improve the efficiency of an installed pump system on site [7].

Therefore, this project defines the efficiency as a energy conversion figure as in equation 4.2.

$$\text{Efficiency} = 100 \cdot \frac{\int_{t_0}^{t_1} \mathcal{P}_{out} dt}{\int_{t_0}^{t_1} \mathcal{P}_{IM,in} dt} \tag{4.2}$$

For the load trajectory the integral limits are defined as $t_0 = 2$[s] and $t_1 = 10$[s].

To simplify the comparison between controllers these performance measures are averaged to give an average RMS pressure tracking error, $\overline{RMSe}$ and average efficiency $\overline{Eff}$.

4.4.1 Fixed Speed Variable Displacement HPU with Open Loop Pressure Control

As discussed previously, the open loop control of the fixed speed variable displacement HPU is not suitable for tracking a varying pressure reference. Therefore, this method is only evaluated for LSL0. The simulated results are stated in table 4.2.

Table 4.2: Simulated performance figures of the fixed speed, variable displacement HPU with open loop pressure control.

$RMSe$ [dbar] / $Eff.$ [%]		Load Sense Level (LSL) 0	1	2	3
Load Level (LL)	0	0/35.6	-	-	-
	1	28.3/48.3	-	-	-
	2	58/56.2	-	-	-
	3	96.3/61.4	-	-	-

Note, the unit [dbar] which is an abbreviation for *decibar*.

4.4.2 Fixed Speed Variable Displacement HPU with Closed Loop Pressure Control

Evaluating the performance figures across all combinations of LSL and LL yields table 4.3.

Table 4.3: Simulated performance figures of the fixed speed, variable displacement HPU with closed loop pressure control.

$RMSe$ [dbar] / $Eff.$ [%]		Load Sense Level (LSL) 0	1	2	3
Load Level (LL)	0	0/35.6	0.8/30.6	1.8/26.3	5.6/22.4
	1	1.4/48.5	1.7/43.1	2.5/38.3	5.8/33.7
	2	16.7/56.8	6.8/51.6	6.3/46.7	8.2/42
	3	52.3/62.5	26.5/57.6	17.3/53	16/48.2

As seen, the RMS-error varies from 0 to 5.23 [bar] while the system efficiency varies from 22.4 to 62.5 [%]. The average RMS error and efficiency is therefore:

$$\overline{RMSe} = 10.62[\text{dbar}] \tag{4.3}$$

$$\overline{Eff.} = 43.55[\%] \tag{4.4}$$

4.4.3 Variable Speed Fixed Displacement HPU

Evaluating the performance figures across all combinations of LSL and LL yields table 4.4.

Table 4.4: Simulated performance figures of the variable speed, fixed displacement HPU.

$RMSe$ [dbar] / $Eff.$ [%]		Load Sense Level (LSL) 0	1	2	3
Load Level (LL)	0	4.7/60.8	5.2/65	9.6/66	14.1/65
	1	42.9/70.1	43.1/73.7	42.2/74.6	41.1/74.1
	2	67.2/73.8	72.2/76.8	69.3/77.4	65/76.8
	3	88.5/75.1	92.4/77.7	91.7/77.9	85.9/77.1

As seen, the efficiencies are greatly increased as compared to the fixed speed variable displacement HPU, though the RMS tracking error is increased likewise. The average RMS error and efficiency is therefore:

$$\overline{RMSe} = 52.18[\text{dbar}] \quad (4.5)$$

$$\overline{Eff.} = 72.62[\%] \quad (4.6)$$

4.5 Choice of Benchmark HPU: Fixed Speed Variable Displacement HPU with Closed Loop Pressure Control

From the simulated results, it is chosen to use the fixed speed variable displacement HPU with closed loop pressure control to form the benchmark HPU.

It is clear, that this is the intended use of the pressure control unit, making it the likely preferred choice in industry.

Based on this, a benchmark for the hydro gear has been established. This benchbark HPU, will thus forth be abbreviated bHPU.

4.5.1 Experimental Measurement of the Input and Output Powers

The experimental setup does neither have measurement points that can measure the input power to the induction motor, $\mathcal{P}_{IM,in}$, nor the hydraulic output power, $\mathcal{P}_{out}$.

The frequency inverter drive does though provide a measurement of the DC-bus power consumption. In [1], the identification of the induction motor equivalent core resistance revealed that besides the consumption of the voltage source inverter which feeds the induction motor, there is a consumption of approx. 400 [W] by the integrated 24 [V] control voltage supply. These 400 [W] are an average of the 45 [s] sampled data, that the identification problem was based on. The integrated 24 [V] control voltage supplies the PLC, its expansion modules, the sensors and the valves. From the output proportional control valve data-sheet the maximum power consumption is defined to be 40 [W] [8] and from the control unit data-sheet the unit has a maximum power consumption of 18.5 [W] [9].

Based on this, the control signals are deemed to have a small influence on the power consumed by the integrated 24 [V] control voltage supply. Rather it is deemed, that the majority of the power is consumed by the PLC, its expansion modules and the sensors. Therefore, the 400 [W] are assumed to be constant.

Besides identifying the consumption of the integrated 24 [V] control voltage supply, the solution to the identification problem found that the switching losses of the voltage source inverter are diminishing. Hence, the induction motor input power is experimentally estimated according to equation 4.7.

$$\mathcal{P}_{IM,in} \approx \mathcal{P}_{DC} - 400 \quad (4.7)$$

There is no output flow-meter, therefore the output power is estimated based on the output flow model and the measured pressure according to equation 4.8.

$$\mathcal{P}_{out} \approx Q_{out}(P_s - P_t) \quad (4.8a)$$

$$\approx K_{out} l(|P_s - P_t|)^{3/2} sgn(P_s - P_t) \quad (4.8b)$$

The precision of the output flow model is deemed sufficient as the load valve is manufactured for having a linear control signal-flow characteristic.

4.6 Experimental Validation of the Benchmark HPU

During implementation of the PID for the bHPU, the relatively large amplitude of the pressure feedback noise required altering the control structure to a PI-Lead, thus adding an extra pole to avoid amplification of the high frequency noise. Furthermore, the proportional gain and the derivative gain had to be reduced drastically as to diminish the influence of the noise, while the integral gain could be persisted. The resulting pressure tracking for LL3 and LSL3 is depicted in figure 4.8, while the responses for the remaining 15 load trajectories can be assessed in appendix E.

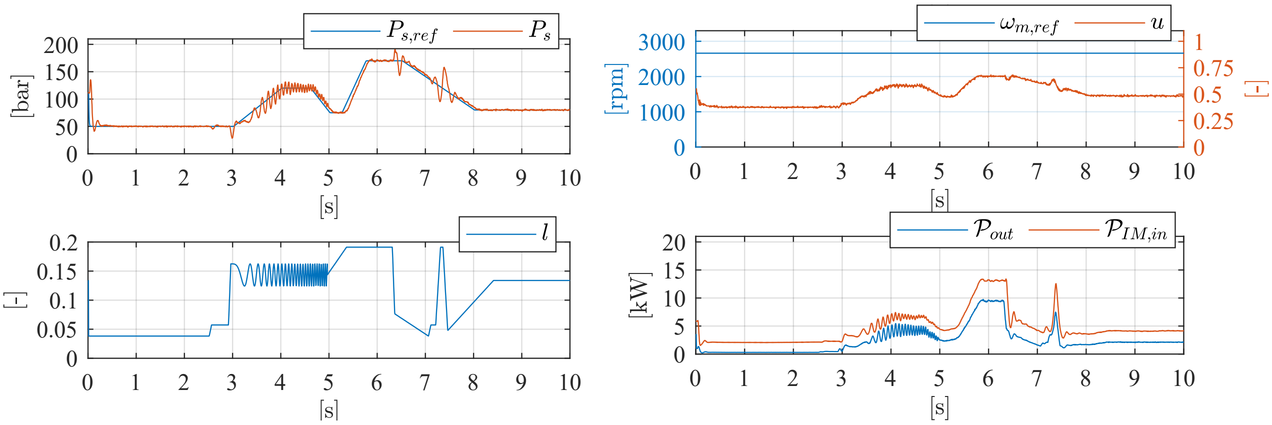

Figure 4.8: Measured pressure tracking of the bHPU.

As seen, the measured pressure tracking is quite deteriorated compared to the simulated. This is indeed due to the reduction of the proportional and derivative gains. Also visible is a much reduced control input activity, which in table 4.5 is seen to increase the system efficiency compared to the simulated.

Table 4.5: Measured performance figures of the bHPU.

$RMSe$ [dbar] / $Eff.$ [%]		Load Sense Level (LSL) 0	1	2	3
Load Level (LL)	0	11.7/38.6	15.8/35.9	28.1/32.5	46.5/28.5
	1	36.2/52.7	35/50.2	40/46.4	51.9/41.7
	2	65.4/60.2	59.2/58.3	58.5/54.7	63.7/50.1
	3	86.8/63.7	86.6/63.3	78.4/60.2	77.5/55.8

The average RMS error and efficiencies are evaluated to:

$$\overline{RMSe} = 52.58[\text{dbar}] \tag{4.9}$$

$$\overline{Eff.} = 49.54[\%] \tag{4.10}$$

The discrepancy between the simulated and the experimental data is thus quantified as an increase of $\overline{RMSe}$ of 41.96 [dbar] and $\overline{Eff.}$ of 5.99 [p.p]. In order to verify that the PI-Lead controller is not deteriorating the performance of the internal pressure control, potentially undermining the argument of being an industrial-best-practice equivalent, the open loop control, defined in section 4.2.2, is evaluated experimentally. The results can be assessed in appendix D and display that the results for LSL0 are quite similar to both the simulated open loop performance and more importantly to the experimental results of the bHPU. The main discrepancy between the simulated and measured closed loop response is then deemed to be caused by the much less aggressive PI-Lead controller as compared to the simulated PID, yielding an increased efficiency at the cost of reduced pressure tracking performance.

Based on this, the benchmark HPU is deemed validated experimentally. The following control development will be carried out taking offset in the bHPU model, while the final control validation will be compared to the experimental bHPU results.

Control Development 5

In this chapter, controllers will be developed as to meet the problem definition, such that they allow the hydro gear to track a pressure reference, while increasing the system efficiency.

In the first section a single input, single output strategy is pursued, where a SMC-based controller tracks the pressure reference, while high efficiency figures are pursued by the means of a look-up table, defining the reference for the second input.

In the second section a multiple input, multiple output strategy is pursued, where SMC-based controllers are used for both pressure tracking and efficiency improvement.

The combination of intriguing performance figures and generality of the solution yields that the developed multiple input, multiple output approach is chosen for experimental validation in the third section, concluding the control development of this project.

5.1 Robust SISO Pressure Control With Max-Efficiency Based Look-up Table

In the following section various SISO-approaches will be developed for controlling the hydro gear. They will take offset in the concept of the variable frequency fixed displacement HPU, section 4.3, by controlling the output pressure through the input speed, as this proved to have high efficiency, though suffered from quite poor pressure tracking. Hence the SISO-approaches will seek to improve the pressure tracking while maintaining as much of the efficiency as possible. The controllers will be based on robust sliding mode control.

5.1.1 Control Strategy

Instead of applying a constant control input $u = 1$, it will be based on a look-up table, that describes the most efficient choice of u from the current value of ω_m as described by the steady state results. This general SISO pressure control strategy is illustrated in figure 5.1.

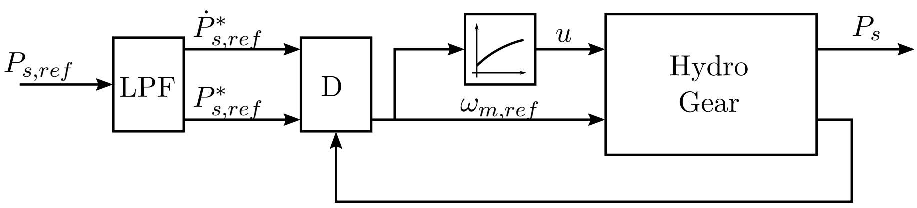

Figure 5.1: SISO control structure, with input low pass filter and max-efficiency based look-up table. The feed-back is unspecified as it may contain more signals than P_s.

As seen, the controller D will be developed to control the output pressure P_s through the input

$\omega_{m,ref}$, while the input u is a function of $\omega_{m,ref}$, under the assumption that its influence can be regarded as a disturbance to the pressure control. There will be implemented an input filter with the purpose of protecting the controller from infinite first order reference derivative in the hypothetical case of steps in the reference pressure. This also allows to evaluate the reference derivative without having to require this from the consumer load sensing.

The pressure control law will be developed with a continuous control that is aided by a sliding mode disturbance compensator.

A sliding mode algorithm is generally based on a notational simplification that substitute a nth order problem by a first order problem. By means of discontinuous control signals the algorithm can obtain *perfect* performance on the sliding mode, while obtaining robustness to matched parameter uncertainties and unmodeled dynamics. This is at the cost of extremely high control effort. In discrete systems this control effort may excite all resonance frequencies of which most may be uncontrollable due to having a finite update frequency. Furthermore, for most actuators, such discrete control signal is not admissible. Therefore, the sliding algorithm is usually modified to outputting admissible control activity, compromising the ideal performance and robustness [10].

The disturbance compensator will be designed for providing a continuous control signal while increasing robustness.

5.1.2 Choice of Control Input u from Steady State Results

In figure 5.2, the steady state solution is used to map the maximum obtainable efficiency as function of the shaft speed ω_m, along with the corresponding value of u. Since the most efficient values of u only varies across three of the discrete steps applied in the steady state solution, it is chosen to fit a second order polynomial function to the data.

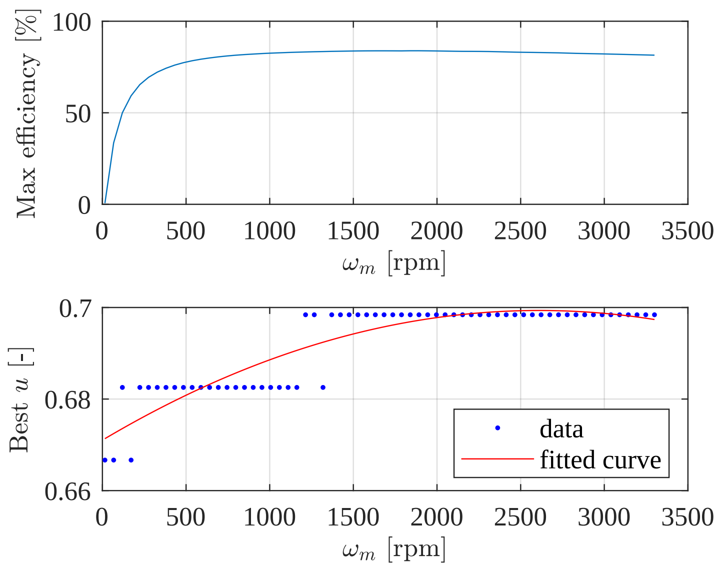

Figure 5.2: Uppermost is the maximum obtainable efficiencies as function of shaft speed in steady state. Lowermost is the values of u that contributed to the efficiency of the uppermost figure, labelled as "data", while a fitted second order polynomial is labelled as "fitted curve".

The second order polynomial function is described by equation 5.1.

$$f(\omega_m) = a_1\omega_m^2 + a_2\omega_m + a_3 \ , \qquad (5.1)$$
$$a_1 = -4.156 \cdot 10^{-9} \quad , \quad a_2 = 2.17 \cdot 10^{-5} \quad , \quad a_3 = 0.671$$

As seen, the variation of u is small. The maximum obtainable efficiency is generally high across all speeds. Furthermore, f belongs to the regions of $x = x_{max}$ according to the steady state results as $f(\omega_m) \in \{0.65, 1 \ |0 \leq \omega_m \leq 3300\}$ yielding that, at least during steady state, the pump effectively has a fixed displacement.

5.1.3 Reference Input Filter

As to protect the system from the hypothetical scenario of steps in the pressure reference and to be able to have its derivative, an input low pass filter is applied. The derivative is then available from the difference equation directly as seen in equation 5.2.

$$\dot{P}^*_{s,ref}(k) = -\frac{1}{\tau_f}P^*_{s,ref}(k-1) + \frac{1}{\tau_f}P_{s,ref}(k) \qquad (5.2a)$$

$$P^*_{s,ref}(k) = P^*_{s,ref}(k-1) + \dot{P}^*_{s,ref}(k)T_s \qquad (5.2b)$$

The consequence of this is indeed a reduced tracking performance as the controller only sees $P^*_{s,ref}$, while the performance quantification will be based on $P_{s,ref}$. Hence, in order to reduce the decay in tracking performance introduced by the filter, its time constant, τ_f should be reduced, while for improved protection against unrealisable inputs, τ_f should be increased.

5.1.4 Pressure Control Law

The output pressure control error is defined according to equation 5.3.

$$e_s = P_s - P^*_{s,ref} \qquad (5.3)$$

The pump leakage coefficient is found to be very small, hence it is assumed to be zero in terms of control development. This yields the pressure error dynamics of equation 5.5.

$$\begin{aligned} \dot{e}_s &= \dot{P}_s - \dot{P}^*_{s,ref} && (5.4) \\ &\approx \dot{P}_s|_{C_l=0} - \dot{P}^*_{s,ref} && (5.5) \\ &\approx \frac{\beta_s}{V_s}(D_s x K_{p\theta}\omega_m - Q_{sp} - K_{sc}\sqrt{P_s - P_c} - Q_{out}) - \dot{P}^*_{s,ref} \end{aligned}$$

Here, the flow Q_{sp} and the swash plate control piston displacement x is unknown. For the general case, the output flow Q_{out} can be measured by additional sensors or estimated by the consumer which is assumed to have load sensing, though it is desirable to avoid feedback of the load flow. The goal is to separate the error dynamics into terms that are directly controllable through the input and terms that are regarded as disturbances, such that $\dot{e}_s = g_s + f_s$. Here g_s is a function of the states x, P_s and the shaft speed ω_m, such that $g_s = g_s(x, P_s, \omega_m)$, and f_s is a function of the states, reference derivative, load reference signal and an unknown bound disturbance $|d_s| \leq D_s$, such that $f_s = f_s(\dot{P}^*_{s,ref}, P_s, P_c, P_p, z, l, d_s)$. These are defined in equation 5.6 and 5.7. The disturbance f_s is separated into two terms: A term that can be evaluated and compensated directly $f_{s1} = f_{s1}(\dot{P}^*_{s,ref}, P_s, P_c, l)$ and an unknown disturbance term $f_{s2} = f_{s2}(P_s, P_p, z, d_s)$.

$$g_s = S_\omega \omega_m \quad , \qquad S_\omega = \frac{D_s \beta_s x K_{p\theta}}{V_s} \tag{5.6}$$

$$f_s = f_{s1} + f_{s2} \quad , \tag{5.7}$$

$$f_{s1} = -\frac{\beta_s}{V_s}(K_{sc}\sqrt{P_s - P_c} + Q_{out}) - \dot{P}^*_{s,ref} \quad , \qquad f_{s2} = -\frac{\beta_s}{V_s} Q_{sp} + d_s$$

It is assumed that $\omega_m = \omega_{m,ref}$ yielding that the input $\omega_{m,ref}$ is stated directly in g_s. For S_ω it is assumed that $x = x_{max}$, while bulk modulus is assumed constant at a value of $\beta_s = 1.5 \cdot 10^9$ [Pa], as this yields that the now constant model $\hat{S}_\omega \geq S_\omega(x, P_s)$.

Hence a pressure control law can be established based on $\hat{g}_s$ and two control terms: A nominal controller and a compensation term, that will compensate for the disturbances of f_s and the inaccuracies of $\hat{g}_s$, thus allowing for the nominal control law to be fulfilled. This is defined in equation 5.8.

$$\hat{g}_s = U_{ns} + U_{cs} \tag{5.8}$$

From this, the induction motor reference speed can be isolated according to equation 5.9.

$$\omega_{m,ref} = \hat{S}_\omega^{-1} \left(U_{ns} + U_{cs} \right) \tag{5.9}$$

In the following sections the nominal and the compensating controllers will be designed.

5.1.5 Nominal Controller Design for the Pressure Control Law

It is desired to achieve first order linear time invariant (LTI) pressure dynamics as defined by equation 5.10.

$$\dot{e}_s = -C_s e_s \tag{5.10}$$

Assuming that any dynamics which do not comply with the first order LTI dynamics are ideally compensated by the compensating controller, this can be achieved by letting the nominal controller be formed according to equation 5.11.

$$U_{ns} = -C_s e_s \tag{5.11}$$

Tuning of the Nominal Controller

The influence of the gain C_s is studied through separation of variables and integration as defined by equation 5.10. The solution of the differential equation is found to be an exponential function according to equation 5.12.

$$e_s = -\frac{A}{C_s} exp(-C_s t) \tag{5.12}$$

Hence the time constant $\tau_s = \frac{1}{C_s}$ should be chosen to be 5-10 times slower than the input dynamics. As to quantify this requirement, the input dynamics through the induction motor and FOC-control are studied. Due to the relatively high complexity of an analytical solution, the dynamics are linearised and studied in the Laplace domain. In appendix C, the natural frequency is found to be 149 [rad/s], while the bandwidth is 408 [rad/s]. These figures are not conservatively estimated, thus should be used with caution. As to improve the pressure tracking performance C_s should be increased, though kept below $\frac{1}{5}$ to $\frac{1}{10}$ times the bandwidth of the FOC-controlled induction motor.

5.1.6 Compensating Controller Design for the Pressure Control Law

In the following section it is assumed that the model $\hat{g}_s$ is equal to the actual g_s, even though this is generally not possible. Then it is chosen to formulate the compensating controller according to equation 5.13 with ν_s describing the output of some sliding mode controller and a direct compensation of the known part of the disturbance. A low pass filter is applied to $\hat{f}_{s1}$, since it may act as an amplification of the measurement noise. This arises from the fraction $\frac{\beta_s}{V_s}$ being a very large number, while P_s and P_c are close to equal most of the time, leaving the term $\sqrt{P_s - P_c}$ to often contain more noise than intended signal. Similar behaviour is the case for Q_{out} as it is based on the same noise containing P_s-measurement. This yields, that only an estimate of f_{s1} is directly compensated, leaving the estimate-error to also be compensated by ν_s.

$$U_{cs} = \nu_s - \mathrm{LPF}(\hat{f}_{s1}) \tag{5.13}$$

For the purpose of the further control development it is assumed that $\mathrm{LPF}(\hat{f}_{s1}) = f_{s1}$. By doing this it is clear that ν_s need to compensate f_{s2}, according to equation 5.14.

$$\begin{aligned} \dot{e}_s =& g_s \hat{g}_s^{-1}(U_{ns} + U_{cs}) + f_s \\ =& - C_s e_s + \nu_s + f_{s2} \end{aligned} \tag{5.14}$$

Hence, the sliding mode algorithm will be designed to realize $\nu_s = -f_{s2}$. Then first order dynamics is achieved for the pressure control law.

In the following sections a signum function will be used, that is defined according to equation 5.15.

$$\mathrm{sgn}(x) = \begin{cases} 1 & \text{for } x > 0 \\ -1 & \text{for } x < 0 \end{cases} \quad , \quad \mathrm{sgn}(0) \in [-1,\ 1] \tag{5.15}$$

1SMDO

In this section, the so-called first sliding mode disturbance observer (1SMDO) will be utilized. A sliding variable and its first order derivative is defined in equation 5.16.

$$\sigma_s = e_s - z \quad , \quad \dot{\sigma_s} = \dot{e}_s - \dot{z} \tag{5.16}$$

Then choosing $\dot{z}$ to be defined according to equation 5.17, yields the sliding mode first order time derivative according to 5.18.

$$\dot{z} = U_{ns} + U_{cs} + \rho_s \,\mathrm{sgn}(\sigma_s) + f_{s1} \tag{5.17}$$

$$\begin{aligned} \dot{\sigma_s} &= U_{ns} + U_{cs} + f_s - (U_{ns} + U_{cs} + \rho_s \,\mathrm{sgn}(\sigma_s) + f_{s1}) \\ &= f_{s2} - \rho_s \,\mathrm{sgn}(\sigma_s) \end{aligned} \tag{5.18}$$

A positive definite radially unbounded Lyapunov candidate function $V(\sigma_s)$ is proposed along with defining its first order derivative in equation 5.19.

$$V(\sigma_s) = \frac{1}{2}\sigma_s^2 \quad , \quad \dot{V}(\sigma_s) = \sigma_s \left(f_{s2} - \rho_s \,\mathrm{sgn}(\sigma_s)\right) \tag{5.19}$$

The open loop disturbance is bounded by $|f_{s2}| \leq L_s$, according to equation 5.20 with the arguments of the following enumerated points.

$$|f_{s2}| = \left| -\frac{\beta_s}{V_s} Q_{sp} + d_s \right| \leq \underbrace{\frac{\beta_s}{V_s}\bar{Q}_{sp}}_{(1)} + \underbrace{D_s}_{(2)} = L_s \tag{5.20}$$

(1) The fraction is matched as β_s can be evaluated online. In order to develop the upper bound $\bar{Q}_{sp}$, it is assumed that $P_s \geq P_p$. This is with few minor exceptions generally the case. Based on that, the upper bound is found by setting $P_p = 0$, such that $Q_{sp} = K_{sp}z\sqrt{|P_s - P_p|} \cdot sgn(P_s - P_p) \leq K_{sp}z\sqrt{P_s} = \bar{Q}_{sp}$, while z can be evaluated with available measurement points.
(2) As previously specified, the unknown disturbance needs to be upper bounded according to $|d_s| \leq D_s$.

This yields that the derivative Lyapunov candidate function is dominated according to equation 5.21.

$$\dot{V}(\sigma_s) = \sigma_s(f_{s2} - \rho_s \operatorname{sgn}(\sigma_s)) \leq |\sigma_s|L_s - \rho_s\sigma_s \operatorname{sgn}(\sigma_s) \tag{5.21}$$

Since the function $\dot{V} = -\alpha V^{\frac{1}{2}}$ can be shown to be negative definite whenever V is positive definite, it is chosen to use this function to define ρ_s according to equation 5.22.

$$|\sigma_s|L_s - \rho_s\sigma_s \operatorname{sgn}(\sigma_s) = -\alpha\left(\frac{1}{2}\sigma_s^2\right)^{\frac{1}{2}} = -\frac{\alpha}{\sqrt{2}}|\sigma_s| \quad \rightarrow \quad \rho_s = \frac{\alpha}{\sqrt{2}} + L_s \tag{5.22}$$

In order to account for the case that $g_s \neq \hat{g}_s$, which was assumed until this point, the compensation factor is defined $K_m \leq \frac{g_s}{\hat{g}_s}$ yielding the final $\rho_s = \frac{1}{K_m}(\frac{\alpha}{\sqrt{2}} + L_s)$. Hence, applying this controller, the sliding mode equilibrium point $\sigma_s = 0$ is globally asymptotically stable. Furthermore, from $\dot{V}$ using separation of variables and integration, a reaching time of $t_r = \frac{2(V(\sigma_s(0)))^{1/2}}{\alpha}$ is derived, yielding that the sliding mode equilibrium point is globally finite time stable [12].

When $\forall t > t_r$, $\sigma_s = 0$ then $\forall t > t_r$, $\dot{\sigma}_s = 0$, yielding that $f_{s2} = \rho_s \text{sgn}(\sigma_s)$ meaning that the average value of $\rho_s \text{sgn}(\sigma_s)$ equals f_{s2}. Then the compensating controller can be described by equation 5.23 as this will yield an approximation of f_{s2}.

$$\nu_s = -\rho_s \text{LPF}(\text{sgn}(\sigma_s)) \tag{5.23}$$

Here, the function LPF is comprised of four first order low pass filters. Indeed, the choice of filter frequency heavily influence the control performance. If the frequency is too high, it does not attenuate the high frequencies originating from the discontinuous signum function, while if it is too low, the filter introduce a phase lag so large that the compensating controller is not able to compensate the disturbances.

In figure 5.3, the pressure tracking of the 1SMDO controller applied on the trajectory of LSL3 and LL3, is depicted.

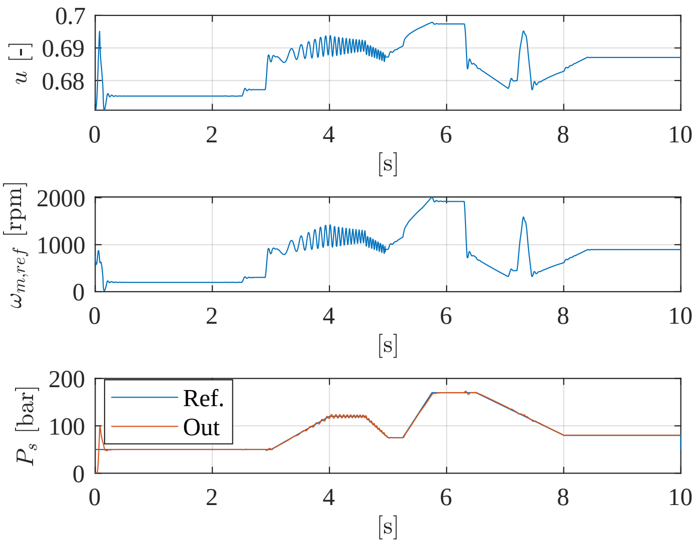

Figure 5.3: Simulation of 1SMDO-controller running the trajectory of LSL3 and LL3.

As seen, this yields a much improved pressure tracking compared to the bHPU. Running it for all combinations of LSL and LL yields the performance figures of table 5.1.

Table 5.1: Simulated performance figures across all combinations of LSL and LL with comparison to the bHPU stated as $^{bHPU}/_{1SMDO}$.

(a) System efficiency [%].

Load Level (LL)	Load Sense Level (LSL) 0	1	2	3
0	35.6/57.5	30.6/62.5	26.3/64.6	22.4/63.9
1	48.5/69.3	43.1/72.9	38.3/73.9	33.7/73.3
2	56.8/73.3	51.6/75.6	46.7/76.2	42/75.6
3	62.5/74.7	57.6/76.2	53/76.2	48.2/75.5

(b) RMS pressure tracking error [dbar].

Load Level (LL)	Load Sense Level (LSL) 0	1	2	3
0	0/0	0.8/4.3	1.8/6.1	5.6/7.6
1	1.4/3.6	1.7/5.5	2.5/6.9	5.8/8.3
2	16.7/6.7	6.8/7.6	6.3/8.7	8.2/9.9
3	52.3/15.8	26.5/11	17.3/11	16/11.8

Based on this, the average performance figures and the improvement compared to the bHPU are given in equation 5.24 and 5.25.

$$\overline{RMSe} = 7.8[\text{dbar}] \qquad \downarrow 2.82[\text{dbar}] \tag{5.24}$$

$$\overline{Eff.} = 71.32[\%] \qquad \uparrow 27.78[p.p.] \tag{5.25}$$

While the 1SMDO displays good performance figures, it is a disadvantage that the performance is crucially dependent on the choice of filter frequency. In the following section, a method that may solve this issue is proposed.

2SMDO

In this section, a second order sliding mode will be implemented for disturbance observation based on the so-called super twisting algorithm. This features finite time convergence on the sliding variable and its derivative, while the discontinuous signum function is nested within an integral.

Reusing the sliding variable of the 1SMDO, restated in equation 5.26, while $\dot{z}$ is defined according to equation 5.27, yields the first order derivative of the sliding variable according to equation 5.28.

$$\sigma_s = e_s - z \tag{5.26}$$

$$\dot{z} = U_{ns} + U_{cs} + \nu_s + f_{s1} \tag{5.27}$$

$$\begin{aligned} \dot{\sigma_s} &= U_{ns} + U_{cs} + f_s - (U_{ns} + U_{cs} + \nu_s + f_{s1}) \\ &= f_{s2} - \nu_s \end{aligned} \tag{5.28}$$

Then the compensating controller is defined according to equation 5.29 [11].

$$\nu_s = k_1\sqrt{|\sigma_s|}\mathrm{sgn}(\sigma_s) + w \quad , \qquad \dot{w} = k_2\mathrm{sgn}(\sigma_s) \tag{5.29}$$

This yields the sliding dynamics of equation 5.30.

$$\dot{\sigma}_s = f_{s2} - k_1\sqrt{|\sigma_s|}\mathrm{sgn}(\sigma_s) - w \tag{5.30}$$

Assuming that $|\dot{f}_{s2}| \leq \bar{L}_s$, the sliding dynamics can be rearranged into equation 5.31.

$$\begin{aligned} \dot{\sigma}_s &= \gamma - k_1\sqrt{|\sigma_s|}\mathrm{sgn}(\sigma_s) \quad , \\ \dot{\gamma} &= \dot{f}_{s2} - \dot{w} \\ &= \dot{f}_{s2} - k_2\,\mathrm{sgn}(\sigma_s) \leq \bar{L}_s - k_2\mathrm{sgn}(\sigma_s) \end{aligned} \tag{5.31}$$

For the super twisting algorithm, the stability analysis is elaborate and beyond the scope of this project. According to [11] a suitable tuning is obtained by setting $k_1 = 1.5\sqrt{\bar{L}_s}$ and $k_2 = 1.1\bar{L}_s$, while $\bar{L}_s$ is set constant as its evaluation is elaborate. In figure 5.4, the pressure tracking of the 2SMDO controller applied on the trajectory of LSL3 and LL3, is depicted.

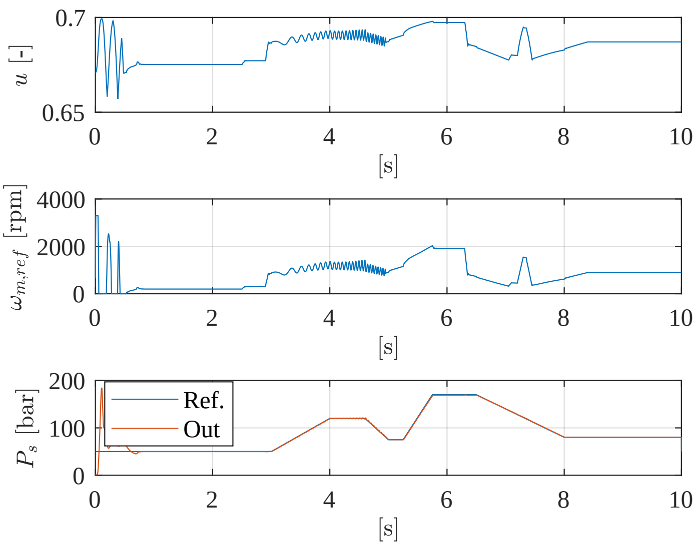

Figure 5.4: Simulation of 2SMDO-controller running the trajectory of LSL3 and LL3.

As seen, the pressure tracking seems slightly improved compared to the 1SMDO. Running it for all combinations of LSL and LL yields the performance figures of table 5.2.

Table 5.2: Simulated performance figures across all combinations of LSL and LL with comparison to the bHPU, stated as ${}^{bHPU}/_{2SMDO}$.

(a) System efficiency [%].

Load Level (LL)	Load Sense Level (LSL) 0	1	2	3
0	35.6/57.8	30.6/62.7	26.3/64.7	22.4/64
1	48.5/69.4	43.1/73	38.3/74	33.7/73.4
2	56.8/73	51.6/75.3	46.7/75.9	42/75.4
3	62.5/73.6	57.6/74.9	53/75.1	48.2/74.6

(b) RMS pressure tracking error [dbar].

Load Level (LL)	Load Sense Level (LSL) 0	1	2	3
0	0/9.9	0.8/5.2	1.8/5	5.6/6
1	1.4/9.8	1.7/5.1	2.5/4.9	5.8/6
2	16.7/9.9	6.8/5.3	6.3/5.1	8.2/6.1
3	52.3/14.1	26.5/7.5	17.3/5.5	16/6.3

Based on this, the average performance figures and the improvement compared to the bHPU are given in equation 5.32 and 5.33.

$$\overline{RMSe} = 6.97[\text{dbar}] \qquad \downarrow 3.65[\text{dbar}] \tag{5.32}$$

$$\overline{Eff.} = 71.04[\%] \qquad \uparrow 27.49[p.p.] \tag{5.33}$$

As seen, the performance figures are almost equal to the 1SMDO, displaying a slight improvement of pressure tracking and a slight deterioration of the efficiency.

The performance figures of the 2SMDO applied in a SISO-structure seems very intriguing, though the look-up table can at best only be considered true for the project test bench and at worst only be considered true for the model. Therefore, it is decided to continue the control-development investigating MIMO-control in the following section.

5.2 Robust MIMO Control

In this section a robust MIMO control will be developed with the goal of reaching comparable performance figures as of the robust SISO control, though without being dependent on the precision of a model based look-up table.

5.2.1 Control Strategy

The strategy is to consider the hydro gear as a multiple input, multiple output system, applying the pressure control law developed in the previous section (equation 5.9) with the 2SMDO and to develop a power loss control law, that seeks to minimize the power loss through u. This strategy is illustrated in figure 5.5.

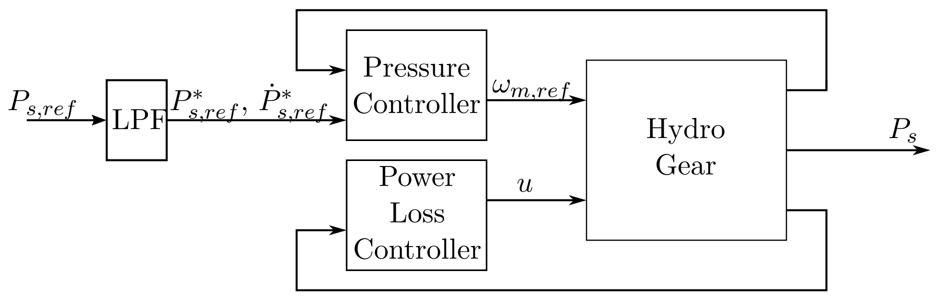

Figure 5.5: MIMO control structure with pressure reference input filter. The feedback signals from the hydro gear to the controllers are unspecified as they may contain several states.

The power loss control law will be formed with a nominal and a compensating controller like for the pressure control law. As will be highlighted, the formulation of an exact control goal on which ideal control could potentially be applied is not feasible for the power loss control law. Rather it takes the form of a minimization problem which is enforced by introducing a boundary layer.

5.2.2 Power Loss Control Law

The control goal is to minimize the difference between the electrical input power and the hydraulic output power. This difference is indeed equal to the combined system losses, described by equation 5.34.

$$
\begin{aligned}
e_w =& \mathcal{P}_{IM,in} - \mathcal{P}_{out} && (5.34a)\\
=& \mathcal{P}_{IM,loss} + \mathcal{P}_{hyd,loss} && (5.34b)
\end{aligned}
$$

These losses are described by nine loss terms as defined in the loss model, section 1.3.3. By identifying the main contributors to the system losses, a highly simplified power loss term is stated in equation 5.35, containing only these main contributors.

$$
\begin{aligned}
e_w \approx& \mathcal{P}_{ts}|_{C_l=0} + \mathcal{P}_{sc} + \mathcal{P}_{ct} + \mathcal{P}_{loss,q} \qquad (5.35)\\
\approx& B_\omega {\omega_m}^2 + K_{sc}\left(P_s - P_c\right)^{3/2} + K_{ct}\left(\frac{\left(P_c - P_t\right)A_{cy} + F_{cy0} - K_u u}{K_{cy}} + y_{max}\right)\left(P_c - P_t\right)^{3/2} \ldots\\
&+ \left(R_r + R_s\right){I_{sq}}^2
\end{aligned}
$$

Then the loss dynamics are approximated by equation 5.36.

$$
\begin{aligned}
\dot{e}_w \approx& 2B_\omega \omega_m \dot{\omega}_m + \frac{3}{2}K_{sc}\sqrt{P_s - P_c}\left(\dot{P}_s - \dot{P}_c\right) + \frac{K_{ct}\left(\dot{P}_c A_{cy} - K_u \dot{u}\right)\left(P_c - P_t\right)^{3/2}}{K_{cy}} \ldots \qquad (5.36)\\
&+ \frac{3}{2}K_{ct}\left(\frac{\left(P_c - P_t\right)A_{cy} + F_{cy0} - K_u u}{K_{cy}} + y_{max}\right)\sqrt{P_c - P_t}\dot{P}_c + 2\left(R_r + R_s\right)I_{sq}\dot{I}_{sq}
\end{aligned}
$$

This power loss dynamics can be expanded into 58 terms by substitution of the dynamic equations for $\dot{\omega}_m$, $\dot{I}_{sq}$, $\dot{P}_s$ and $\dot{P}_c$. From these terms 17 explicitly depend on the inputs u and $\omega_{m,ref}$, recalling the assumption that $\omega_m = \omega_{m,ref}$. 11 of the terms have diminishing influence on the power loss error dynamics, but greatly increase the algebraic complexity and are therefore regarded as disturbances. As for the pressure control law, the goal is to separate the error dynamics into terms, that are directly controllable through the inputs and terms that are regarded as disturbances, such that $\dot{e}_w = g_w + f_w$. Here g_w is a function of u, ω_m, P_s, P_c, I_{sd} and I_{sq}, such that $g_w = g_w(u, \omega_m, P_s, P_c, I_{sd}, I_{sq})$. Likewise, f_w is a function of all states, for now denoted by the state vector χ and an unknown bound disturbance $|d_w| \leq D_w$, such that $f_w = f_w(\chi, d_w)$. The main contributors to the input scaling of the power loss dynamics can then be expressed by equation 5.37.

$$
\begin{aligned}
g_w =& W_u u + W_{\omega 1}\omega_m - W_{\omega 2}\omega_m^2 \qquad (5.37)\\
W_u =& 3\frac{\beta_c}{V_c}\frac{K_u K_{ct}\left(-K_{sc}\sqrt{P_s - P_c}\sqrt{P_c - P_t} + y_{max}K_{ct}\left(P_c - P_t\right)\right)}{K_{cy}}\\
W_{\omega 1} =& 2\frac{I_{sd}I_{sq}L_r L_s p_b\left(R_s + R_r\right)}{{L_m}^2 - L_r L_s}\\
W_{\omega 2} =& 2\frac{B_\omega^2}{J}
\end{aligned}
$$

As seen, W_u relates to the main hydraulic losses which is the loss through the electrically actuated pressure relief valve of the control unit, $W_{\omega 1}$ relates to the main electrical power losses in the induction machine and $W_{\omega 2}$ relates to frictional losses in the rotary group. The remaining loss terms are left for the disturbance and system dynamics, f_w, as stated in equation 5.38. The part of f_w that can be evaluated online is denoted f_{w1} while the unknown/disregarded is denoted f_{w2}.

$$\begin{aligned} f_w =& f_{w1} + f_{w2} \quad , \\ f_{w1} =& 2\frac{\left(\left(R_r + R_s\right) L_r + L_s R_r\right) {I_{sq}}^2 R_s}{{L_m}^2 - L_r L_s} + 3\frac{K_{sc}\beta_s \left(-\sqrt{P_s - P_c} Q_{out} + K_{sc}\left(-P_s + P_c\right)\right)}{2V_s} \quad ... \\ & - 3/2\frac{{K_{ct}}^2 \beta_c {y_{max}}^2 P_c}{V_c} \quad , \\ f_{w2} =& -3\frac{K_{sc}\beta_s Q_{sp}\sqrt{P_s - P_c}}{2V_s} + 2\frac{I_{sq} L_m \left(R_r + R_s\right)\left(I_{rd} L_r p_b \omega_m - I_{rq} R_r\right)}{{L_m}^2 - L_r L_s} + ...44 \text{ terms}... + d_w \end{aligned} \tag{5.38}$$

A power loss control law can be established, based on g_w, a nominal and a compensating controller according to equation 5.39.

$$g_w = U_{nw} + U_{cw} \tag{5.39}$$

In the previous section the inverse of the input scaling for the pressure dynamics was developed and is restated in equation 5.40. Likewise is done for the input scaling of the power loss dynamics yielding the control signal of equation 5.41.

$$\omega_{m,ref} = S_\omega^{-1}\left(U_{ns} + U_{cs}\right) \tag{5.40}$$

$$u_{ref} = W_u^{-1}\left(U_{nw} + U_{cw} - W_{\omega 1} S_\omega^{-1}\left(U_{ns} + U_{cs}\right) + W_{\omega 2}\left(S_\omega^{-1}\left(U_{ns} + U_{cs}\right)\right)^2\right) \tag{5.41}$$

Based on this, the following sections will develop the nominal and the compensating control terms as to minimize the power loss.

5.2.3 Nominal Controller Design

For the power loss control law it is not possible to obtain first order LTI-dynamics for e_w regardless of the choice of compensator as there is only one point of zero power loss, that is when the hydro gear is turned off (zero input power).

One could choose to define a continuous lower bound of e_w and name it $\underline{e_w}$. Then this could form a coordinate transformation by $\tilde{e}_w = e_w - \underline{e_w}$ for which LTI-dynamics are obtainable and then formulate a nominal control law according to equation 5.42.

$$\dot{e}_w = -C_w \tilde{e}_w \quad |\dot{\tilde{e}}_w \approx \dot{e}_w \tag{5.42}$$

This solution is though not feasible as forming a continuous lower bound for e_w will depend on all states and any sustained imprecisions of the power losses may cause the ideally compensating controller to diverge. Further, the solution will yield a great loss of generality as $\underline{e_w}$ is unique for the hydro gear in concern.

Instead, the nominal control law is designed as if first order LTI-dynamics were obtainable on e_w, according to equation 5.43. This will simply minimize e_w.

$$\dot{e}_w = -C_w e_w \tag{5.43}$$

Hence, the nominal controller of equation 5.44 can be formed.

$$U_{nw} = -C_w e_w \tag{5.44}$$

Tuning of the Nominal Controller

Reusing the notation of the minimum e_w being $\underline{e_w}$, the effective nominal control law will be approximated by equation 5.45.

$$\dot{e}_w \approx C_w\underline{e_w} - C_w e_w \tag{5.45}$$

The analytical solution to this is stated in equation 5.46.

$$e_w = \underline{e_w} - \frac{A}{C_w}exp(-C_w t) \quad , \quad A = \text{sgn}(\underline{e_w} - e_w)exp(-C_w k_0) \tag{5.46}$$

Hence, C_w is the speed of which e_w will tend to $\underline{e_w}$ under the assumption that all other dynamics are ideally compensated by the compensating controller. For faster reduction of the power losses, C_w should be increased, though it should be kept well below C_s as to allow for the pressure control law to converge the fastest and avoid the two control laws to counter each other.

5.2.4 Compensating Controller Design for the Power Loss Law

Like for the nominal control design, the compensating control design takes offset in minimizing e_w rather than reaching zero. Therefore, the compensating controller should not ideally compensate f, like for the pressure control. Instead, it should compensate all dynamics and non-linearities not described by equation 5.45. As the minimal loss level $\underline{e_w}$ is unknown during runtime, it would seem intuitive to only apply a sliding mode compensating controller as $U_{cw} = v_w$, though from experience it is found that compensating with the known term f_{w1} according to equation 5.47 improves the performance of the developed sliding mode compensator.

$$U_{cw} = v_w - f_{w1} \tag{5.47}$$

In the following section it is assumed that $\hat{g}_w = g_w$, even though this is generally not possible. This is also underlined by the fact that $\hat{g}_w$ is based on simplifications of the model. In order to obtain a compensating control structure, that drives the losses down without trying to enforce ideal compensation a first sliding mode disturbance observer will be developed with a boundary layer.

1SMDO with boundary layer

In this section a first sliding mode disturbance observer (1SMDO) is developed and a boundary layer is added in order to compromise the ideal robustness and allow the controller to only minimize the control objective rather than obtain ideal tracking. A sliding variable is defined in equation 5.48. Then choosing $\dot{z}$ to be defined according to equation 5.49, yields the first order derivative of the sliding variable according to equation 5.50.

$$\sigma_w = e_w - z \tag{5.48}$$

$$\dot{z} = U_{nw} + U_{cw} + v_w + f_{w1} \tag{5.49}$$

$$\begin{aligned} \dot{\sigma}_w &= U_{nw} + U_{cw} + f_w - (U_{nw} + U_{cw} + v_w + f_{w1}) \\ &= f_{w2} - v_w \end{aligned} \tag{5.50}$$

A positive definite radially unbounded Lyapunov candidate function $V(\sigma_w)$ is proposed along with defining its first order derivative in equation 5.51.

$$V(\sigma_w) = \frac{1}{2}\sigma_w^2 \quad , \quad \dot{V}(\sigma_w) = \sigma_w\left(f_{w2} - v_w\right) \tag{5.51}$$

The open loop disturbance is bounded by $|f_{w2}| \leq L_w$, following the same procedure as for f_{s2}, being to create the function L_w based on f_{w2}, with online evaluation of all possible terms and simplifications of the remaining, that are guaranteed to make L_w dominate f_{w2}. The bound is evaluated according to equation 5.52 with the arguments of the following enumerated points.

$$\begin{aligned} |f_{w2}| = &\left| -3\frac{K_{sc}\beta_s Q_{sp}\sqrt{P_s - P_c}}{2V_s} + 2\frac{I_{sq}L_m\left(R_r + R_s\right)\left(I_{rd}L_r p_b \omega_m - I_{rq}R_r\right)}{{L_m}^2 - L_r L_s} + \text{...44 terms...} + d_w \right| \\ &\leq \underbrace{3\frac{K_{sc}\beta_s \bar{Q}_{sp}\sqrt{P_s - P_c}}{2V_s}}_{(1)} + \underbrace{2\frac{I_{sq}L_m\left(R_r + R_s\right)\bar{I}_{rq}R_r}{{L_m}^2 - L_r L_s}}_{(2)} + \underbrace{\text{...44 terms...}}_{(3)} + \underbrace{D_w}_{(4)} = L_w \end{aligned} \tag{5.52}$$

(1) All terms except Q_{sp} can be evaluated directly, thus the previously developed $\bar{Q}_{sp}$ is used. Note that terms like $\sqrt{P_s - P_c}$ are evaluated applying the form $\sqrt{|P_s - P_c|} \cdot sgn(P_s - P_c)$, though the notation is omitted for compactness of the equations.
(2) The rotor currents I_{rd} and I_{rq} are unknown, though by orienting the dq frame such that the d-axis align with Ψ_s, yields that $I_{rd} = 0$. The phase voltage is bounded, yielding a bounded phase current, yielding a bounded stator flux. This is not directly visible in the developed model, as the voltage source inverter is omitted. Then the rotor e.m.f. is a function of the bounded stator flux and the slip speed, yielding that the bound of $|I_{rq}| \leq \bar{I}_{rq}$ can be evaluated as a function of the slip speed.
(3) Similar methodology is applied to the remaining terms.
(4) As previously specified, the unknown disturbance needs to be upper bounded according to $|d_w| \leq D_w$.

This yields that the derivative Lyapunov candidate function is dominated according to equation 5.53.

$$\dot{V}(\sigma_w) = \sigma_w(f_{w2} - v_w) \leq |\sigma_w|L_w - \sigma_w v_w \tag{5.53}$$

Since the function $\dot{V}_1 = -\alpha V^{\frac{1}{2}}$ can be shown to be negative definite whenever V is positive definite, it is chosen to let $\dot{V}_1$ dominate $\dot{V}$ by equation 5.54.

$$|\sigma_w|L_w - \sigma_w v_w = -\frac{\alpha}{\sqrt{2}}|\sigma_s| \tag{5.54}$$

A boundary layer is added through approximating the signum function by the sigmoid function and thus choosing the compensating controller according to equation 5.55.

$$v_w = \rho_w \frac{\sigma_w}{|\sigma_w| + \epsilon} \quad , \quad \epsilon = \frac{\varphi}{100} \tag{5.55}$$

This yields that ρ_w can be defined according to equation 5.56.

$$|\sigma_w|L_w - \sigma_w \rho_w \frac{\sigma_w}{|\sigma_w| + \epsilon} = -\frac{\alpha}{\sqrt{2}}|\sigma_w| \quad \rightarrow \quad \rho_w = \frac{\alpha}{\sqrt{2}} + L_w + \epsilon \frac{\frac{\alpha}{\sqrt{2}}|\sigma_w| + L_w|\sigma_w|}{\sigma_w^2} \tag{5.56}$$

As seen, the size of ρ_w is highly dominated by the terms $\frac{\alpha}{\sqrt{2}} + L_w$, though the choice of φ should be taken into account. Disregarding the last term such that $\rho_w = \frac{\alpha}{\sqrt{2}} + L_w$ it can be shown that convergence is guaranteed to a domain satisfying $|\sigma_w| \leq \varphi$ [12]. In order to account for the case that $g_w \neq \hat{g}_w$, which was assumed until this point, the compensation factor is defined $K_m \leq \frac{g_w}{\hat{g}_w}$ yielding the final $\rho_w = \frac{1}{K_m}(\frac{\alpha}{\sqrt{2}} + L_w)$.

For implementation of the power loss control law, the high algebraic complexity of evaluating L_w online, renders it necessary to set ρ_w constant, though compromising the robustness.

The boundary layer width φ is then used as a measure of the maximum deviation that σ_w is bound to have from zero.

As to aid the understanding of this concept and to give an estimation of the size, it is noted that the disturbance f_w in steady state will correspond to the steady state power loss. Hence, disregarding the 'pre-compensation' of f_{w1}, the boundary layer width should approximately correspond to the minimum power loss. In figure 5.6 the minimum steady state power loss is depicted as function of shaft speed and output power.

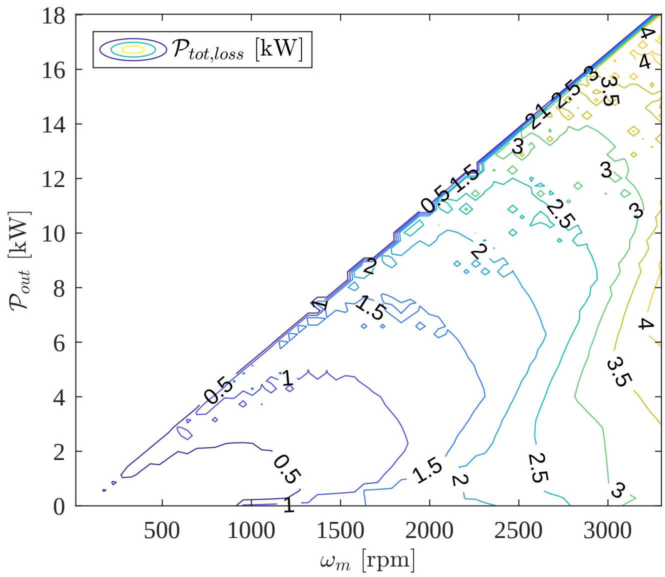

Figure 5.6: The minimum steady state power loss as function of shaft speed and output power.

Based on this, an initial guess for the boundary layer width is $\varphi = 4000$.

In figure 5.7, the pressure tracking of the developed MIMO control structure applied on the trajectory of LSL3 and LL3, is depicted.

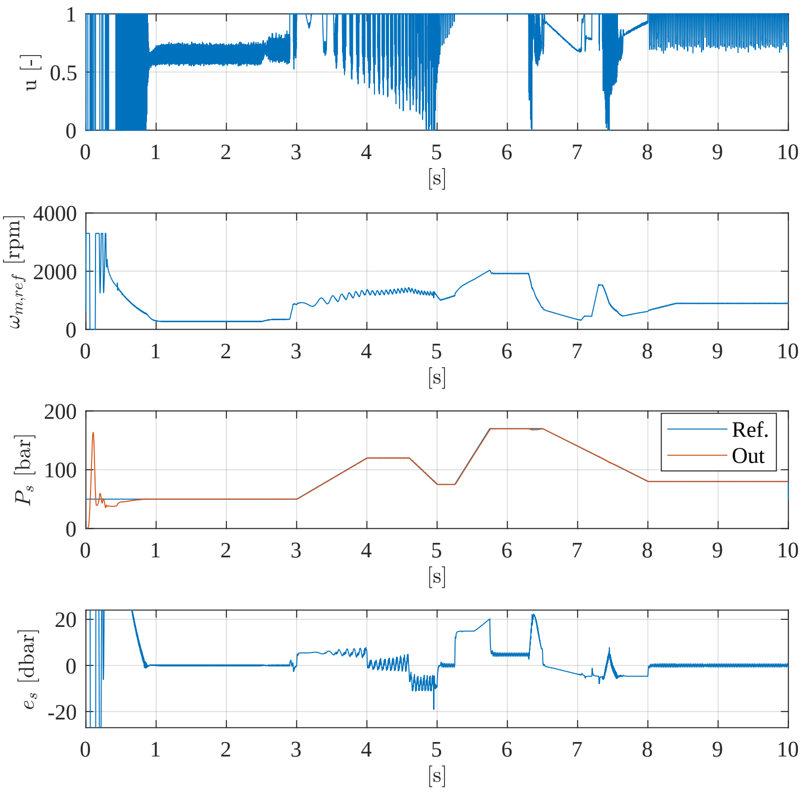

Figure 5.7: Simulation of the developed MIMO control, running the trajectory of LSL3 and LL3.

This controller displays highly intriguing performance figures with an efficiency of 74.7 [%] and RMSe of 5.83 [dbar] for the trajectory, though the very noisy control signal u is not admissible for the control unit. It should be noted, that the noise primarily stems from $W_{\omega 1}$ as this is a function of the quadrature current I_{sq}. Therefore, a low pass filter is applied to the signal, according to equation 5.57.

$$u_{ref} = \text{LPF}\left(W_u^{-1}\left(U_{nw} + U_{cw} - W_{\omega 1} S_\omega^{-1}\left(U_{ns} + U_{cs}\right) + W_{\omega 2}\left(S_\omega^{-1}\left(U_{ns} + U_{cs}\right)\right)^2\right)\right) \tag{5.57}$$

The consequence of applying this filter is a further compromise of the robustness and a deterioration of the linearity of the nominal control. But, the model neglects the dynamics of the valve spool, which allows the spool to follow the signal instantaneously. In the test bench, the spool would act as a filter to the signal, nonetheless.

In figure 5.8, the pressure tracking of the developed MIMO control structure with low pass filter on u, applied on the trajectory of LSL3 and LL3, is depicted.

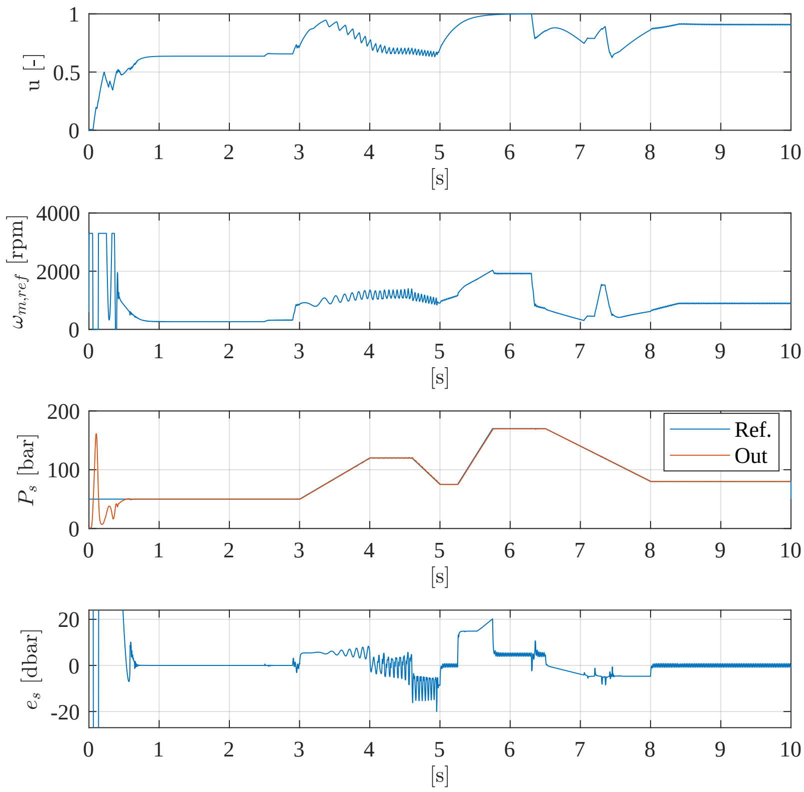

Figure 5.8: Simulation of the developed MIMO control with low pass filter on u, running the trajectory of LSL3 and LL3.

As seen, the pressure tracking is still good, while the control signals are smooth. Running it for all combinations of LSL and LL yields the performance figures of table 5.3.

Table 5.3: Simulated performance figures across all combinations of LSL and LL with comparison to the bHPU, stated as ${}^{bHPU}/_{MIMO}$.

(a) System efficiency [%].

Load Level (LL)	Load Sense Level (LSL) 0	1	2	3
0	35.6/60.1	30.6/64.2	26.3/65	22.4/62.2
1	48.5/69.9	43.1/73	38.3/73.8	33.7/73
2	56.8/73.3	51.6/75.4	46.7/75.9	42/75.3
3	62.5/73.6	57.6/75	53/75.5	48.2/75.2

(b) RMS pressure tracking error [dbar].

Load Level (LL)	Load Sense Level (LSL) 0	1	2	3
0	0/4.5	0.8/2.8	1.8/3.6	5.6/5.1
1	1.4/4.5	1.7/2.8	2.5/3.7	5.8/5.1
2	16.7/4.6	6.8/3	6.3/3.8	8.2/5.1
3	52.3/11	26.5/5	17.3/4	16/5.2

Based on this, the average performance figures and the improvement compared to the bHPU are given in equation 5.58 and 5.59.

$$\overline{RMSe} = 4.61[\text{dbar}] \qquad \downarrow 6[\text{dbar}] \tag{5.58}$$

$$\overline{Eff.} = 71.27[\%] \qquad \uparrow 27.73[p.p.] \tag{5.59}$$

As seen, this is a great improvement in terms of both tracking error and efficiency compared to the benchmark HPU, even a slight improvement to the SISO approach. From this it may be deduced, that the overall most efficient choice of u as function of ω_m in steady state may not be the most efficient choice of u when considering transients and variations in load.

5.3 Experimental Validation of the MIMO Control Structure

During implementation of the developed MIMO control structure many of the same characteristics were experienced as for the bHPU. The noise on the pressure measurement rendered it necessary to reduce the gains of the nominal controllers, C_s and C_w. Further it was experienced that the control structure induced small oscillations during the regions of constant load. The resulting reference tracking for the trajectory LSL3 and LL3 is depicted in figure 5.9, while the remaining 15 can be assessed in appendix F.

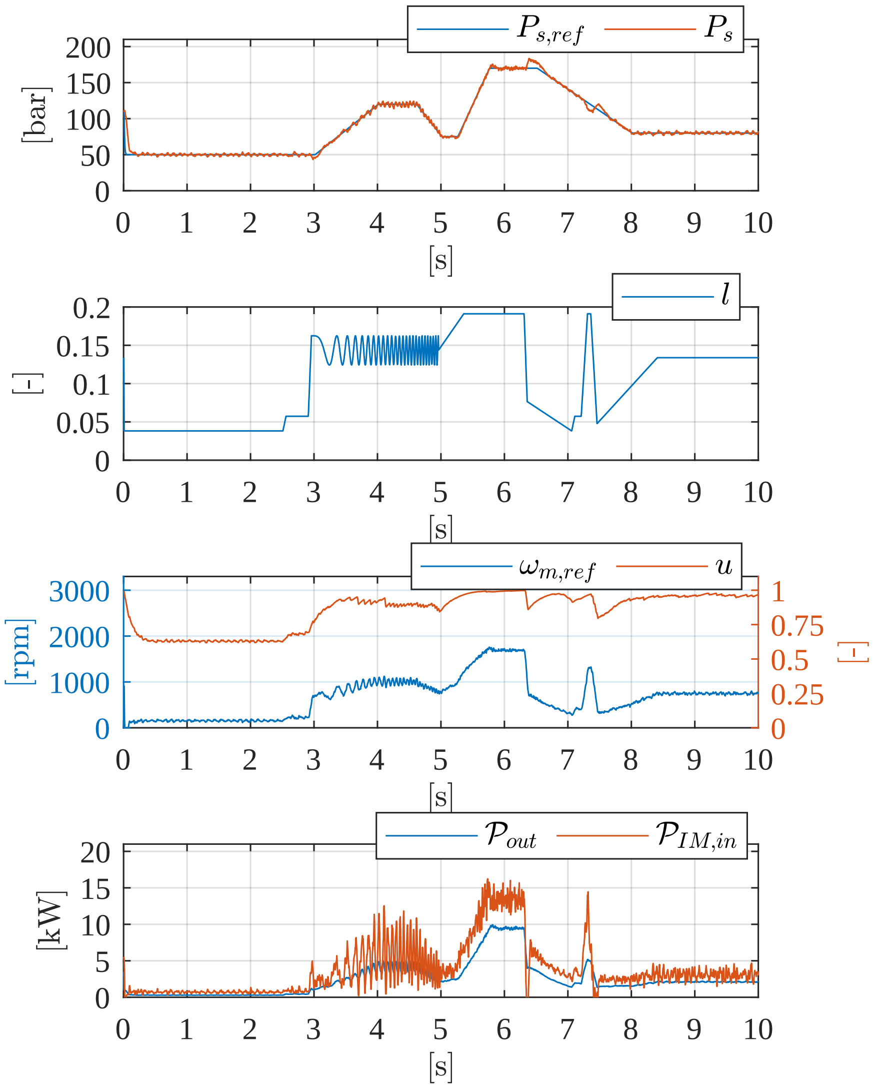

Figure 5.9: Experimental validation of the developed MIMO control, running the trajectory of LSL3 and LL3.

As seen, the pressure tracking is similar to the simulated, though deteriorated due to the reduction of control gains. Furthermore, the input power is rather noisy, which is deemed to originate in the small oscillations seen in the input signals $\omega_{m,ref}$ and u. Running the hydro gear test bench for all combinations of LSL and LL yields the performance figures of table 5.4.

Table 5.4: Experimentally attained performance figures across all combinations of LSL and LL with comparison to the bHPU, stated as ${}^{bHPU}/_{MIMO}$.

(a) System efficiency [%].

Load Level (LL)	Load Sense Level (LSL) 0	1	2	3
0	38.6/50.5	35.9/51	32.5/52.1	28.5/50.8
1	52.7/60.6	50.2/60.7	46.4/61.9	41.7/62.4
2	60.2/64.1	58.3/64.8	54.7/65.5	50.1/65
3	63.7/66.1	63.3/66.6	60.2/67.1	55.8/66.4

(b) RMS pressure tracking error [dbar].

Load Level (LL)	Load Sense Level (LSL) 0	1	2	3
0	11.7/11	15.8/11.7	28.1/12.8	46.5/13
1	36.2/14.3	35/12.7	40/14.5	51.9/16.8
2	65.4/20.8	59.2/20.6	58.5/19.6	63.7/20.2
3	86.8/36.3	86.6/30.1	78.4/29.4	77.5/26.6

Based on this, the average performance figures and the improvement compared to the bHPU are given in equation 5.60 and 5.61.

$$\overline{RMSe} = 19.4[\text{dbar}] \qquad \downarrow 33.18[\text{dbar}] \tag{5.60}$$

$$\overline{Eff.} = 60.97[\%] \qquad \uparrow 11.43[p.p.] \tag{5.61}$$

As seen, this is a great improvement with respect to the bHPU, corresponding to pressure tracking improvement of 63 [%] and an efficiency improvement of 23 [%]. Though there is still some gap to the simulated performance figures. While some of this may be due to imprecisions of the model, some of it may be due to the oscillations of especially the reference shaft speed.

As to reduce the small oscillations of the reference signals several measures were tested, without resolving the issue. One of the measures was to add a boundary layer to the super twisting algorithm, according to equation 5.62.

$$\nu_s = k_1\sqrt{|\sigma_s|}\text{sgn}(\sigma_s) + w \quad , \qquad \dot{w} = k_2 \frac{\sigma_s}{|\sigma_s| + \epsilon} \tag{5.62}$$

The results can be assessed in appendix G, but are excluded here, as they did not improve compared to the above.

It is deemed likely, that the oscillations arise from the imperfect integration of the implemented discrete backward Euler method, as it introduce a time delay. Furthermore, it is deemed, that time delays are present in the FOC-control of the induction motor. Presence of time delays is a well known issue for sliding mode algorithms and the rather intricate solution is deemed outside the scope of this project [11].

Another plausible reason is the neglected input-dynamics through the induction motor with FOC-control. In [13] it is proposed, that the main reason for chattering of the control signal, when applying second order sliding mode control, is the neglection of the input dynamics, even though they are fast. Here it is concluded that a such control signal will converge to a limit cycle, that relates to the natural frequency of the fast input actuator's time constant [13]. This potential reason and its solution has not been investigated.

Conclusion 6

This project was initiated with the aim of developing control-algorithms for a hydro gear, for tracking a pressure reference, while improving the energy efficiency of the system.

The system model took offset in that of a previous project. Here, the model was concluded to be fairly accurate, though left room for improvement. As a fundamental part of being able to develop the objective control-algorithms, the system model need to be detailed enough as to encompass the dominating dynamics and the main losses of the test bench. This was solved through a revision of the model. Here, a previously neglected component was added and the dynamic order was revised, displaying that among 16 candidate models, the previously developed model offered a good trade-off between precision and number of dynamic model orders, while the model parameters were slightly improved.

The concept of a benchmark HPU was created along with a method of quantifying the performance along 16 different load trajectories with varying load flow and pressure reference. The benchmark HPU was established by setting a with fixed speed and applying a linear controller for pressure tracking through the pressure control unit. By experimental validation the performance figures of the benchmark HPU yielded an average RMS pressure tracking error of 5.23 [bar] and an average system efficiency of 49.54 [%].

Through a capability analysis the pressure and efficiency figures were mapped. The results suggested, that the hydro gear is generally most efficient when choosing the slowest speed that is able to realize the reference pressure, yielding that a number of states in the hydro-gear are saturated. This result was used as basis for the development of a SISO-control structure. With a combination of linear control aided by a super-twisting algorithm based sliding mode disturbance observer (2SMDO) for controlling the shaft speed and a look-up table for an efficient choice of the control unit input, the SISO-structure showed promising performance figures during development. Though, as argued, the look-up table does only resemble the most efficient choice of control unit input for specifically the model it was made from, during steady state.

As to achieve a more generally applicable control solution, a MIMO-structure was developed. The pressure tracking was implemented according to the above method, while the power losses were reduced by a first sliding mode disturbance observer (1SMDO) with a boundary layer. The control objective was formulated as a zero set-point of the power losses, while the boundary layer purposely compromise the otherwise ideal disturbance observer, as to allow for convergence to a bound region, which is regarded as the minimum power loss.

By experimental validation, this controller achieved an RMS pressure tracking error of 1.94 [bar], an improvement of 3.32 [bar] compared to the benchmark HPU. This corresponds to a pressure tracking improvement of 63 [%]. Further, the controller achieved an average system efficiency of 60.97 [%], which is an improvement of 11.43 [p.p.]. This corresponds to an efficiency improvement of 23 [%].

These performance figures are deemed satisfying, leading to the conclusion that: The hydro gear can be controlled through a MIMO-approach with a 2SMDO-based pressure control law, that aims to track a pressure reference and a 1SMDO-based power loss law with a boundary layer, that aims to increase the system efficiency.

Though few issues are identified, the developed control scheme displays promising potential for future industrial application.

Perspectives 7

In this chapter different perspectives of the developed control solution will be presented.

7.1 Reduction of oscillations during constant inputs

As seen from the experimental validation of the MIMO-approach, the control structure induced small oscillations during the regions of constant load. Arising from the control signals, they are unfortunate as it requires unnecessary power to produce especially the accelerations of the rotary shaft group. It is deemed, that these oscillations reduce the efficiency by 1-5 [%]. In the following, solutions to the two plausible reasons for the oscillations, discussed in the control validation are proposed.

It is discussed, that these oscillations may arise from the presence of time delays in the control structure, which are a consequence of the finite sampling frequency explicit Euler integration methods used [14]. In [15], this phenomenon is studied for the super-twisting algorithm, resulting in a entirely new discrete-time variant of the super-twisting algorithm. For improving the results of this project, it is recommended to implement the novel discrete-time variant of the super-twisting algorithm of [15]. Though, the likely presence of further time delays in the FOC-control in the induction motor may impede the potential improvements of the implemented method.

It is also discussed, that the neglection of the input dynamics may be the reason for the oscillations. In [13], an analysis of chattering in systems with second-order sliding modes concludes that neglecting input dynamics may be a main reason for control chattering, even though the input dynamics are fast. The solution to this may likely be the introduction of higher order sliding modes.

7.2 Energy Efficient Control of the Induction Motor

In the pursuit of increased efficiency, it may be meaningful to consider energy efficient control of the induction motor itself. While, the conventional FOC-method applied in the project is generally rather efficient, [3] suggest several measures to increase the efficiency further. One of the methods, that offers rather simple implementation into the existing FOC-control, is to make a variable direct axis reference current $I_{sd,ref}$, instead of having it constant. Based on the loss model, the reference current $I_{sd,ref}$ can be controlled online as to minimize the losses.

This method is in [16] implemented on a 7.5 [kW] induction motor with FOC control, yielding an efficiency increase of 3 [%] for the motor. It is deemed likely, that similar results may be obtained for the induction motor of the hydro gear.

7.3 Potential Overheating of the Induction Motor

When recognising that the hydro gear is generally most efficient, when $x = x_{max}$, such that the pump operates like a variable speed fixed displacement pump, a consequence of this operation is an elevated torque level on the induction motor, compared to the benchmark HPU. An increased amount of the system losses will thus be placed in the induction motor. This may cause the induction motor to overheat more frequently. When overheating, the build-in protection of the motor reduces the maximum torque which is likely to cause the pressure tracking to deteriorate drastically. This is therefore deemed to be a potential problem needing to be addressed.

7.4 Industrial Application

The developed solution is deemed to be highly industrially relevant, as it by far and large only requires a software update of *'any'* variable speed and displacement HPU, that is equipped with similar hydraulic control units, in order to obtain an energy efficient HPU with good pressure tracking. Though, indeed this control method comes with a set of requirements:

1. A highly similar hydraulic schematic, with the same or highly similar control unit to the ER72 from the manufacturer Bosch Rexroth.
2. A rather accurate estimate or a measurement of the load flow. This could e.g. be obtained from a model as for the project, a flow-meter or an estimate produced by the load, which also has load sensing for producing a pressure reference.
3. Quantified the following 18 model parameters:
    - Induction motor parameters: Rotor and stator resistances R_s and R_r, magnetizing, stator and rotor inductances L_m, L_s and L_r and the number of pole pairs, p_b. All of these were for the project test bench readily available through the IndraWorks PLC programming software.
    - Variable displacement pump parameters: Area of control piston A_{sx} and maximum displacement of the swash plate control pistons x_{max}. These were in the project obtained from Bosch Rexroth. The maximum volumetric displacement per rotation D_s, which was stated in the data sheet of the pump.
    - Equivalent static flow gains: K_{sc}, K_{ct}. These were in the project identified through optimization.
    - Parameters of the control unit: The spring rate K_{cy}, control input-force scaling K_u, control volume V_c and maximum displacement of the electrically actuated control valve spool y_{max}. These were in the project identified through optimization.
    - The output control volume V_s, which was estimated the volume of the hoses on the output side of the pump.
    - Rotary group parameters: Equivalent viscous friction coefficient B_ω and combined moment of inertia J.

If these requirements are met, it is deemed likely that the developed MIMO-control will be able to track a pressure reference, while improving the system efficiency on a given hydro gear.

With the non-linear model and a catalogue of hardware solutions with corresponding model parameters, it would be feasible to develop a tuning/sales software which takes some defined system components, with e.g. the larger pump A10VZO-028, an approximate load trajectory and then the software approximates the system performance figures along with appropriate tuning of the controllers. The tuning of the controllers would then follow the design rules defined during the control development, though they need to be more specifically defined, e.g. that $C_s = \frac{\omega_n}{6}$, with ω_n being the natural frequency of the closed loop induction motor with FOC. Based on this it would be possible to make the developed control solution easily accessible for the sales person and applicable for the technician.

Bibliography

[1] Jesper Mortensen. *Modelling of a Speed and Displacement-Variable Hydraulic Pump*. Tech. rep. AAU, 2019.

[2] George E. Totten and Victor J. De Negri. *Handbook of Hydraulic Fluid Technology*. CRC Press, 2011. ISBN: 978-1-4200-8527-3.

[3] Flemming Abrahamsen. "Energy optimal control of induction motor drives". ISBN: 8789179269. PhD thesis. Pontoppidanstraede 101, DK-9220 Aalborg East: Institute of Energy Technology, Aalborg University, 2000.

[4] K.J. Keesman. *System Identification: An Introduction*. Advanced Textbooks in Control and Signal Processing. Springer London, 2011. ISBN: 9780857295224.

[5] ISO 4409:2019. *Hydraulic fluid power - Positive-displacement pumps, motors and integral transmissions - Methods of testing and presenting basic steady state performance*. Standard. International Organization for Standardization, 2019.

[6] Peter Achten et al. "Measuring the losses of hydrostatic pumps and motors - A critical review of ISO4409:2007". In: *ASME* FPMC2019-1615.1 (2019).

[7] ISO 14414:2019. *Pump system energy assessment*. Standard. International Organization for Standardization, 2019.

[8] Bosch Rexroth AG. *Directional control valves, direct operated, with electrical position feedback and integrated electronics (OBE)*. Type 4WRPEH. `http://www.boschrexroth.com/`, 2018.

[9] Bosch Rexroth AG. *Axial piston variable pump, A10VSO Series 31*. `http://www.boschrexroth.com/`, 2016.

[10] J.J.E. Slotine and W. Li. *Applied Nonlinear Control*. Prentice Hall, 1991. ISBN: 9780130408907.

[11] L. Fridman, J. Moreno, and R. Iriarte. *Sliding Modes after the first Decade of the 21st Century: State of the Art*. Lecture Notes in Control and Information Sciences. Springer Berlin Heidelberg, 2011. ISBN: 9783642221637.

[12] Y. Shtessel et al. *Sliding Mode Control and Observation*. Control Engineering. Springer New York, 2013. ISBN: 9780817648930.

[13] I Boiko et al. "Analysis of Chattering in Systems With Second-Order Sliding Modes". eng. In: *IEEE Transactions on Automatic Control* 52.11 (2007), pp. 2085–2102. ISSN: 0018-9286.

[14] Charles L. Phillips and John M. Parr. *Feedback Control Systems*. 5th edition ISBN: 978-0-13-186614-0. Pearson, 2011.

[15] Stefan Koch and Markus Reichhartinger. "Discrete-time equivalents of the super-twisting algorithm". eng. In: *Automatica* 107 (2019), pp. 190–199. ISSN: 0005-1098.

[16] Frederik Ødum Nielsen, Lasse Nørby Nielsen, and Nikolaj Grønkær. *Intelligent Control Design Improving the Energy Efficiency & Dynamic Performance of a Novel Self-contained Cylinder Drive Concept*. Tech. rep. AAU, 2019.

[17] Bosch Rexroth AG. *Rexroth IndraDrive, Supply Units, Power Sections, HMV, HMS, HMD, HCS02, HCS03*. HCS03.1E-W0070-A-05-NNNV. http://www.boschrexroth.com/, 2017.

[18] Bosch Rexroth AG. *Rexroth IndraDyn A Asynchronous Motors MAD / MAF*. MAD100D-0250-SA-M2-AH0-05-N1. http://www.boschrexroth.com/, 2011.

[19] Bosch Rexroth AG. *Axial piston units A10FZO, A10VZO and A10FZG, A10VZG, Series 10 for variable-speed drives*. A10VZO-018DRG00/10R-VRC12N00. http://www.boschrexroth.com/, 2016.

[20] Paresh Chandra Sen. *Principles of electric machines and power electronics*. John Wiley & Sons, 2007.

Appendices

Hydro Gear Test Bench Main Component Specification A

This specification is from [1].

The main components of the hydro gear test bench are noted in table A.1.

Table A.1: The main components of the test bench. The manufacturer is Bosch Rexroth.

Frequency inverter drive:	IndraDrive, HCS03.1E-W0070
Induction motor:	IndraDyn A, MAD100D-0250
Variable displacement axial piston pump:	A10VZO-018
Control unit for piston pump:	ZA10V-ER72
Proportional control valve for output:	4WRPEH 6 C3 B40L

In the following bullets, key parameters of each of the main components will be presented.

- **Frequency inverter drive:** The inverter drive is rated for 15 [kW] with a rated current of 45 [A] [17].
- **Induction Motor:** The induction motor has a rated power of 13.1 [kW], with a rated torque and speed of 50 [Nm] and 2500 [rpm] respectively. The maximum torque and speed is 118.7 [Nm] and 9000 [rpm]. It is a three pole pair machine [18].
- **Variable displacement axial piston pump:** The variable displacement pump is of the axial piston pump type, with a maximum displacement of 18 [mL] per revolution. It has a maximum rotational speed of 3300 [rpm]. Hence, at maximum speed and displacement, the pump outputs 59 [L/min] [19].
- **Control unit for piston pump:** The ER72 is a electro-hydraulic pressure control 'valve' which sets a certain pressure by a specified current into its solenoid. If the load changes, the swivel angle of the pump will change in order to sustain the set pressure. [9]
- **Proportional control valve for output:** The proportional control valve of the output stage is used as load for the system. The valve has a rated flow of 40 [L/min] per control edge at a pressure drop of 35 [bar] and a linear flow/input current characteristic [8].

The combined system is rated for 42 [L/min] at 170 [bar] yielding an output power of 11.83 [kW].

Steady State Torque-Speed Curves of the Induction Motor B

In [1], the steady state torque speed curves of the induction motor were defined as depicted in figure B.1.

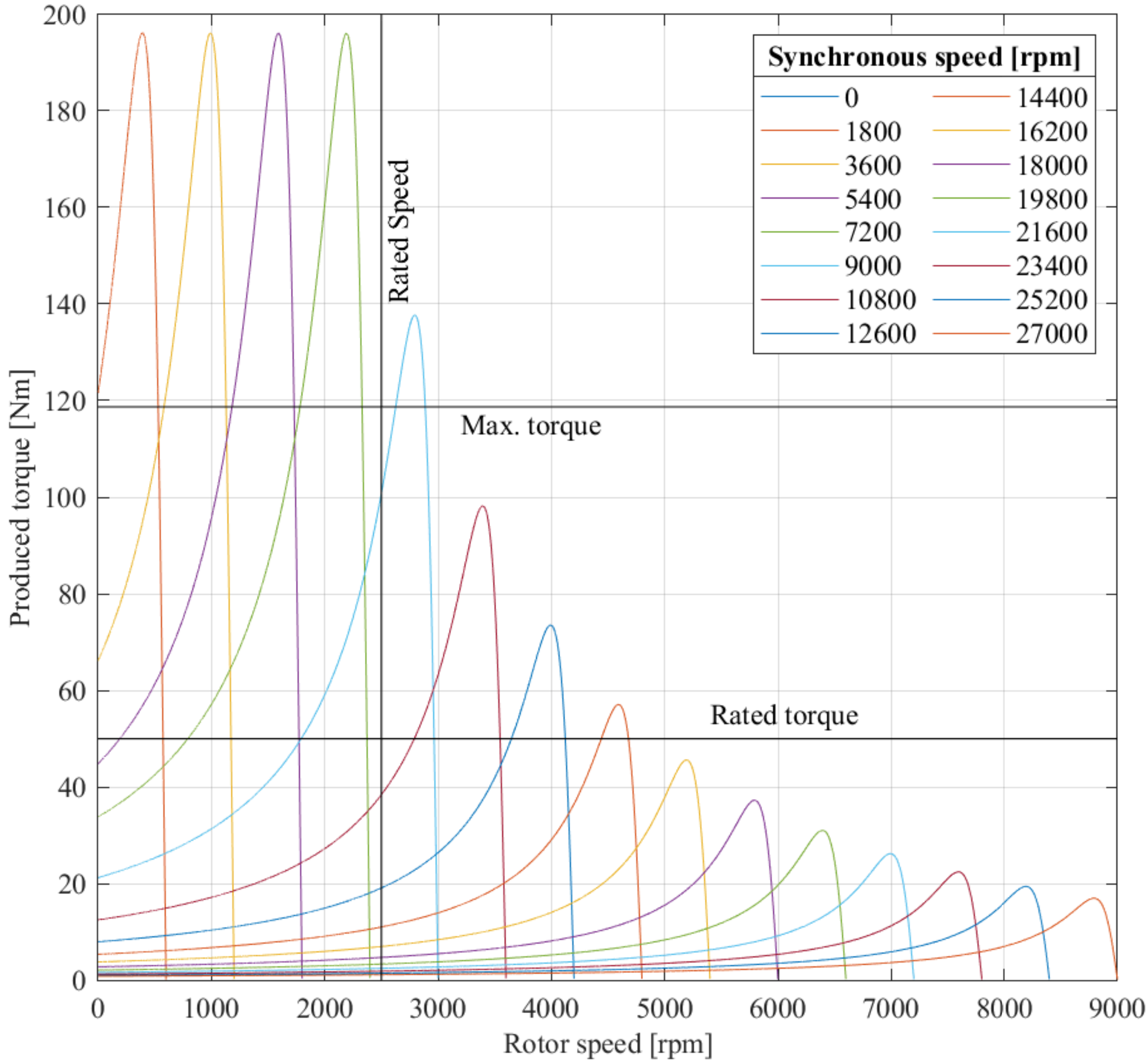

Figure B.1: Torque-speed curves of the induction motor as found in [1].

Approximation of the Natural Frequency and Bandwidth of the Induction Motor with FOC-control

C

In this appendix, the natural frequency of the outer velocity loop of the induction motor with field oriented control, will be estimated. Due to the relatively high complexity of an analytical solution, the dynamics are linearised and studied in the Laplace domain.

As stated previously, the torque of the induction motor is defined according to equation C.1.

$$\tau_{em} = -\frac{3p_b L_m}{2}\left(\frac{\Psi_{rd}\Psi_{sq} - \Psi_{sd}\Psi_{rq}}{\sigma_{IM}}\right) \tag{C.1}$$

By utilization of the relations $\Psi_{sd} = L_m I_{rd} + L_s I_{sd}$, $\Psi_{sq} = L_m I_{rq} + L_s I_{sq}$, $\Psi_{rd} = L_m I_{sd} + L_r I_{rd}$, $\Psi_{rq} = L_m I_{sq} + L_r I_{rq}$ and $\sigma_{IM} = L_m^2 - L_s L_r$ the torque is simplified into equation C.2.

$$\tau_{em} = \frac{3p_b}{2}\left(I_{sq}\Psi_{sd} - I_{sd}\Psi_{sq}\right) \tag{C.2}$$

The rotor EMF is induced by the air gap magnetic field according to Faraday's law of induction. Consequently, the rotor EMF is lagging the air gap magnetic field by 90 [°]. When the induction motor is operating at its nominal value, the slip is near zero and the rotor leakage inductance has a small reactance. This is used to assume that the rotor in general is resistive. Then, the rotor current is in phase with the rotor EMF, and is lagging the air gap magnetic field by 90 [°] [20]. For induction machines, the orientation of the *dq*-reference frame, is principally arbitrary. Letting the *d*-axis align with Ψ_s yields that $\Psi_{sq} = 0$ and $I_{rd} = 0$. Based on this, the torque equation is simplified according to equation C.3.

$$\tau_{em} \approx \frac{3p_b}{2}\left(I_{sq}(L_m \cancel{I_{rd}} + L_s I_{sd}) - I_{sd}\cancel{\Psi_{sq}}\right) \tag{C.3a}$$

$$\approx \frac{3}{2}p_b L_s I_{sd} I_{sq} \tag{C.3b}$$

Assuming that the direct axis stator current is ideally controlled to be constant, yielding $I_{sd} = I_{sd,ref}$, the torque is directly proportional to the quadrature axis current.

By disregarding the load torque introduced by the pump, the dynamic equation for the rotor shaft is linearised according to equation C.4. Indeed this simplification disregards some coupled dynamics, which would most likely reduce the acceleration of the rotor shaft making this simplification non-conservative.

$$\dot{\omega}_m = J^{-1}(\tau_{em} - \cancel{D_s K_{\theta p} x(P_s - P_t)} - B_\omega \omega_m) \tag{C.4}$$

From the simplified dynamic rotor shaft equation, its transfer function can be established according to equation C.5 while the open loop dynamics are described by equation C.6, with

D_ω being the shaft speed PI-controller.

$$G_\omega = \frac{\omega_m}{I_{sq,ref}} = \frac{3}{2} p_b L_s I_{sd,ref} \frac{1}{Js + B_\omega} = \frac{3}{2B_\omega} p_b L_s I_{sd,ref} \frac{1}{\frac{J}{B_\omega} s + 1} \tag{C.5}$$

$$D_\omega \cdot G_\omega = \frac{\omega_m}{\omega_{m,ref} - \omega_m} = \frac{3p_b L_s I_{sd,ref}}{2J} \frac{K_p s + K_i}{s^2 + \frac{B_\omega}{J} s} \tag{C.6}$$

As seen, the open loop system is of type 1 due to the presence of a free integrator, yielding zero steady state error of the closed loop system. The closed loop dynamics are then described by equation C.7.

$$\begin{aligned} G_{cl}(s) &= \frac{\omega_m}{\omega_{m,ref}} = \frac{D_\omega \cdot G_\omega}{1 + D_\omega \cdot G_\omega} \\ &= \frac{3p_b L_s I_{sd,ref}}{2J} \frac{K_p s + K_i}{s^2 + \left(\frac{3I_{sd,ref} K_p L_s p_b}{2J} + \frac{B_\omega}{J} \right) s + \frac{3I_{sd,ref} K_i L_s p_b}{2J}} \end{aligned} \tag{C.7}$$

Hence, the natural frequency of the closed loop system is evaluated as $\omega_n = \sqrt{\frac{3I_{sd,ref} K_i L_s p_b}{2J}} = 149$ [rad/s] while the bandwidth is numerically evaluated to $\omega_B = 408$ [rad/s] [14].

Experimental data for Open Loop, Fixed Speed, Variable Displacement HPU

D

In this appendix, the experimental data for the open loop fixed speed variable displacement HPU is stated. As described previously, the open loop control is only able to track LSL0. The measured performance figures are stated in table D.1.

Table D.1: Measured performance figures for the open loop fixed speed variable displacement HPU

$RMSe$ [dbar] / $Eff.$ [%]		Load Sense Level (LSL)			
		0	1	2	3
Load Level (LL)	0	$^{9.9}/_{38.9}$	$^{-}/_{-}$	$^{-}/_{-}$	$^{-}/_{-}$
	1	$^{30}/_{52.7}$	$^{-}/_{-}$	$^{-}/_{-}$	$^{-}/_{-}$
	2	$^{53.6}/_{60.4}$	$^{-}/_{-}$	$^{-}/_{-}$	$^{-}/_{-}$
	3	$^{76}/_{64.6}$	$^{-}/_{-}$	$^{-}/_{-}$	$^{-}/_{-}$

The corresponding plots of the pressure tracking, the load, the control inputs and measured powers are depicted in the following:

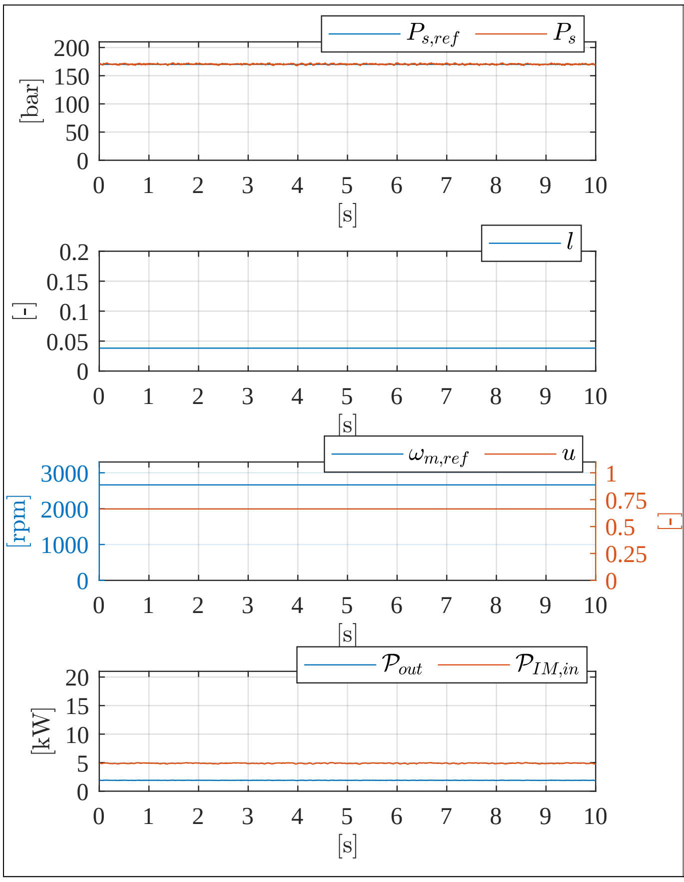

(a) LL0, LSL0.

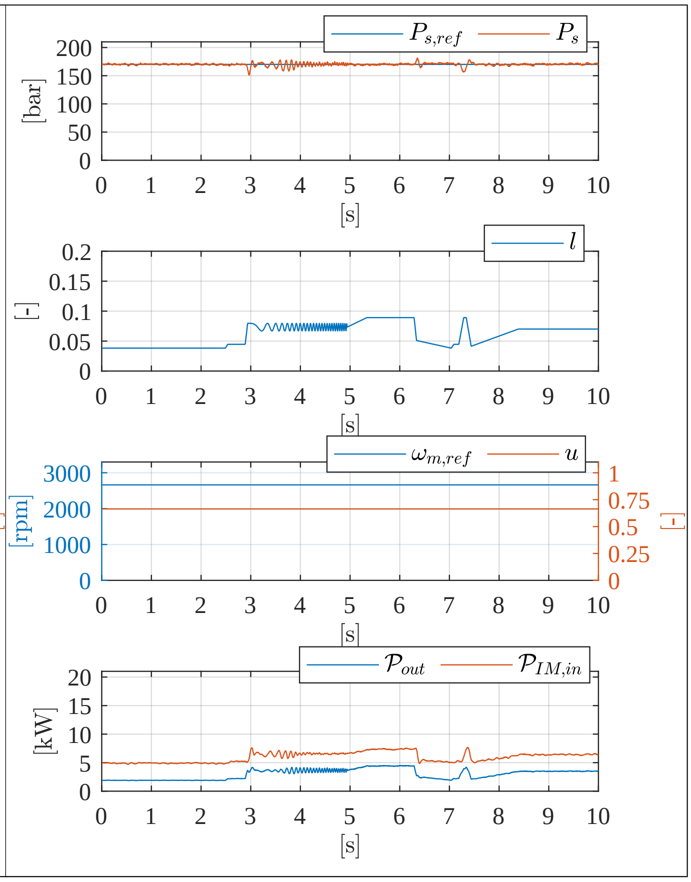

(b) LL1, LSL0.

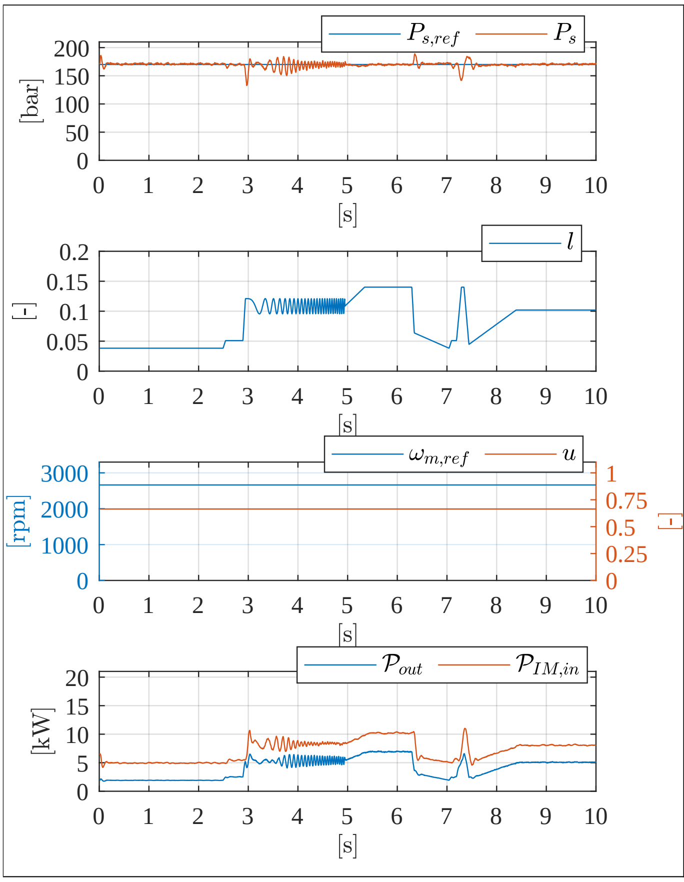

(c) LL2, LSL0

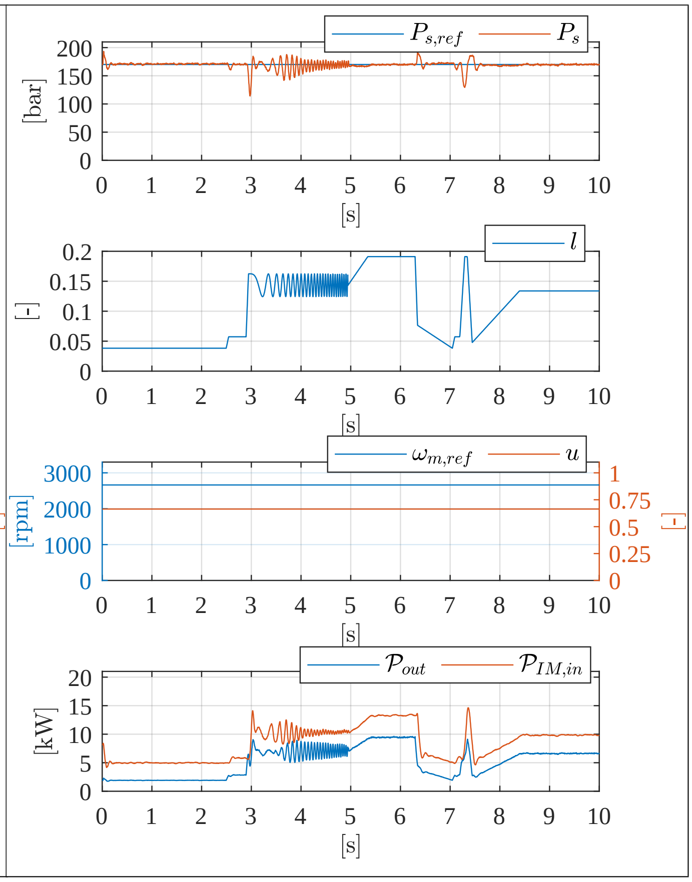

(d) LL3, LSL0.

Experimental data for bHPU E

In this appendix, the experimental data for the benchmark HPU is stated. The measured performance figures are stated in table E.1.

Table E.1

$RMSe$ [dbar] / $Eff.$ [%]	Load Sense Level (LSL) 0	1	2	3
Load Level (LL) 0	$^{11.7}/_{38.6}$	$^{15.8}/_{35.9}$	$^{28.1}/_{32.5}$	$^{46.5}/_{28.5}$
1	$^{36.2}/_{52.7}$	$^{35}/_{50.2}$	$^{40}/_{46.4}$	$^{51.9}/_{41.7}$
2	$^{65.4}/_{60.2}$	$^{59.2}/_{58.3}$	$^{58.5}/_{54.7}$	$^{63.7}/_{50.1}$
3	$^{86.8}/_{63.7}$	$^{86.6}/_{63.3}$	$^{78.4}/_{60.2}$	$^{77.5}/_{55.8}$

Based on this, the average performance figures are the following:

$$\overline{RMSe} = 52.58[\text{dbar}] \tag{E.1}$$

$$\overline{Eff.} = 49.54[\%] \tag{E.2}$$

The corresponding plots of the pressure tracking, the load, the control inputs and measured powers are depicted in the following:

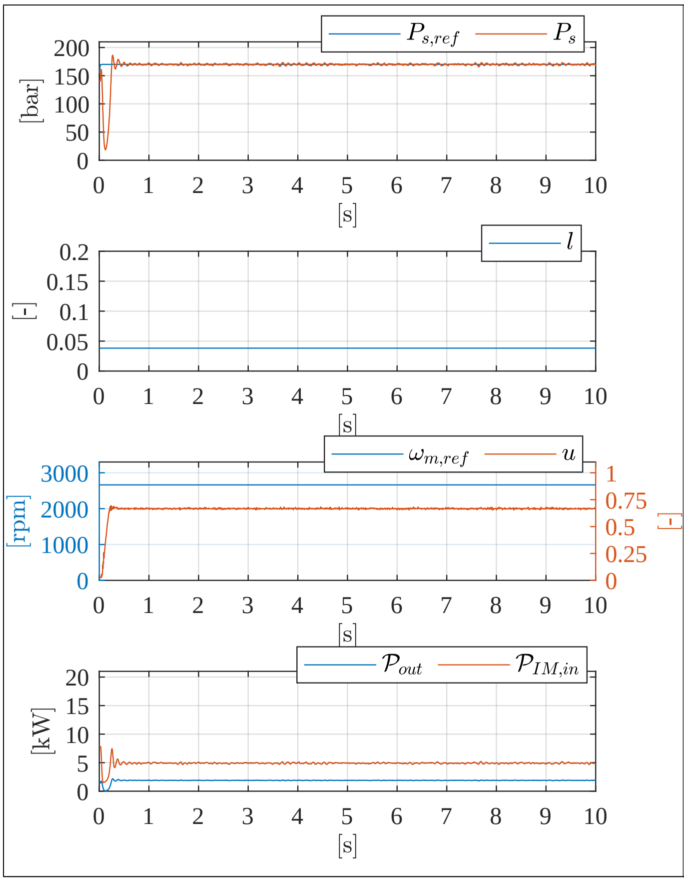

(a) LL0, LSL0.

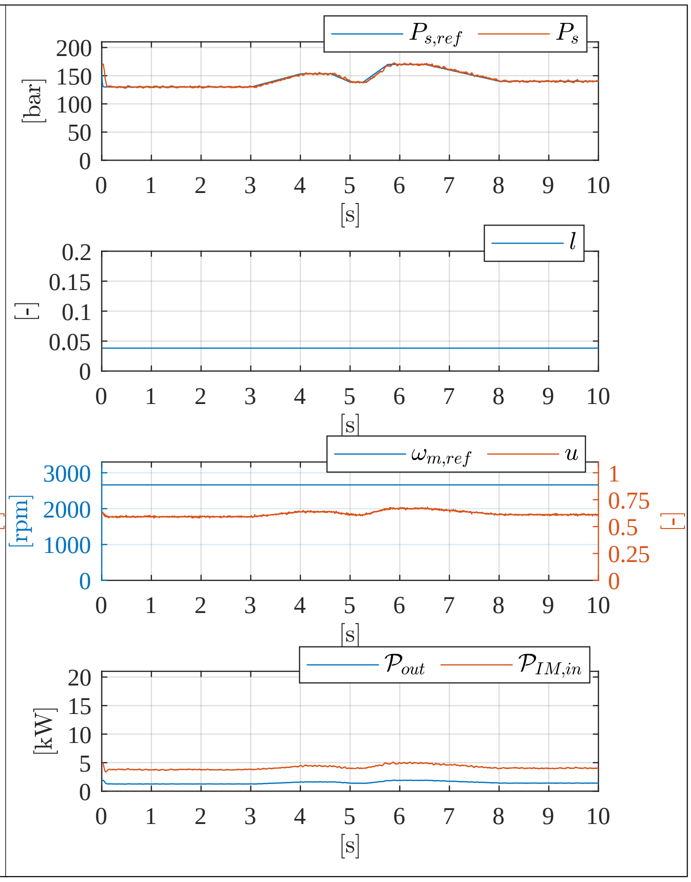

(b) LL0, LSL1.

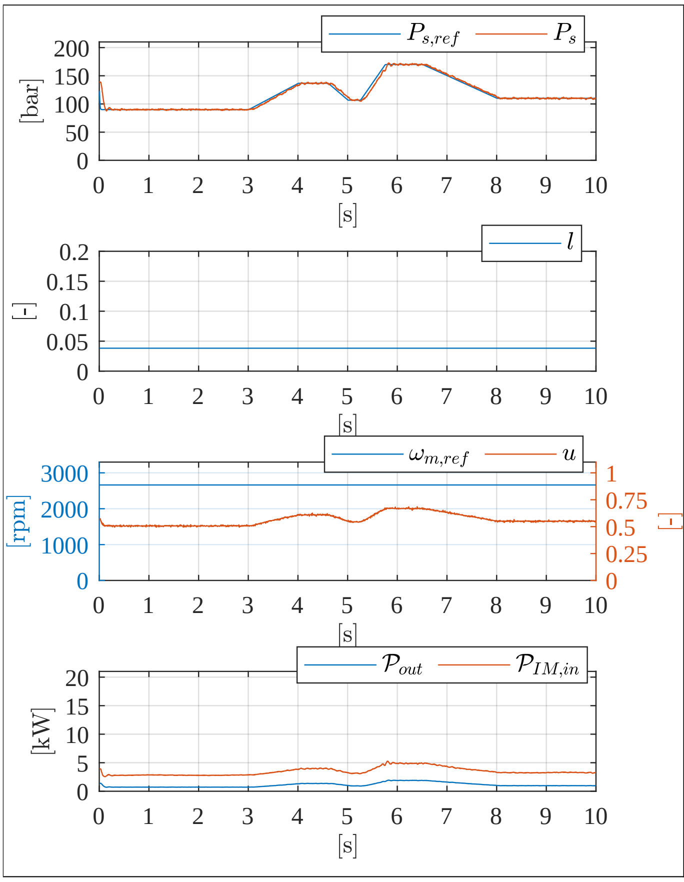

(c) LL0, LSL2.

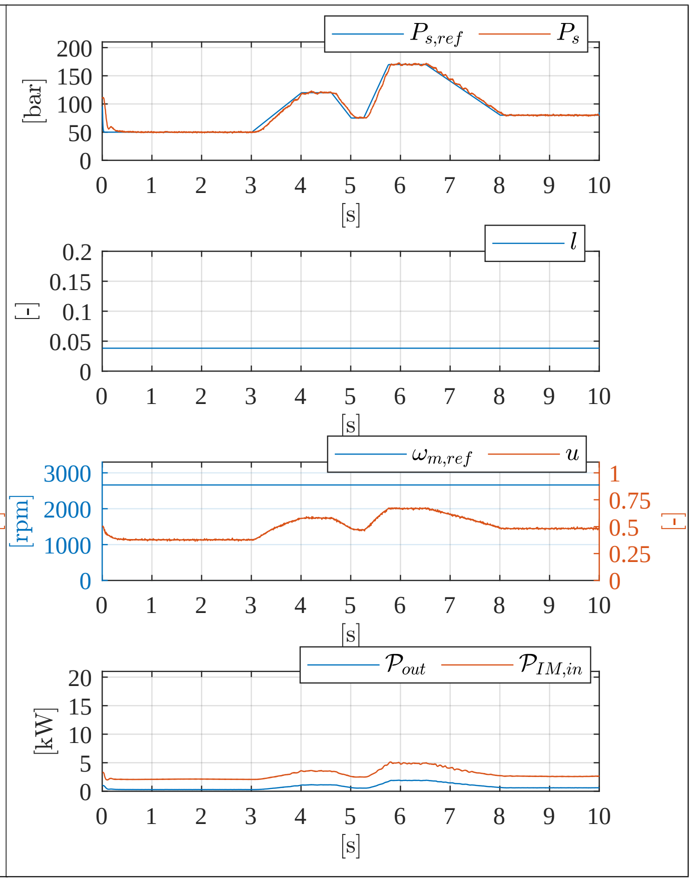

(d) LL0, LSL3.

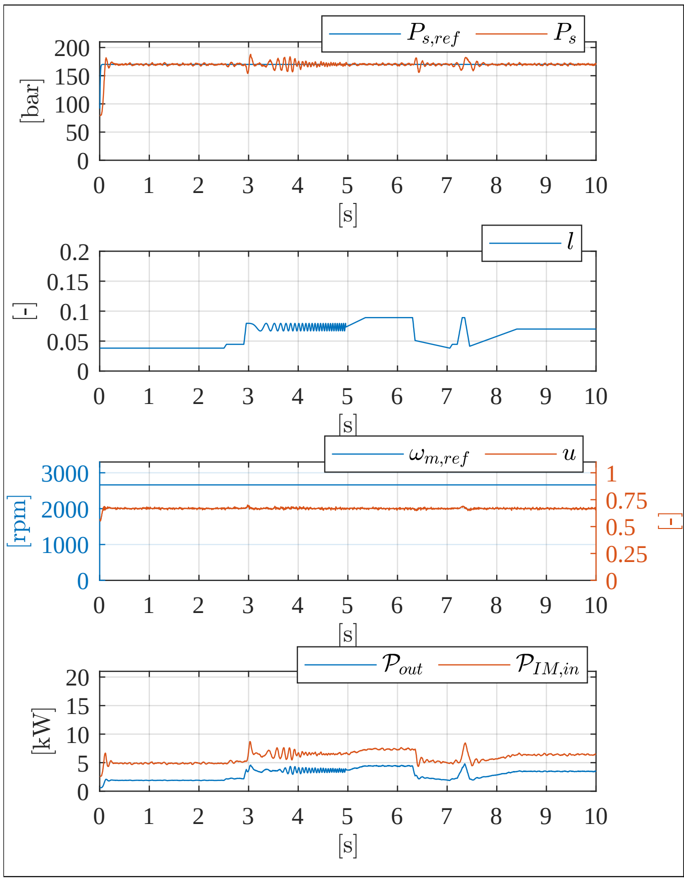

(a) LL1, LSL0.

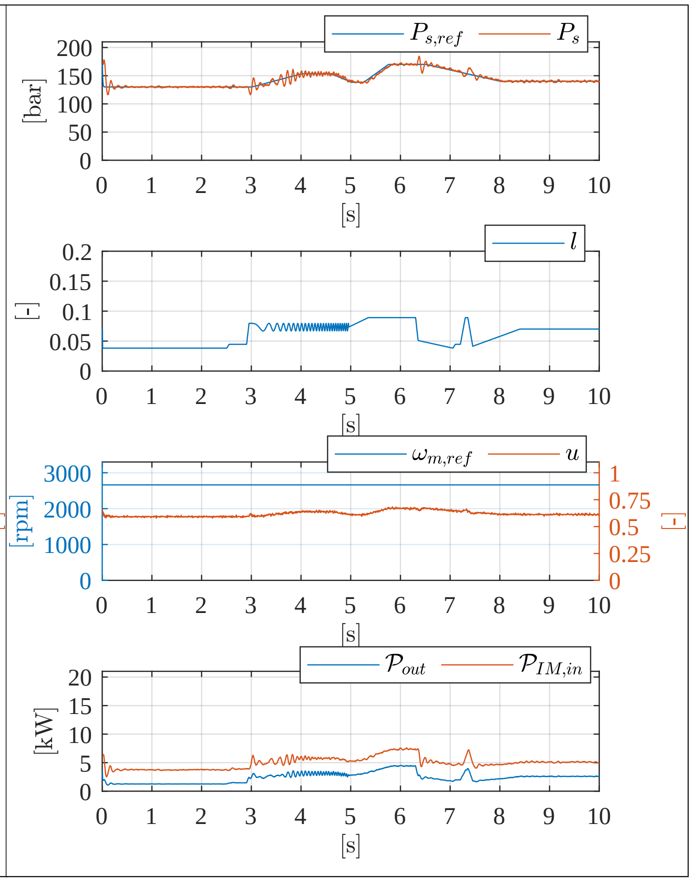

(b) LL1, LSL1.

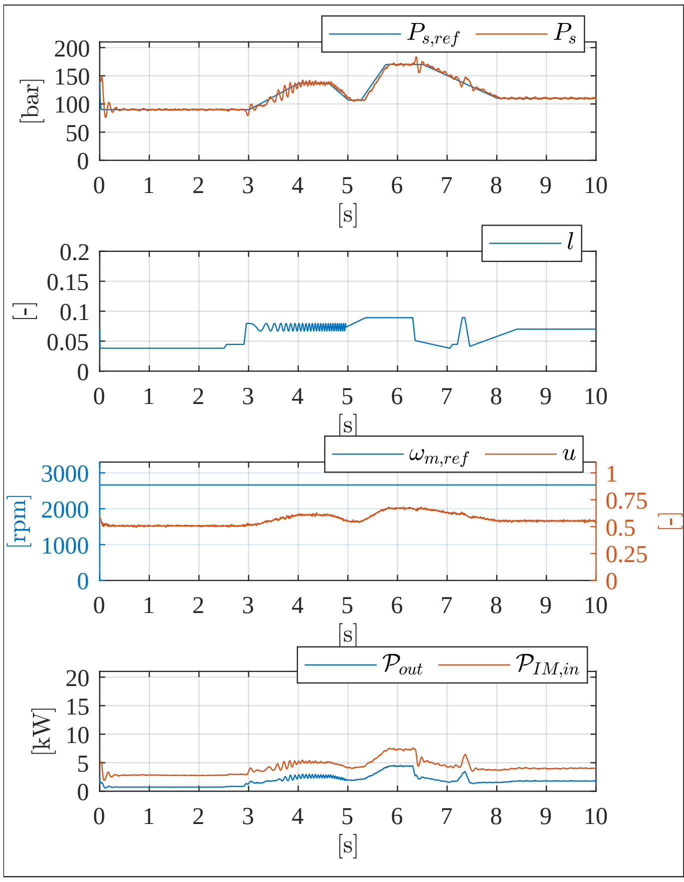

(c) LL1, LSL2.

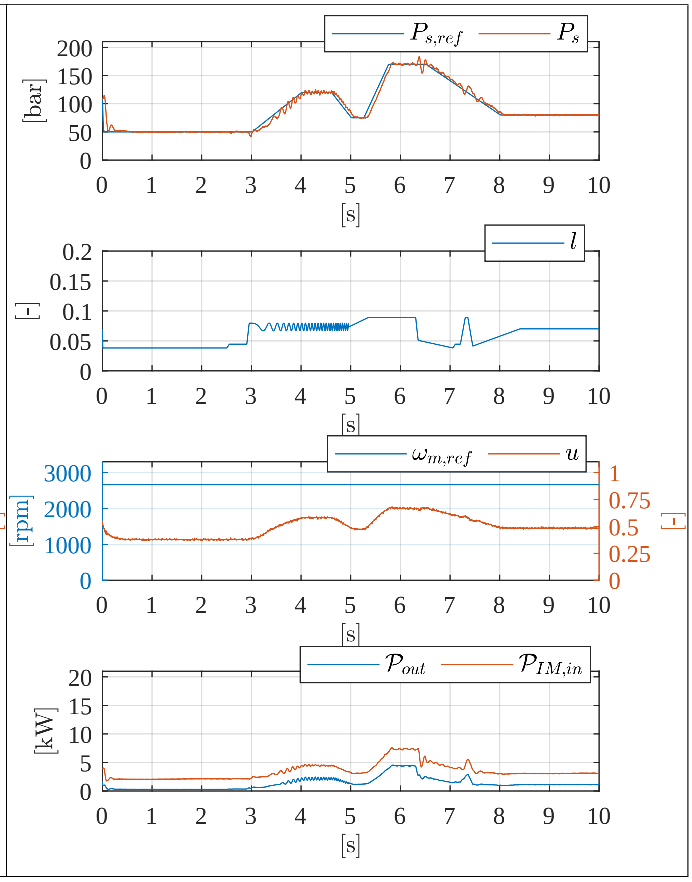

(d) LL1, LSL3.

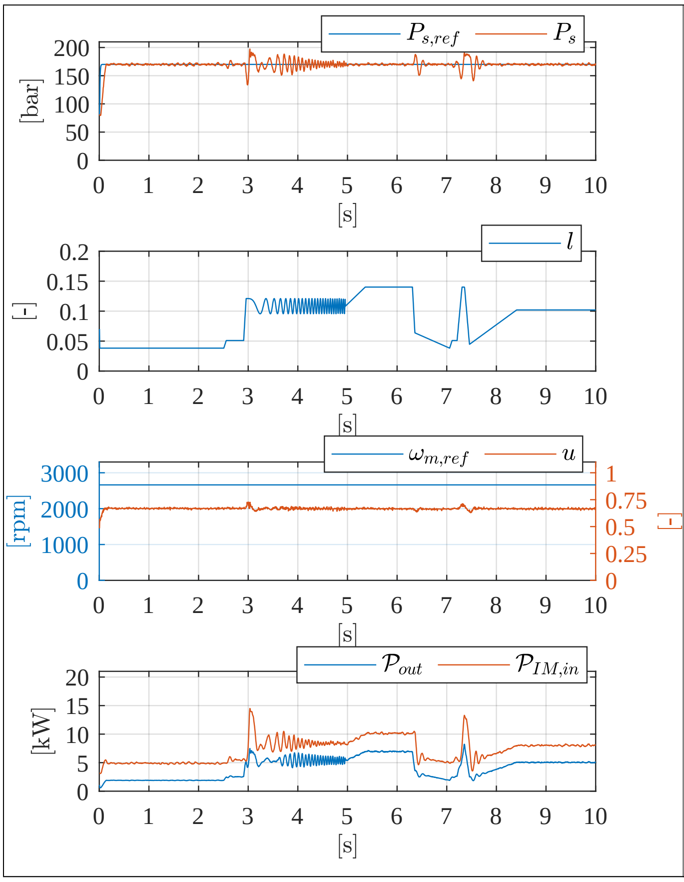

(a) LL2, LSL0.

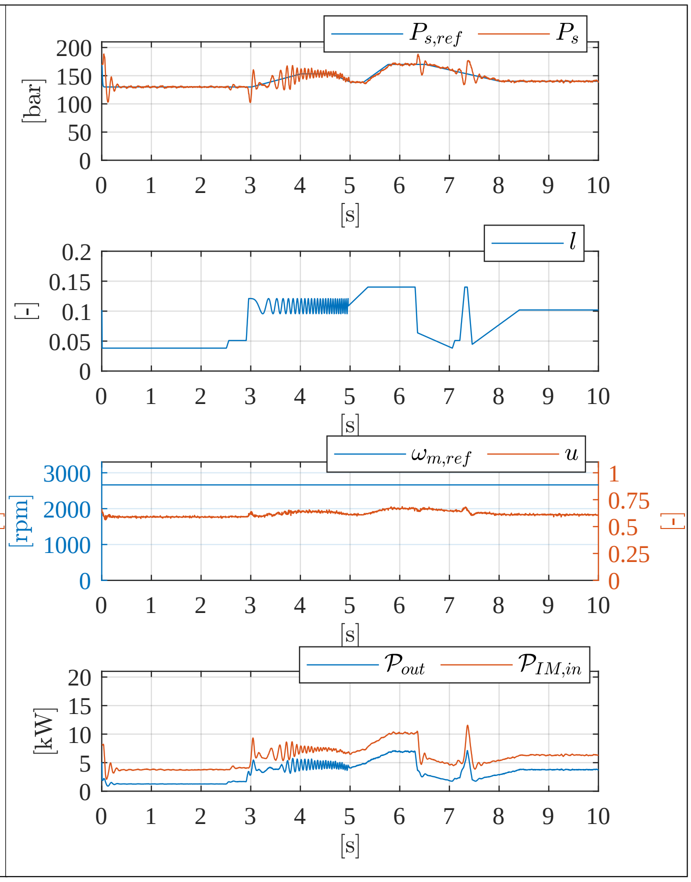

(b) LL2, LSL1.

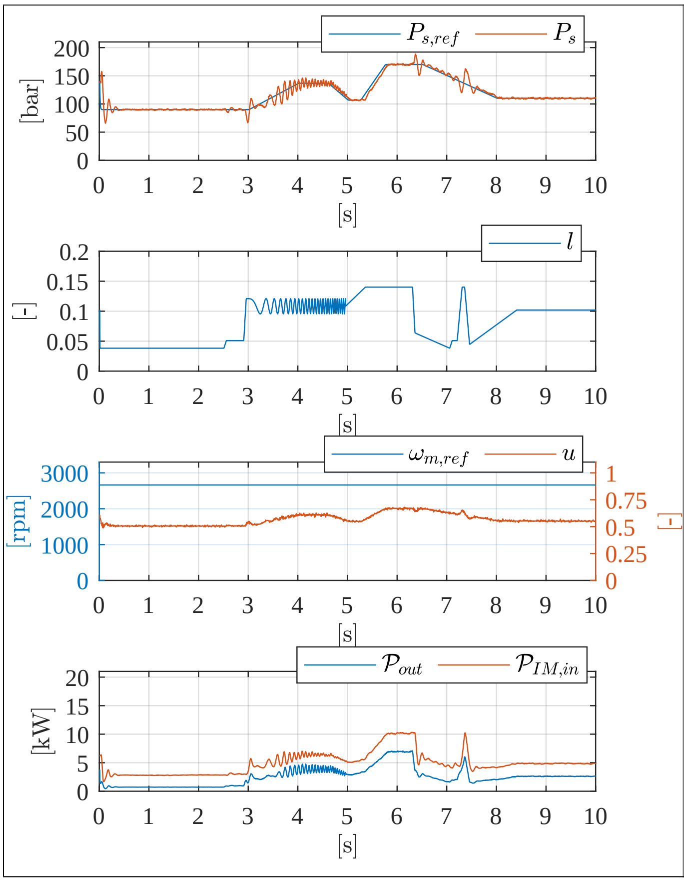

(c) LL2, LSL2.

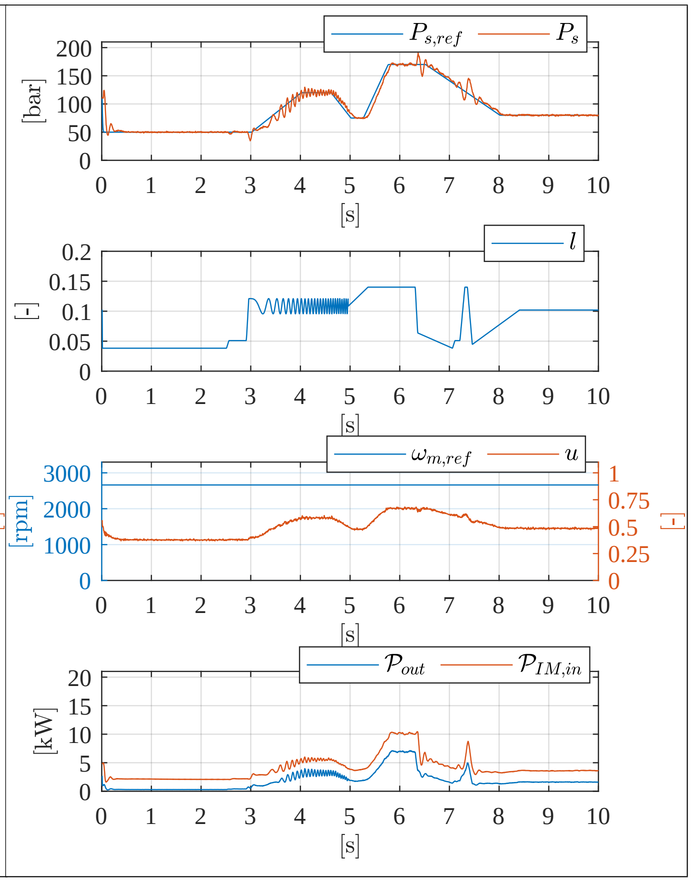

(d) LL2, LSL3.

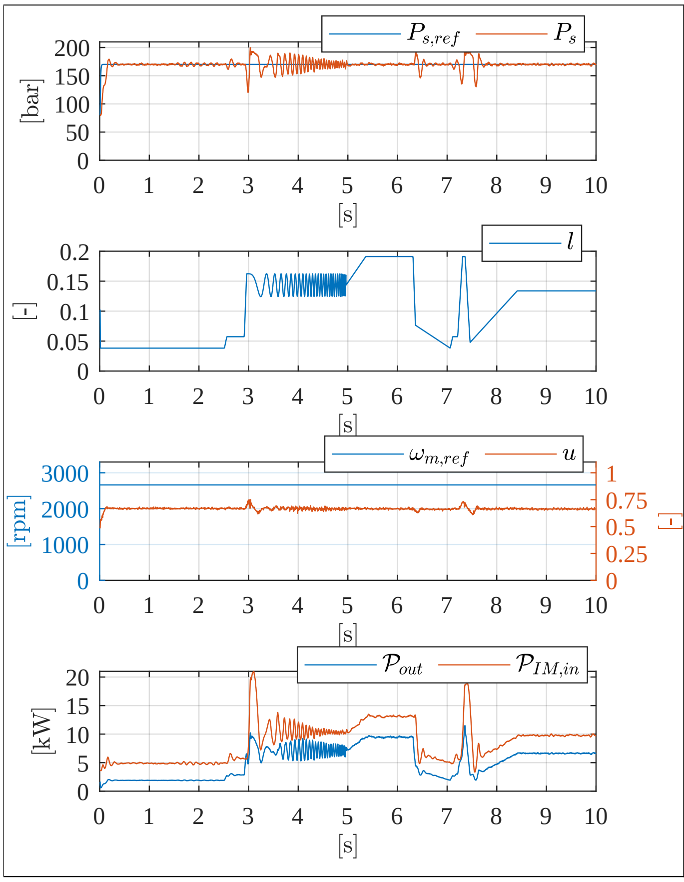

(a) LL3, LSL0.

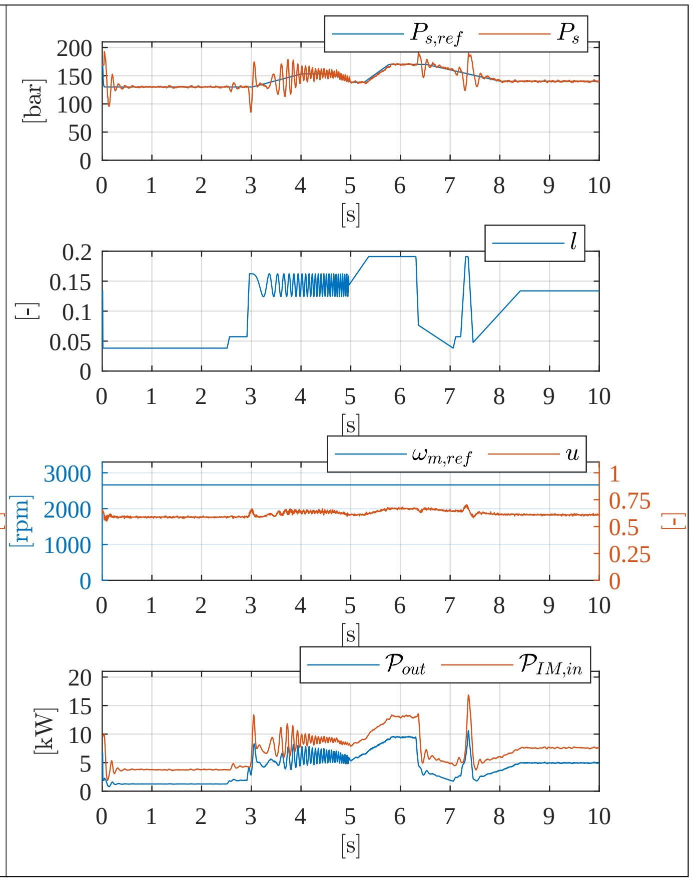

(b) LL3, LSL1.

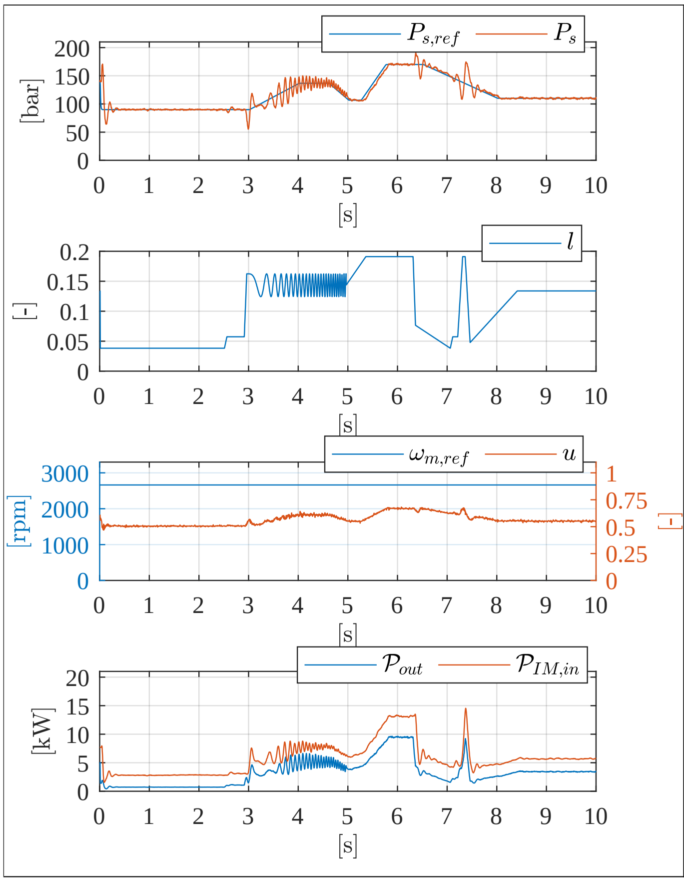

(c) LL3, LSL2.

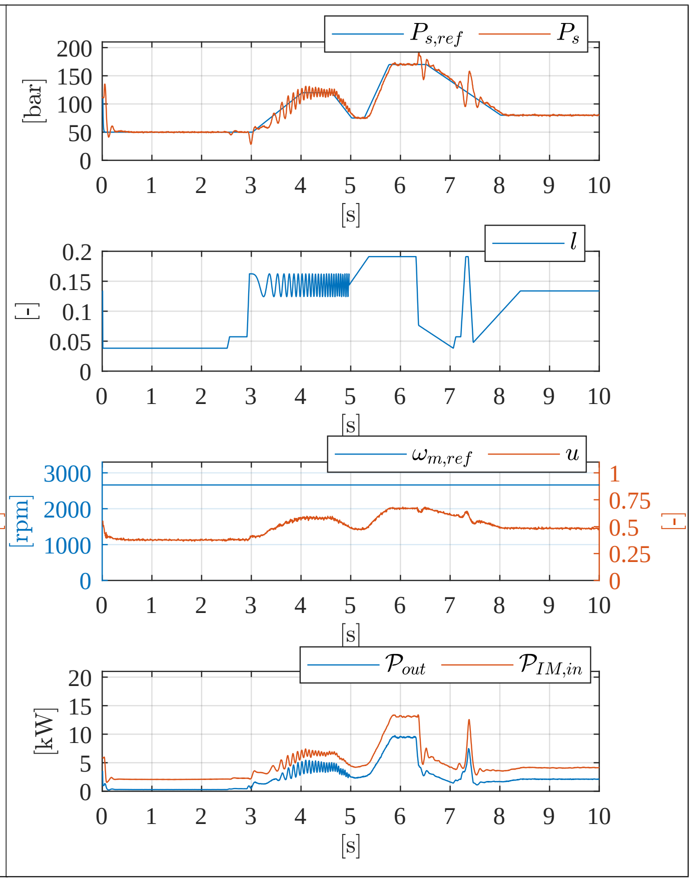

(d) LL3, LSL3.

Experimental data for 2SMDO and 1SMDO + boundary layer

F

In this appendix, the experimental data for the developed MIMO control of the hydro gear is stated. The measured performance figures are stated in table F.1.

Table F.1

$RMS(e_s)$ [dbar] / $Eff.$ [%]		Load Sense Level (LSL) 0	1	2	3
Load Level (LL)	0	$^{11}/_{50.5}$	$^{11.7}/_{51}$	$^{12.8}/_{52.1}$	$^{13}/_{50.8}$
	1	$^{14.3}/_{60.6}$	$^{12.7}/_{60.7}$	$^{14.5}/_{61.9}$	$^{16.8}/_{62.4}$
	2	$^{20.8}/_{64.1}$	$^{20.6}/_{64.8}$	$^{19.6}/_{65.5}$	$^{20.2}/_{65}$
	3	$^{36.3}/_{66.1}$	$^{30.1}/_{66.6}$	$^{29.4}/_{67.1}$	$^{26.6}/_{66.4}$

Based on this, the average performance figures are the following:

$$\overline{RMSe} = 19.4[\text{dbar}] \qquad \downarrow 33.18[\text{dbar}] \tag{F.1}$$

$$\overline{Eff.} = 60.97[\%] \qquad \uparrow 11.43[p.p.] \tag{F.2}$$

The corresponding plots of the pressure tracking, the load, the control inputs and measured powers are depicted in the following:

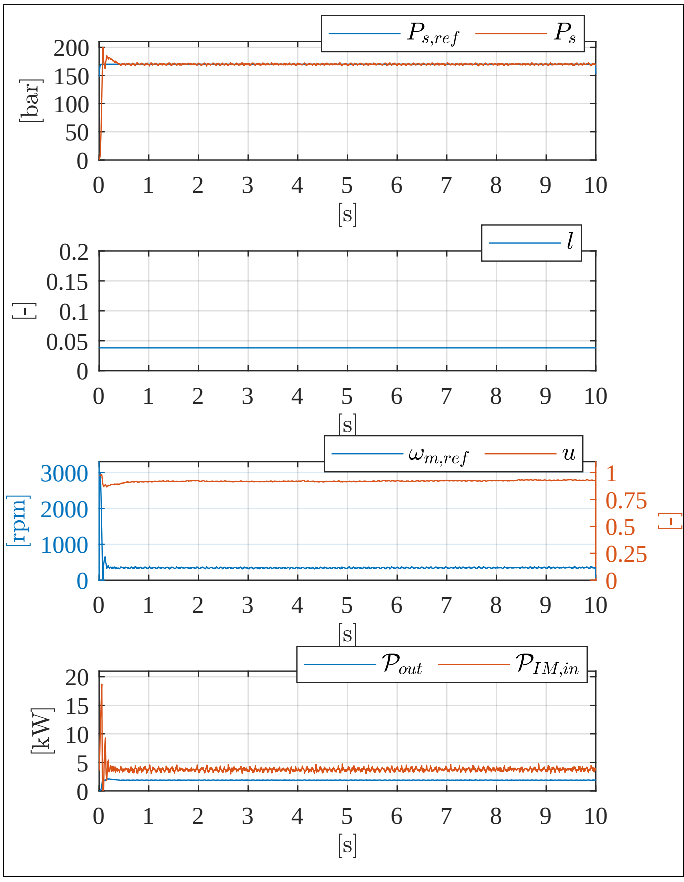

(a) LL0, LSL0.

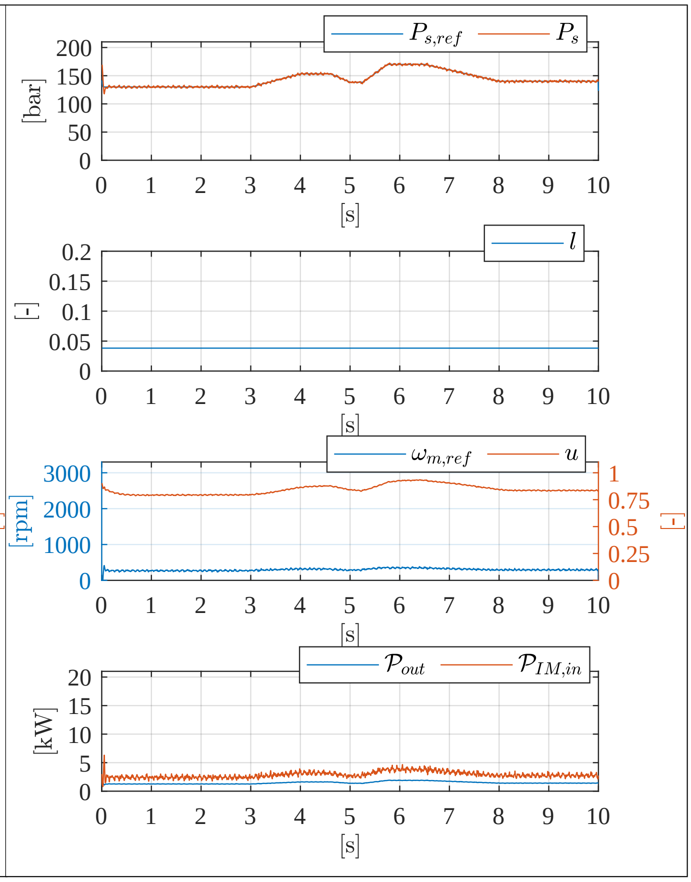

(b) LL0, LSL1.

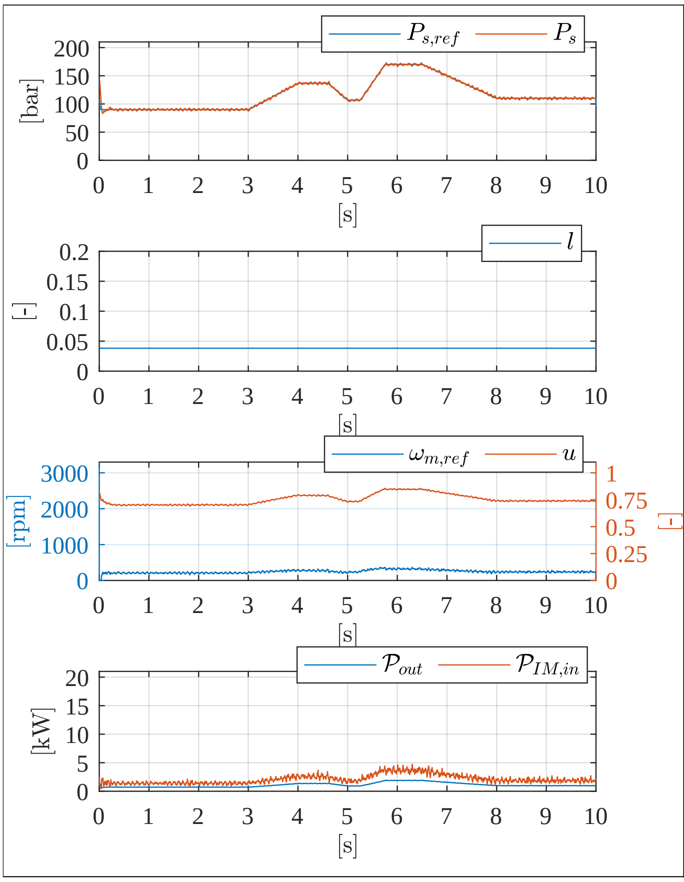

(c) LL0, LSL2.

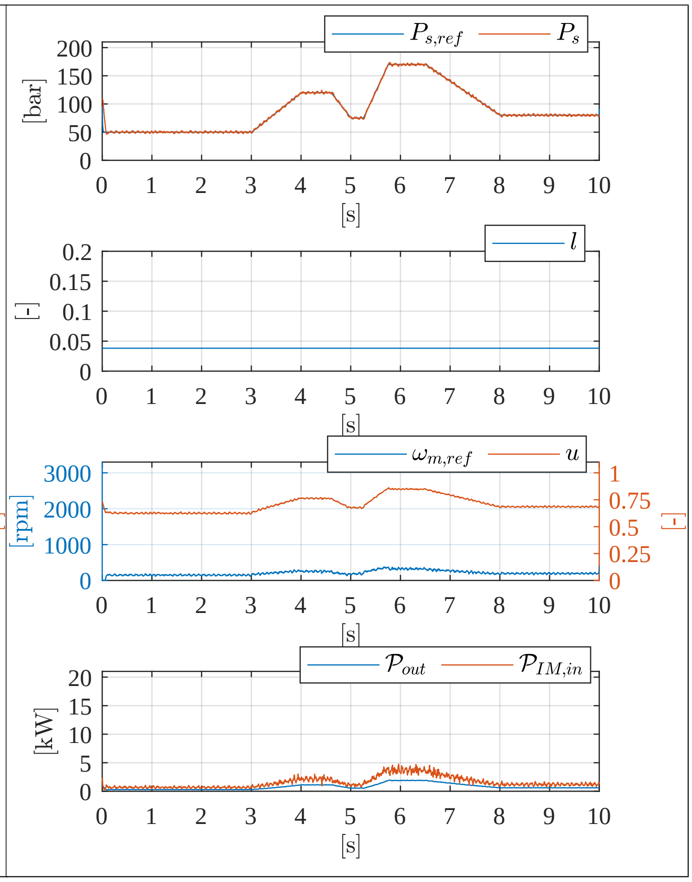

(d) LL0, LSL3.

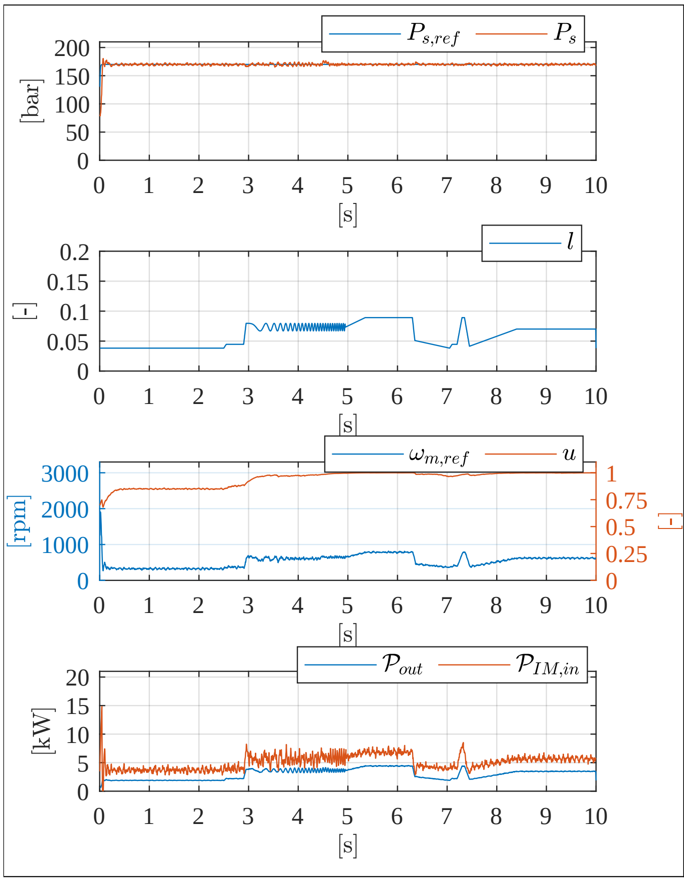

(a) LL1, LSL0.

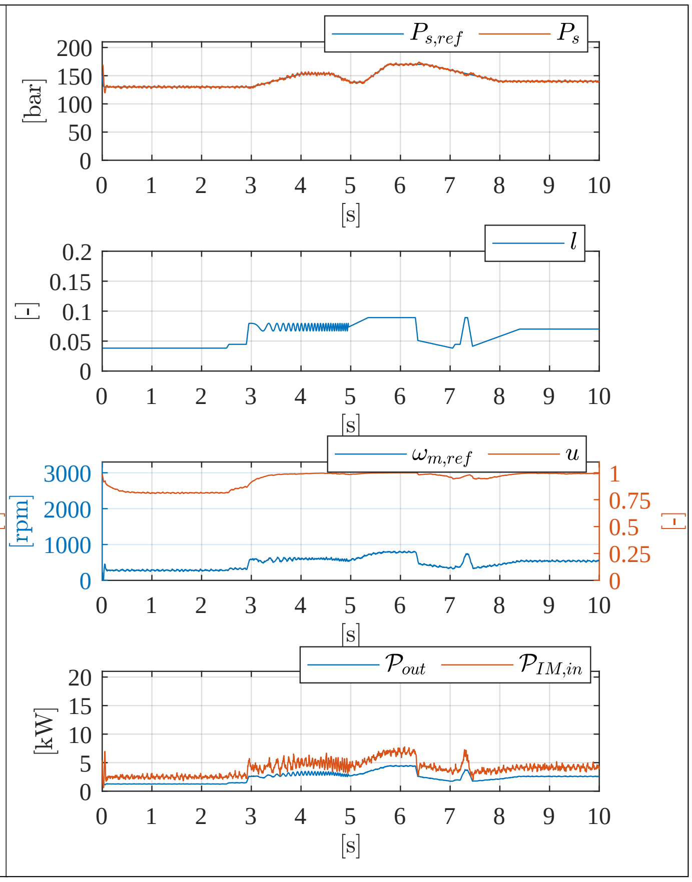

(b) LL1, LSL1.

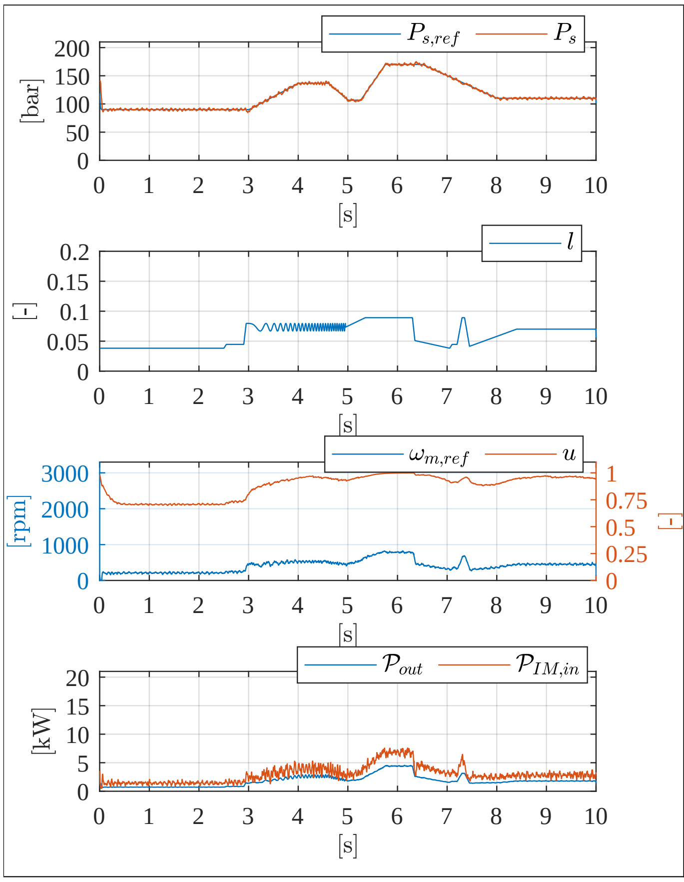

(c) LL1, LSL2.

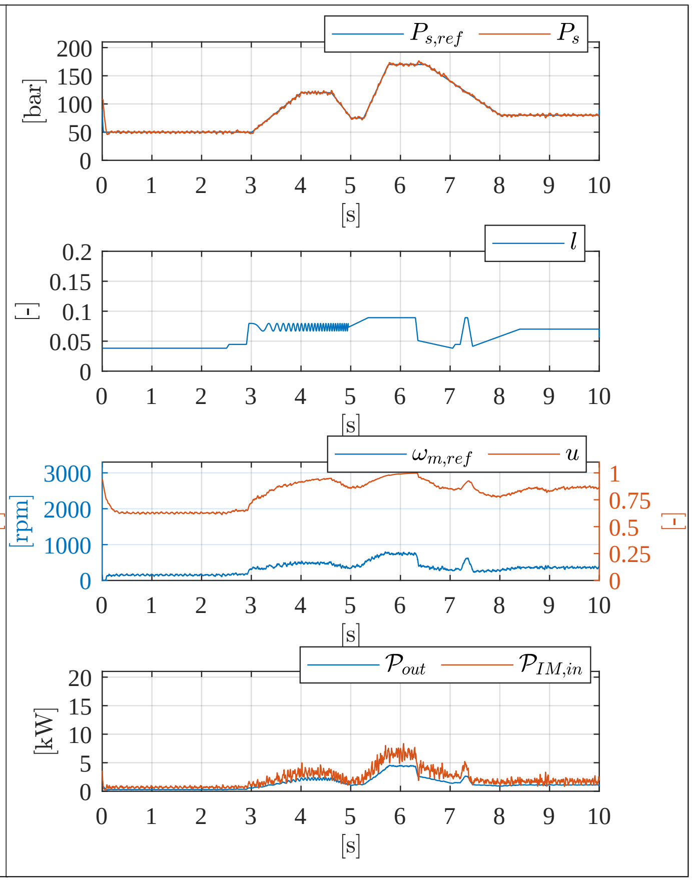

(d) LL1, LSL3.

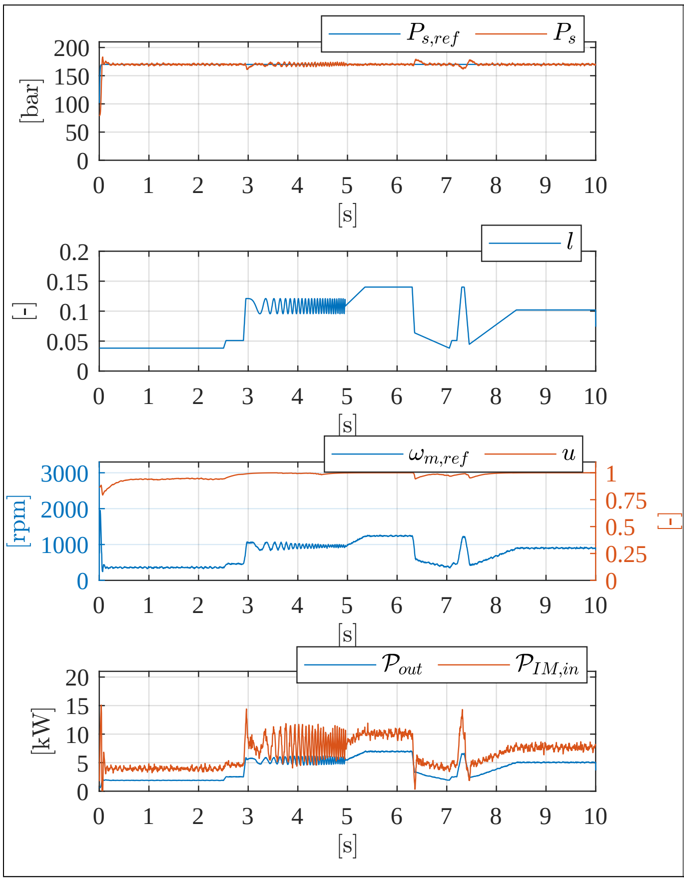

(a) LL2, LSL0.

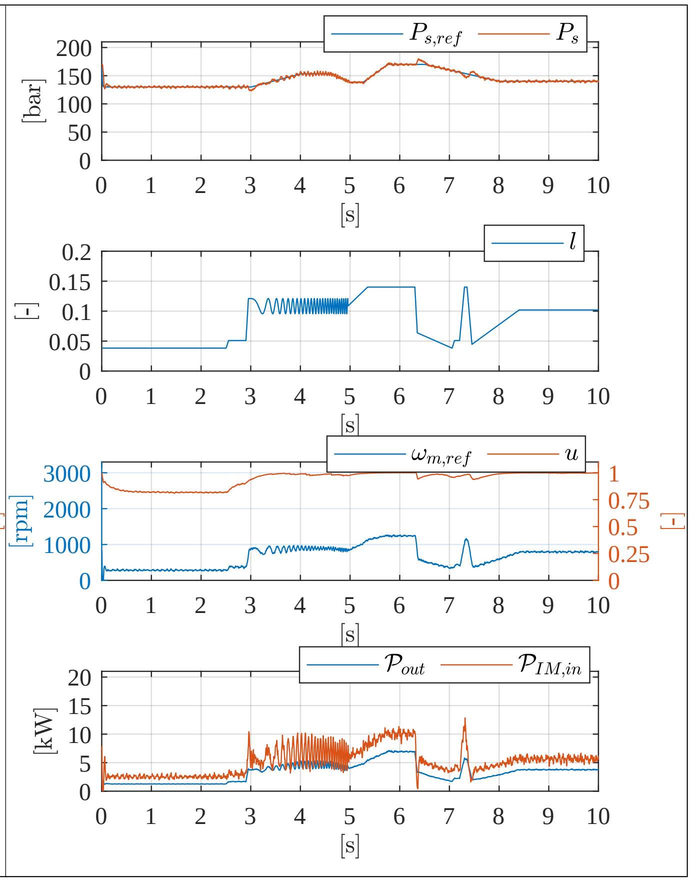

(b) LL2, LSL1.

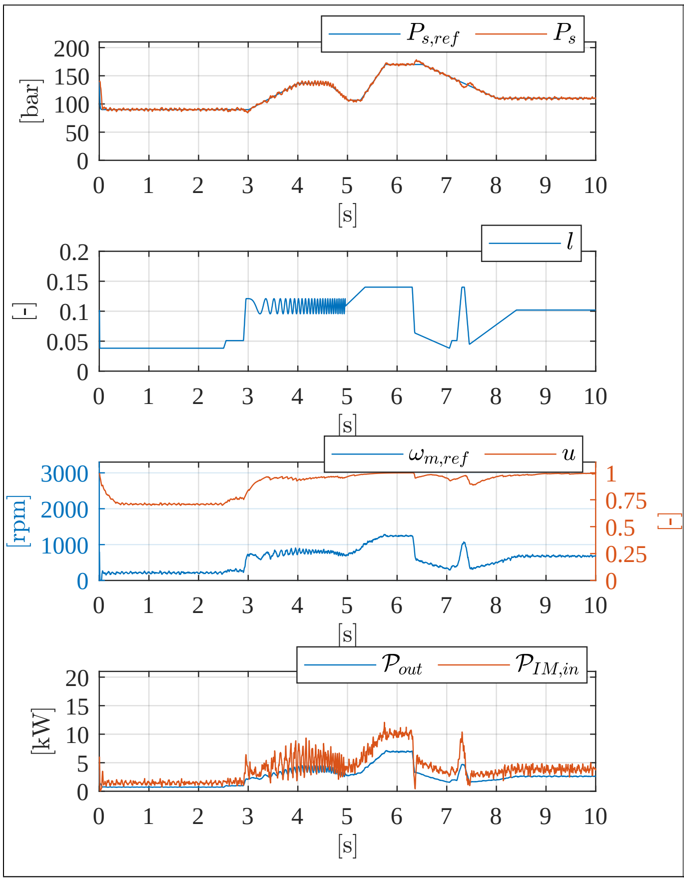

(c) LL2, LSL2.

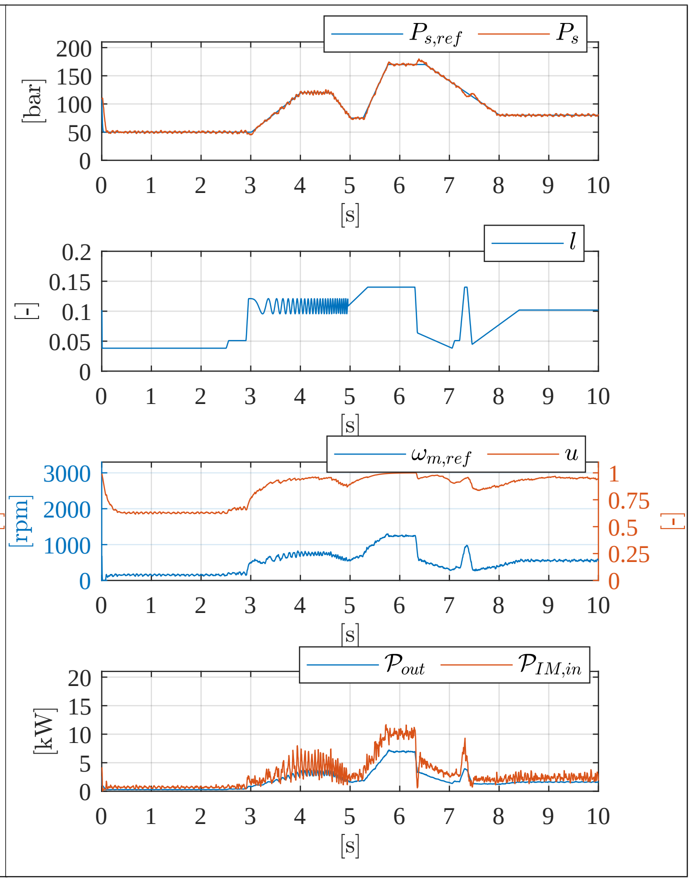

(d) LL2, LSL3.

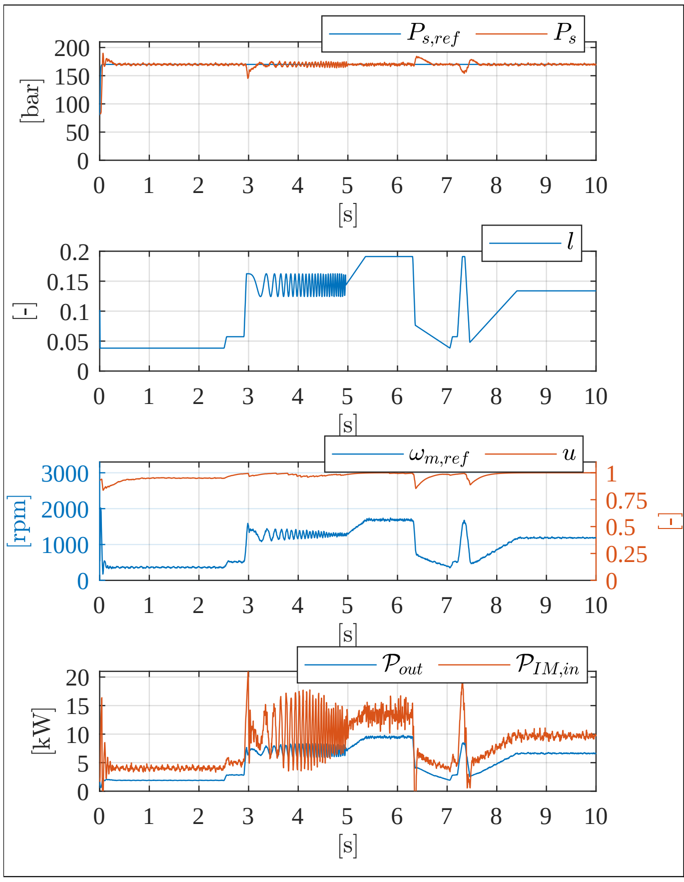

(a) LL3, LSL0.

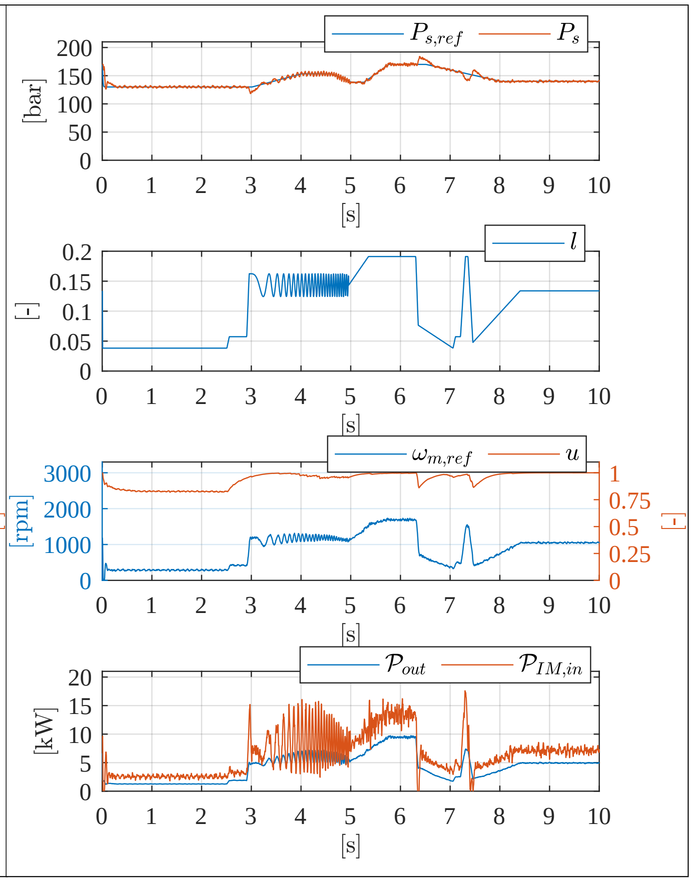

(b) LL3, LSL1.

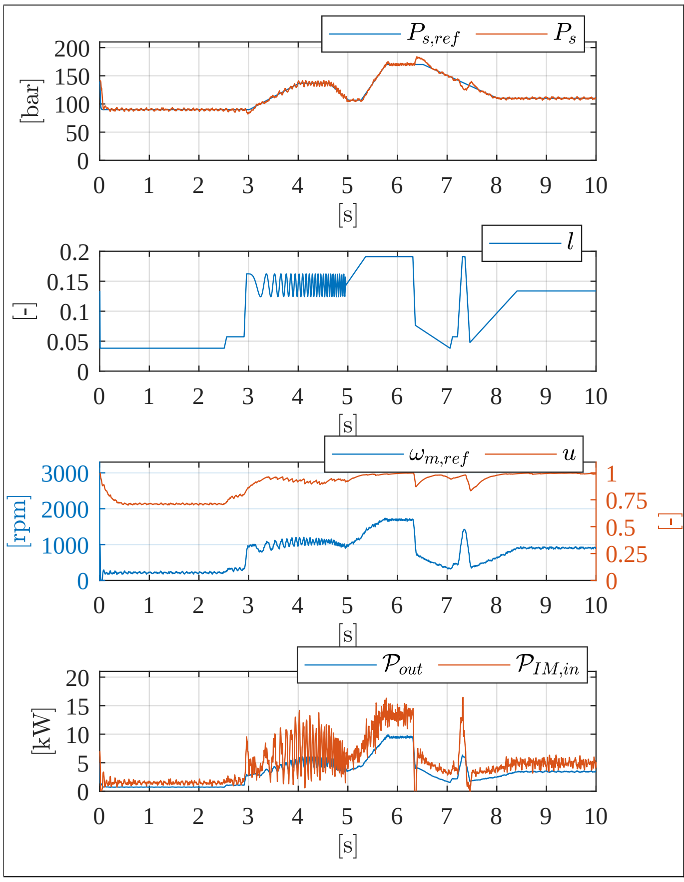

(c) LL3, LSL2.

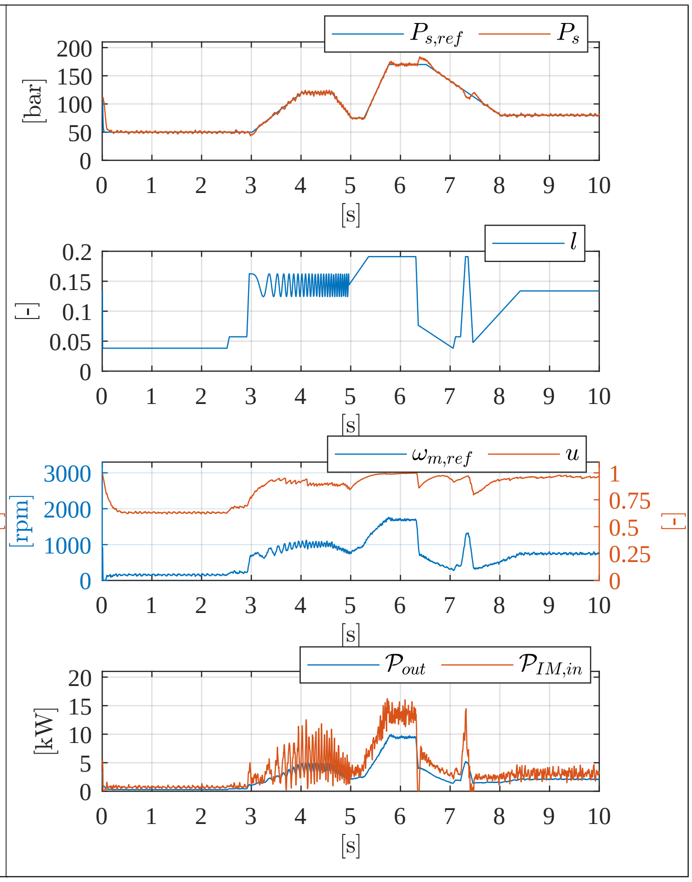

(d) LL3, LSL3.

Experimental data for 2SMDO + boundary layer and 1SMDO + boundary layer G

In this appendix, the experimental data for the developed MIMO control of the hydro gear is stated. In this version a boundary layer is added to the 2SMDO according to equation G.1, as a measure to reduce the experienced control oscillations during constant reference input.

$$v_s = k_1\sqrt{|\sigma_s|}\text{sgn}(\sigma_s) + w \quad , \qquad \dot{w} = k_2\frac{\sigma_s}{|\sigma_s| + \epsilon} \tag{G.1}$$

The measured performance figures are stated in table G.1.

Table G.1

Load Level (LL) \ Load Sense Level (LSL) — $RMSe$ [dbar] / $Eff.$ [%]	0	1	2	3
0	9.7/47.9	12.3/49.1	11.9/48.8	11.6/47.6
1	13.2/59.1	12.6/59.4	15.1/61.1	14.7/60.3
2	19.9/63.5	17.1/63.8	18.6/64.5	18.7/63.9
3	31.9/65.2	24.8/65.7	24.4/66.6	23/65.9

Based on this, the average performance figures are the following:

$$\overline{RMSe} = 17.46[\text{dbar}] \qquad \downarrow 35.12[\text{dbar}] \tag{G.2}$$

$$\overline{Eff.} = 59.53[\%] \qquad \uparrow 9.99[p.p.] \tag{G.3}$$

The corresponding plots of the pressure tracking, the load, the control inputs and measured powers are depicted in the following:

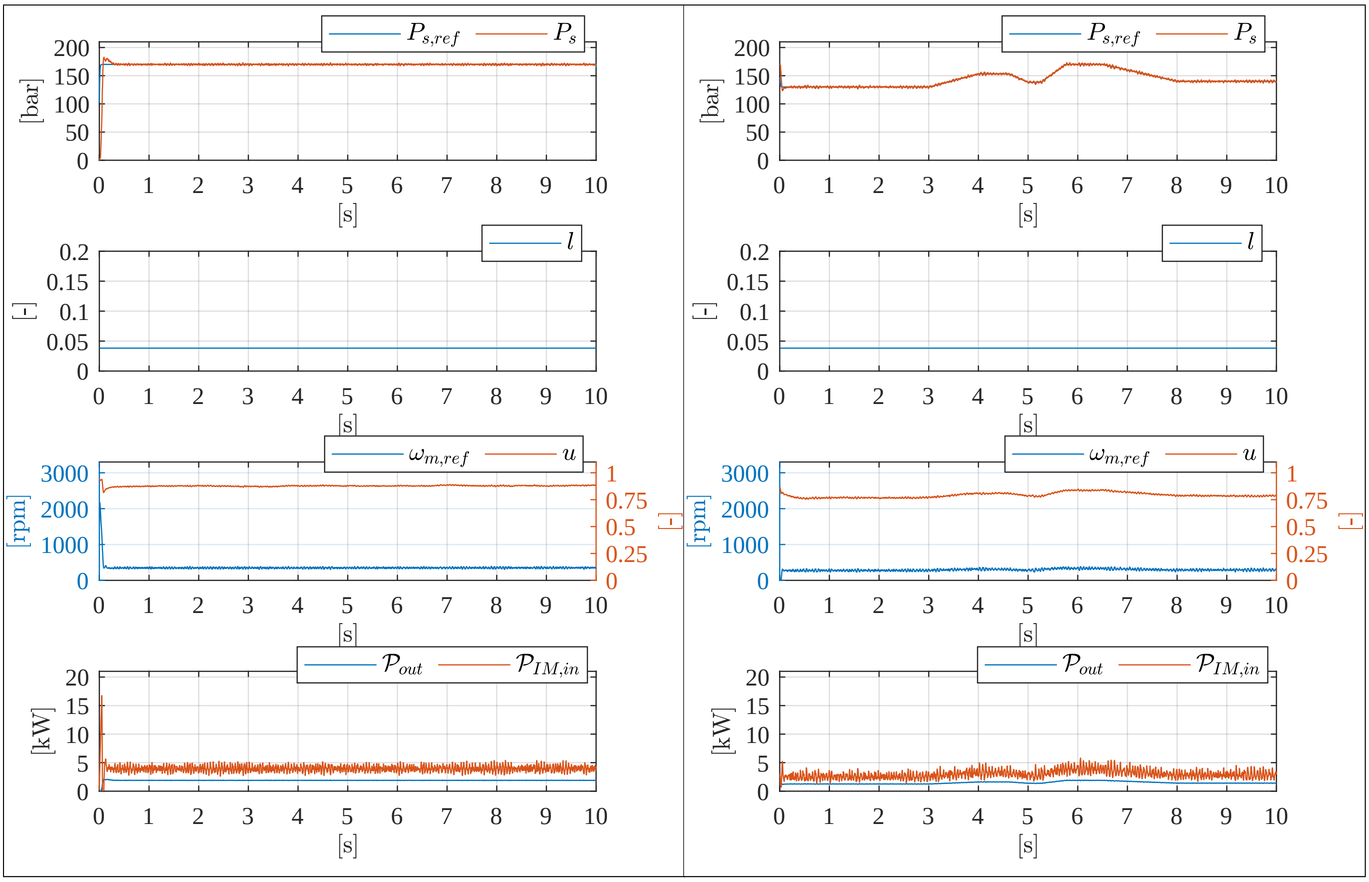

(a) LL0, LSL0.

(b) LL0, LSL1.

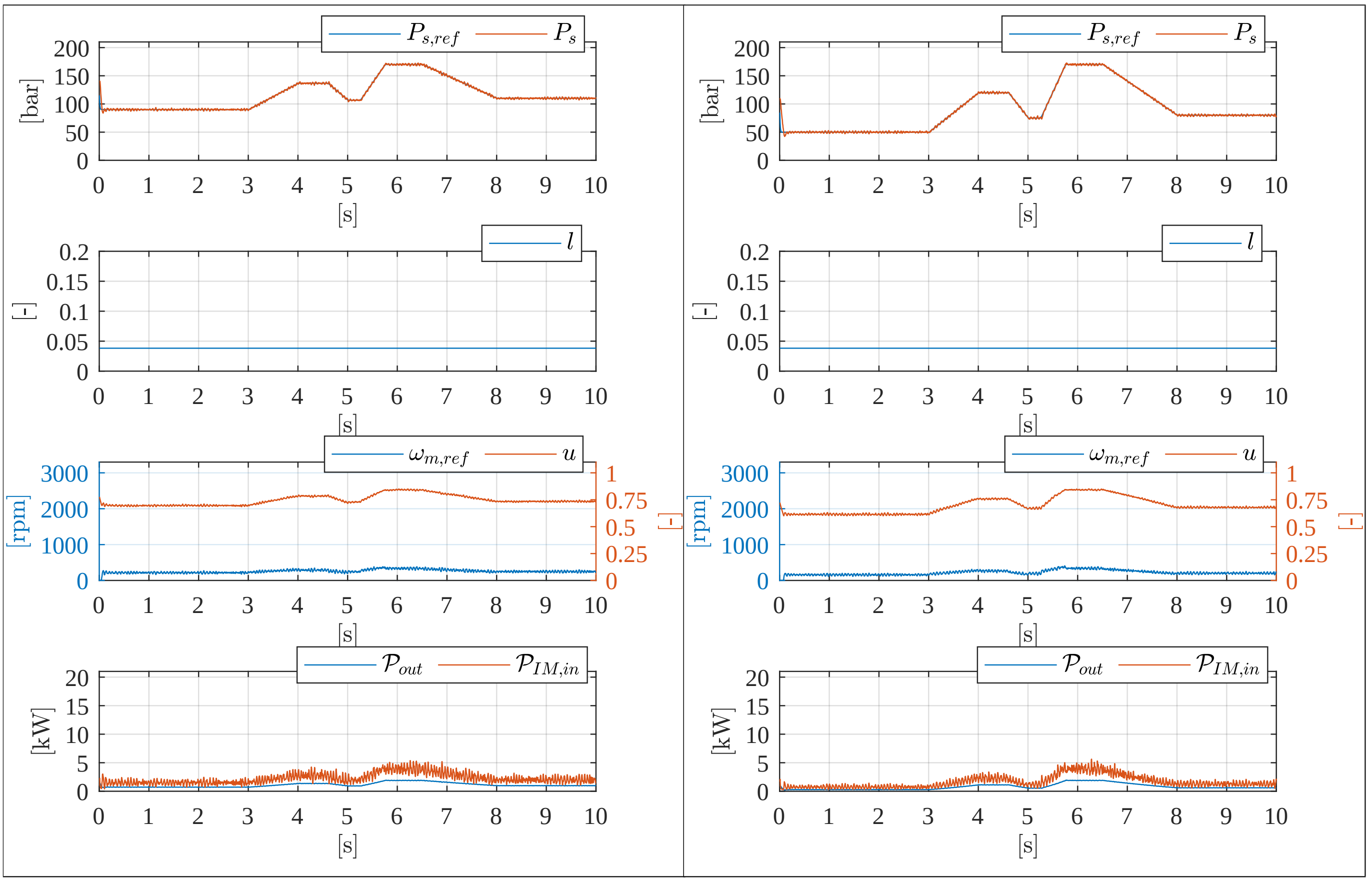

(c) LL0, LSL2.

(d) LL0, LSL3.

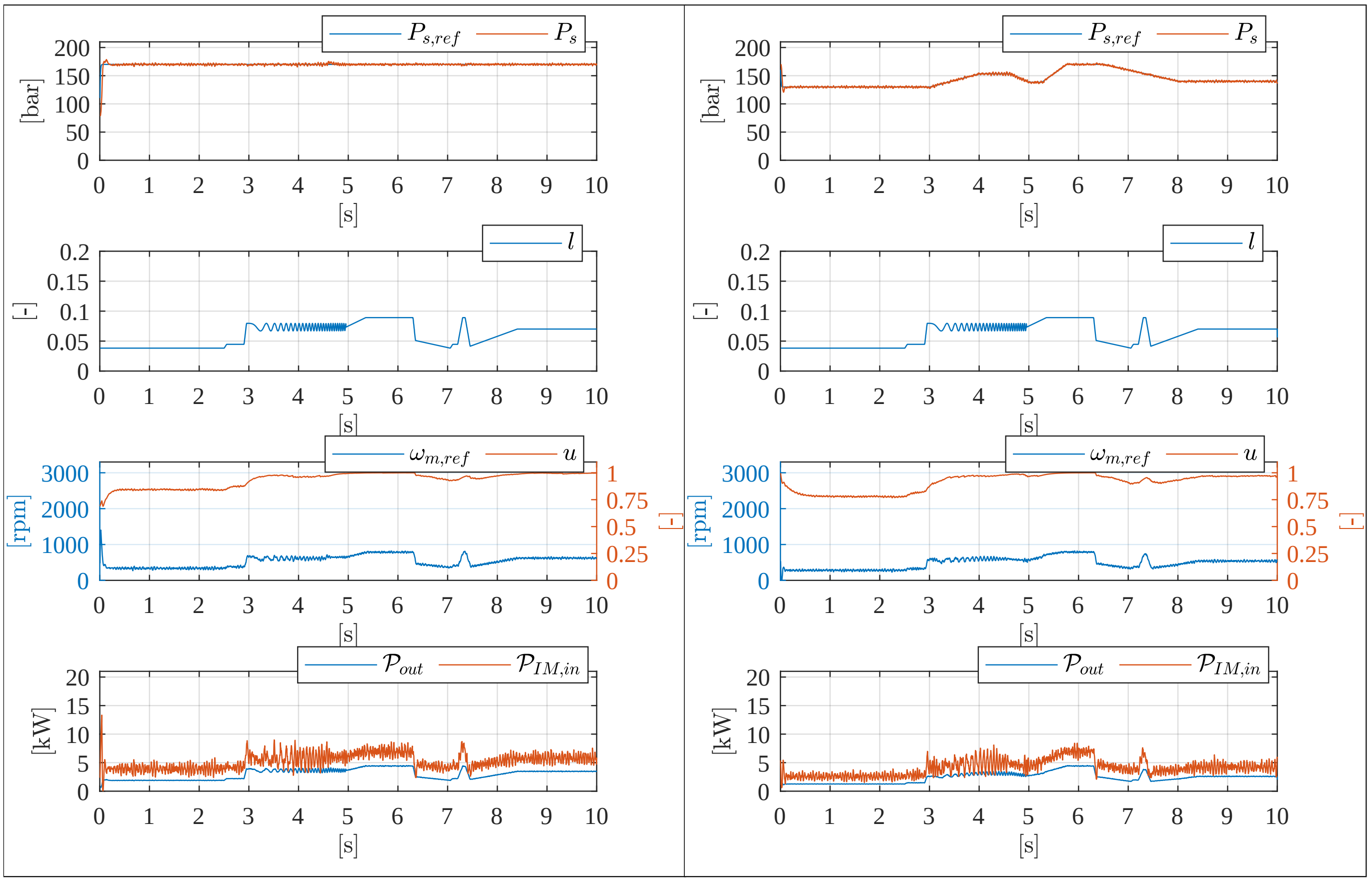

(a) LL1, LSL0.

(b) LL1, LSL1.

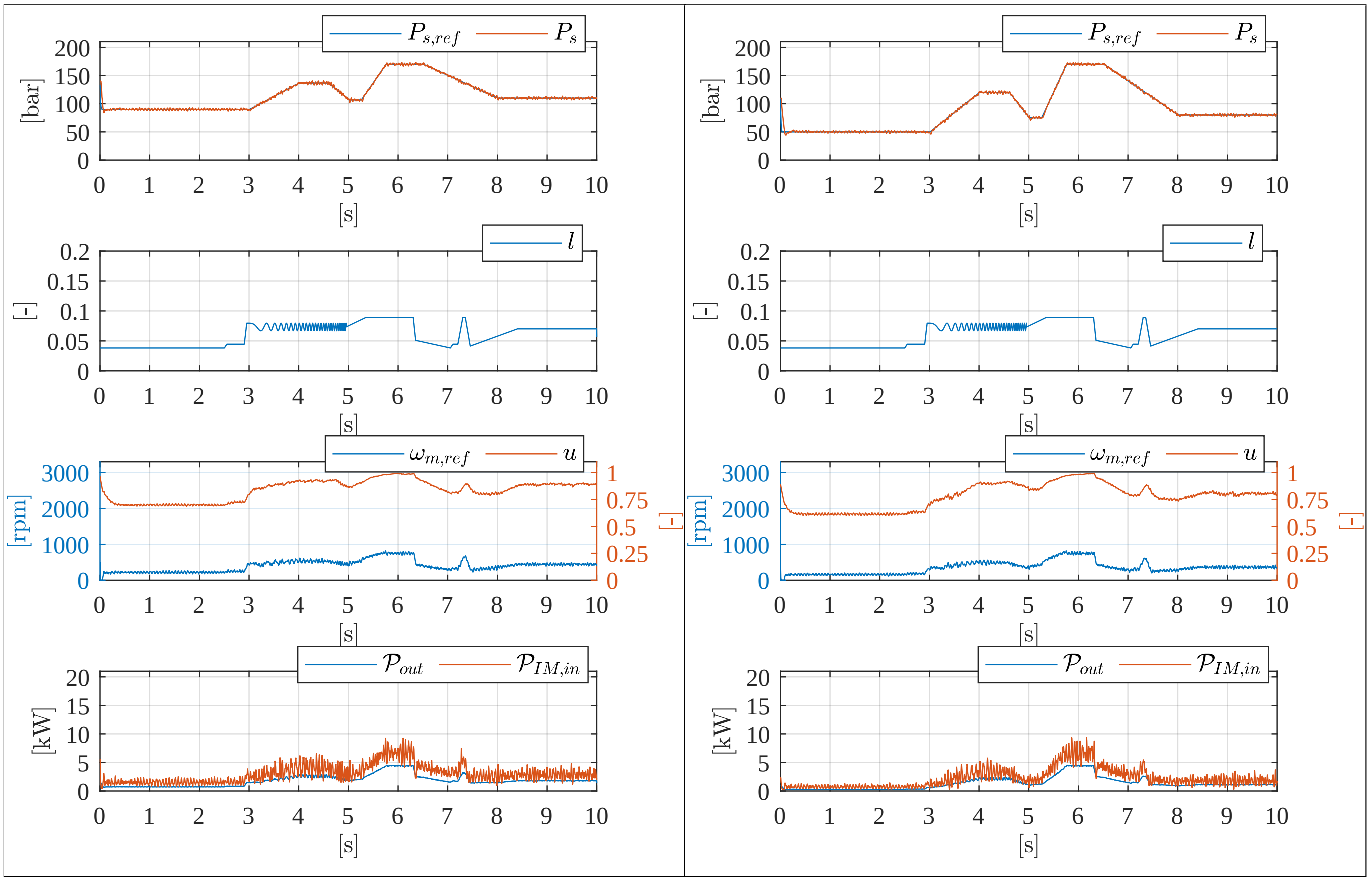

(c) LL1, LSL2.

(d) LL1, LSL3.

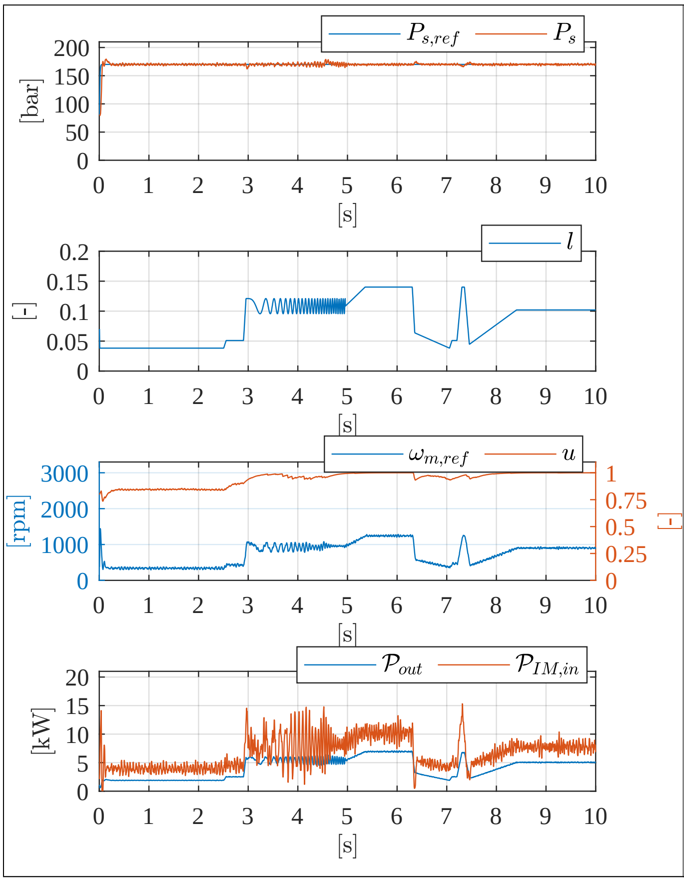

(a) LL2, LSL0.

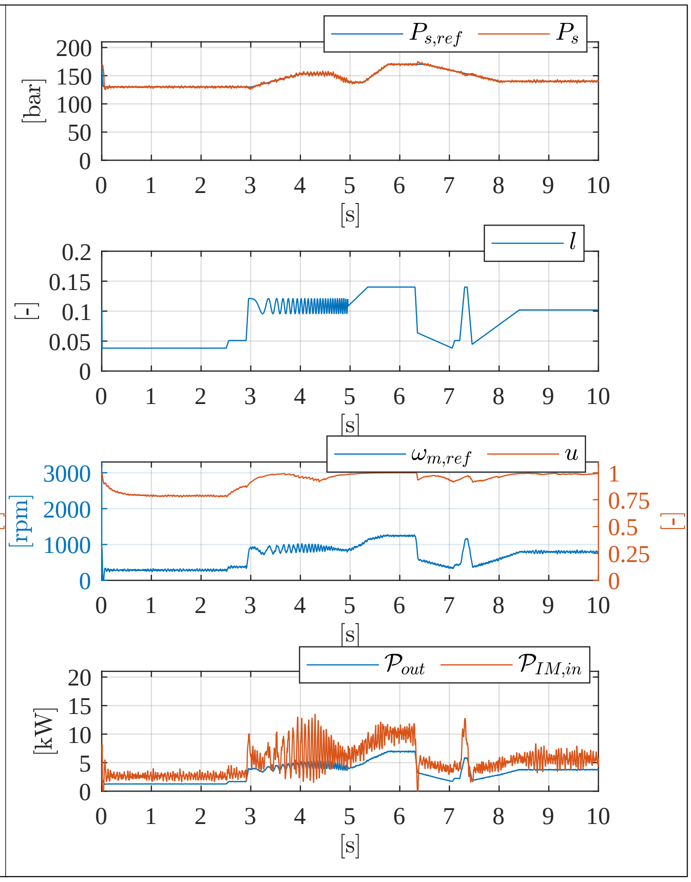

(b) LL2, LSL1.

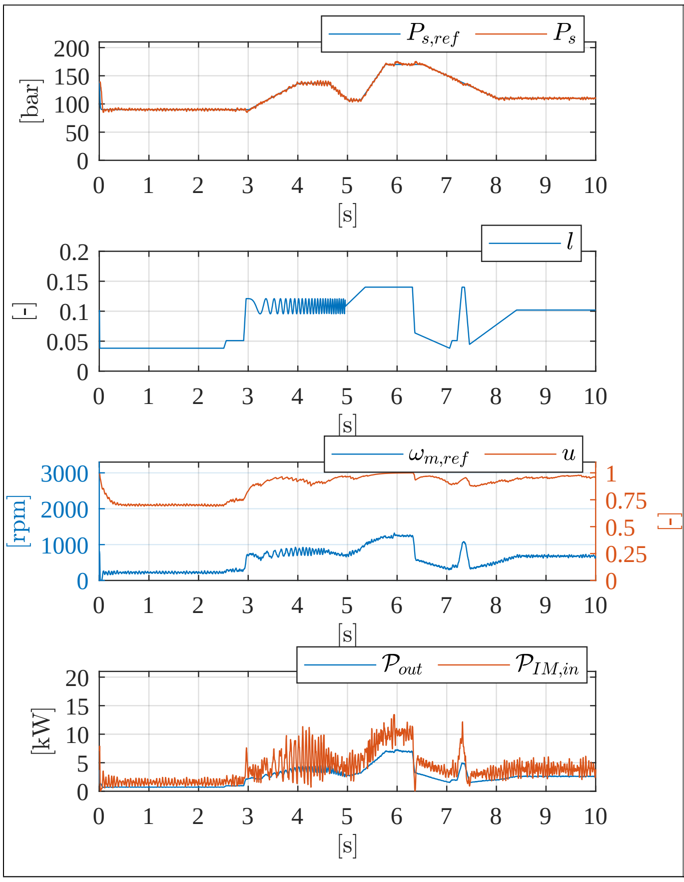

(c) LL2, LSL2.

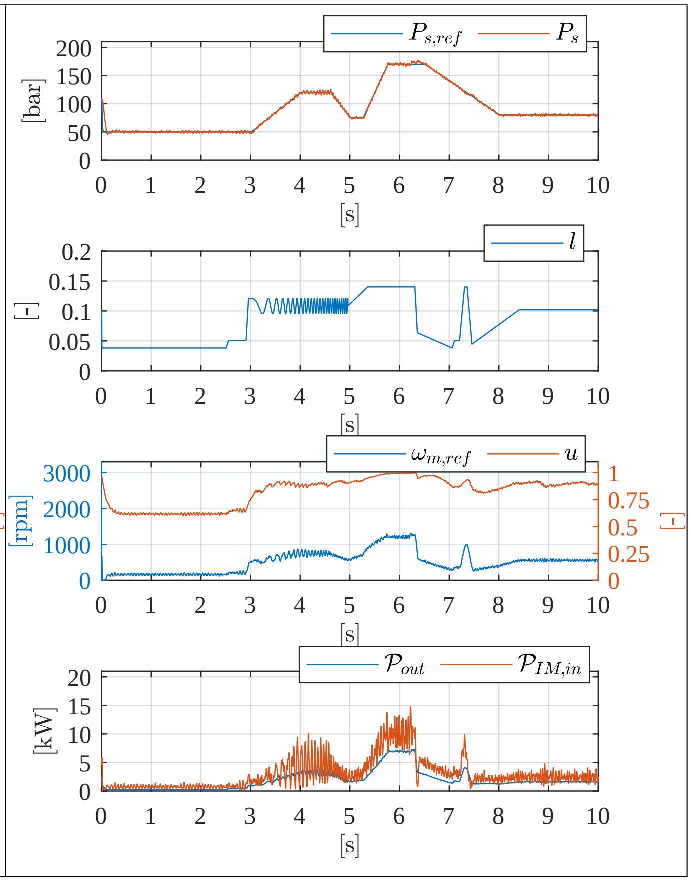

(d) LL2, LSL3.

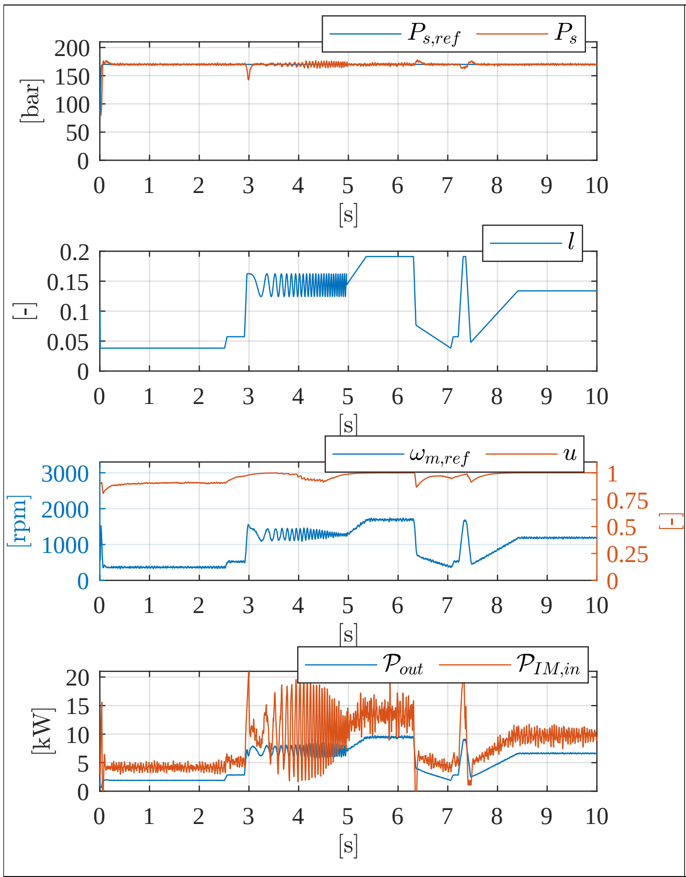

(a) LL3, LSL0.

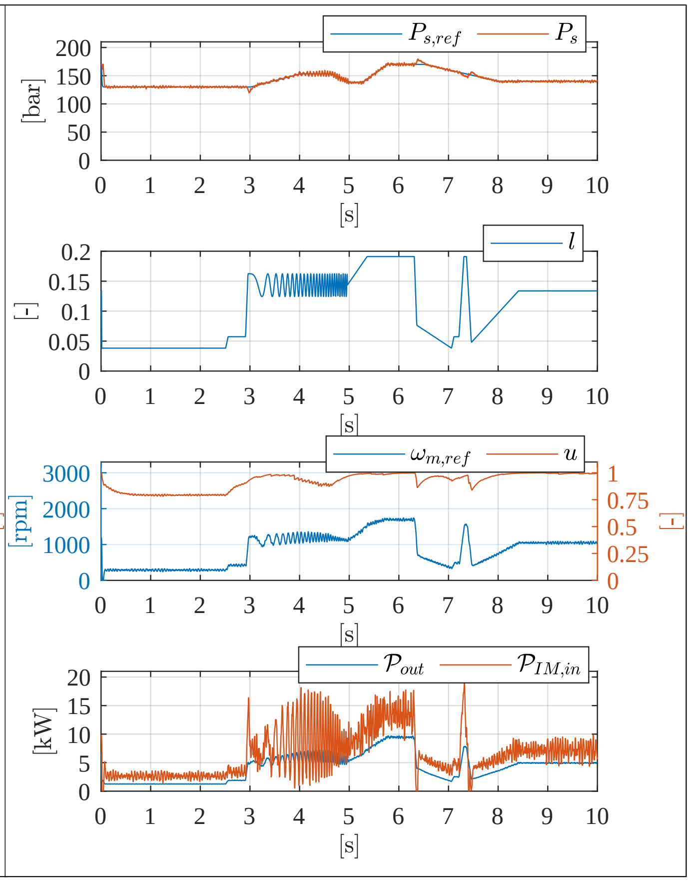

(b) LL3, LSL1.

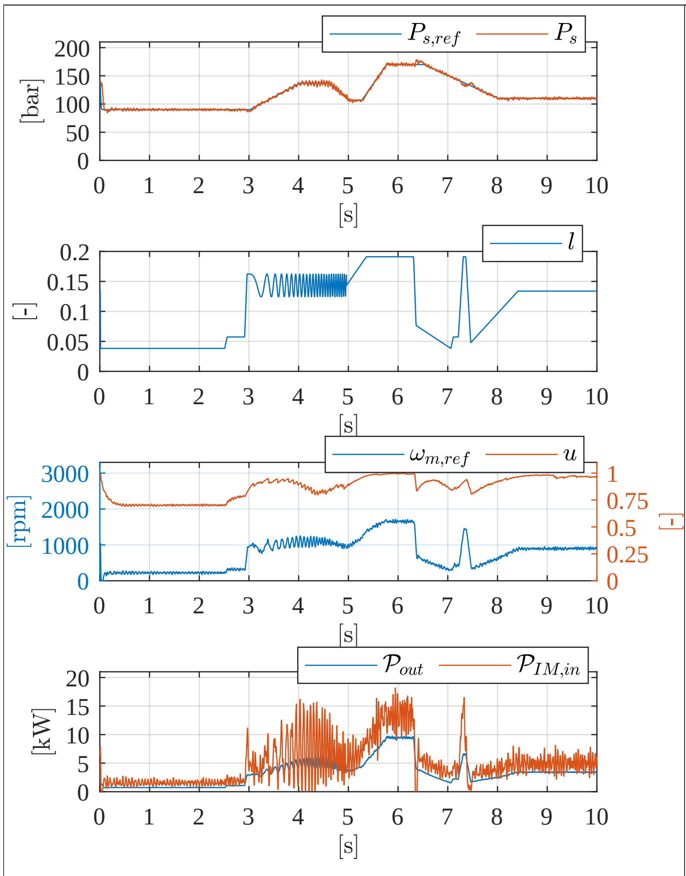

(c) LL3, LSL2.

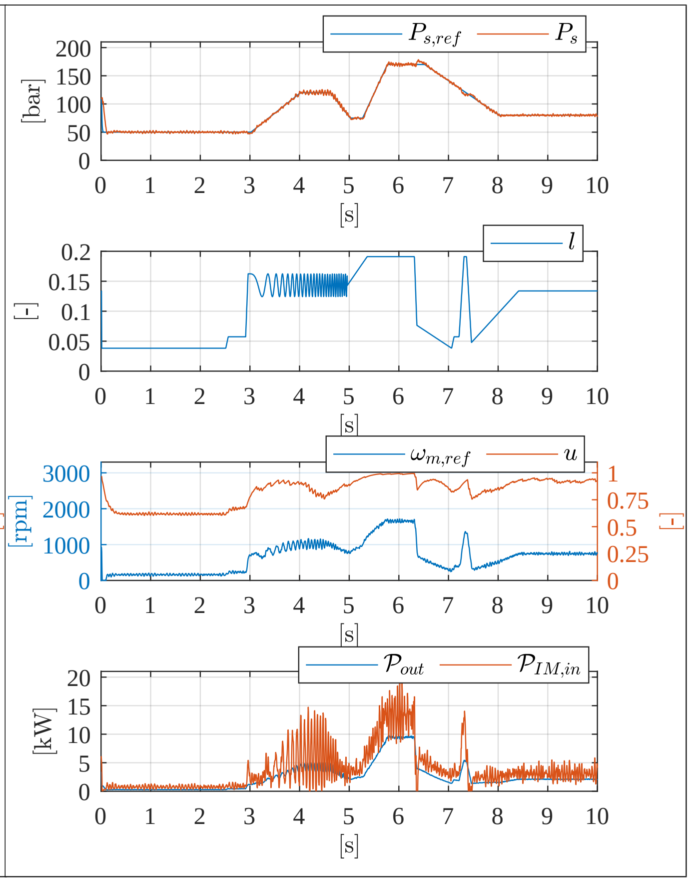

(d) LL3, LSL3.